Title	Theoretical Studies on the Electronic Structures of d-π Conjugated Systems : Molecule-based Magnets and Non-heme Oxygen Transport Proteins
Author(s)	鷹野, 優
Citation	大阪大学, 2002, 博士論文
Version Type	VoR
URL	https://hdl.handle.net/11094/1084
rights	
Note	

Theoretical Studies on the Electronic Structures of d-π Conjugated Systems: Molecule-based Magnets and Non-heme Oxygen Transport Proteins

Yu Takano

Department of Chemistry,
Graduate School of Science,
Osaka University

2002

Theoretical Studies on the Electronic Structures of d-π Conjugated Systems: Molecule-based Magnets and Non-heme Oxygen Transport Proteins

Yu Takano

Department of Chemistry,
Graduate School of Science,
Osaka University

2002

Acknowledgement

Contents

i

Part III

Chemical Bonding Character, Magnetic Coupling and Dioxygen Binding Process of Non-Heme Oxygen Transport Protein

Part IV

General Conclusion

Part I

General Introduction

Part I

Chapter 1

Introduction of This Thesis

Transition metal compounds ligated some molecules or atoms called coordination ligands, namely complexes, have been attracted continuous interests of many scientists because the complexes play key role in a lot of field such as material science, chemistry and biology. Especially, d-p conjugated complexes, which utilize organic compounds as ligands, are expected as the interesting multifunctional substances with the characteristics of both inorganic and organic materials due to various interaction between d electrons of transition metal ions and p ones of organic ligands.

In material science, the conjugated systems provide the possibilities of novel materials such as photo-induced magnets. Since the electronic structure of transition metal complexes greatly depends on coordination ligands, the appropriate choice of ligands enables us to obtain novel and useful materials. Theoretical approaches can provide a lot of insights into such molecular design. However, theoretical strategy for the design of new materials has still been limited yet.

In biology, many metalloproteins, for example, photosystem II of photosynthetic organisms, the terminal respiratory enzyme cytochrome oxidase, the nitrogen activating enzyme nitrogenase, the methane activating enzyme methane monooxygenase, and ribonucleotide reductase which converts ribonucleotides into deoxynucleotides, are fundamentally important for life processes. Despite their obvious importance and the intense experimental interest, until a few years ago, there were only few studies of these systems using accurate quantum chemical methods.

Calculations using high-accuracy methods on such transition-metal containing systems are relative new. In the initial period, at the end of the 1980's, these calculations were restricted to very small systems containing less than 10 atoms. It turned out early that it was very difficult to obtain qualitative agreement with experiments even for atoms unless very sophisticated methods and huge basis sets were used [1]. The reason was that both nondynamical and dynamical correlation effects are unusually large, and these effects are also strongly coupled. Still, after a few years of development, results could be obtained using a small degree of semiempirical parameterization [2], which were in quite good agreement with experiments for small, mainly cationic, systems, for which accurate ion beam experiments were available [3]. A rather surprising experience from this period with model calculations on small systems, worth mentioning here since it was very important for the development of the present day models, was that even these small

systems could provide insights which turned out to be generally relevant also for larger realistic systems. The relative insensitivity of some of the most important results to the choice of model, for example, concerning the choice of ligands, was promising for future modeling of complex systems.

A breakthrough for the treatment of larger systems came with the development of highly accurate density functional (DFT) methods about a decade ago [4, 5]. The key to the increased accuracy of these methods was the incorporation of terms in the functionals that depend on the gradient of the density. This was primarily important for the description of the exchange energy, much less so for the correlation energy. Incorporation of exact exchange and a few semiempirical parameters were also significant in this context. Benchmark calculations showed that using these so-called hybrid functionals, results almost as accurate as those obtained from the most accurate ab initio methods could be obtained at a fraction of the cost. For benchmark tests, which have gradually included more and more systems, the hybrid DFT methods have been shown to give energies normally within a few kilocalories per mole of essentially exact experiments.

The aim of the doctorate thesis is the elucidation of the magnetic and electronic structure for d-p conjugated system, especially d-π-p and d-π-d conjugated magnetic systems and the active site of non-heme oxygen transport protein. The author has investigated the spin alignment mechanism of d-π-p and d-π-d conjugated magnetic system (Part II) and the dioxygen binding process in non-heme oxygen transport protein (Part III) with quantum chemical approaches such as hybrid DFT methods.

In the following, the author briefly describe some of the highlights of the three parts. Part I describes the aim of this doctorate thesis and provides the theoretical backgrounds of computational methods, calculation of magnetic interactions and orbital analyses, which have been employed through this thesis.

Part II contains a through discussion of the magnetic couplings and coordination ligand effects of d-π-p and d-π-d conjugated magnetic systems. Several quantum chemical calculations have been performed to understand the magnetic interaction. Calculated results have been discussed from the viewpoint of the effective exchange integrals, charge and spin density distributions and the shape and symmetry of natural orbitals. The author have made it clear that coordination ligands regulate the charge transfer from π conjugate bridge to the transition metal ion,

4

resulting in the appropriate estimate of the magnetic interaction.   Finally, spin alignment rules for d-π-p and d-π-d conjugated system have been proposed on the basis of the calculated results and experimental ones.

Part III consists of theoretical explanation of the magnetic interaction and dioxygen binding process in hemocyanin and hemerythrin.   The author have elucidated that ligand coordination effects control the electron transfer in the active sites, providing the sufficient effects to the magnetic interaction and the dioxygen binding process in both hemocyanin and hemerythrin.

Part I

Chapter 2

Theoretical Background

2.1 Computational Methods: HF, post-HF and DFT

2.1.1. Hartree–Fock approximation

Hartree–Fock (HF) approach [6], which is to optimize the molecular orbitals (MOs) in order to obtain a "best" many-electron function of single determinant, has been employed for a lot of theoretical calculations. In HF theory, according to the variational principle, the "best" orbitals are those which minimize the total electronic energy;

$$E_0 = \langle \Psi_0 | H | \Psi_0 \rangle = \sum_a \langle a|h|a \rangle + \frac{1}{2} \sum_{ab} \langle ab \| ab \rangle. \tag{1}$$

The equation for the "best" spin orbitals is the Hartree–Fock integro-differential equation;

$$h(1)\chi_a(1) + \sum_{b \neq a} \left[\int d\mathbf{x}_2 |\chi_b(2)| r_{12}^{-1} \right] \chi_a(1) - \sum_{b \neq a} \left[\int d\mathbf{x}_2 \chi_b^*(2) \chi_a(2) r_{12}^{-1} \right] \chi_b(1) = \varepsilon_a \chi_a(1), \tag{2}$$

where

$$h(1) = -\frac{1}{2}\nabla_1^2 - \sum_A \frac{Z_A}{r_{1A}}, \tag{3}$$

is the kinetic energy and potential energy for attraction to the nuclei, of a single electron chosen to be electron-one. The orbital energy of the spin orbital χ_a is ε_a.

2.1.2. Møller–Plesset perturbation theory

The Hartree–Fock approximation, while it is remarkably successful in many cases, has its limitations. The HF method fails to apply for the strong electron correlated systems including the transition metal ions. Hence, improvement upon the HF approximation, post-HF approximation, is necessary in order to investigate the electronic structure of the strong electron correlated systems such as the d-p conjugated systems and the active site of non-heme oxygen transport protein. One of the post-HF procedure is Møller–Plesset (MP) perturbation theory [6–9]. In MP perturbation

7

theory, the Hamiltonian is partitioned as

$$H = H_0 + V,$$
(4)

where H_0 is the HF Hamiltonian, and V is the perturbation term.   The result for the second-order (MP2) energy can express as follow;

$$E_0^{(2)} = \frac{1}{4} \sum_{abrs} \frac{|\langle ab \| rs \rangle|^2}{\varepsilon_a + \varepsilon_b - \varepsilon_r - \varepsilon_s}.$$
(5)

2.1.3. Configuration Interaction

A different procedure beyond HF is the method of configuration interaction (CI) [10].   CI is conceptually the simplest.   The basic idea is to represent the exact wave function as a linear combination of N-electron trial functions

$$|\Phi_0\rangle = c_0 |\Psi_0\rangle + \left(\frac{1}{1!}\right)^2 \sum_{ar} c_a^r |\Psi_a^r\rangle + \left(\frac{1}{2!}\right)^2 \sum_{abrs} c_{ab}^{rs} |\Psi_{ab}^{rs}\rangle + \left(\frac{1}{3!}\right)^2 \sum_{abcrst} c_{abc}^{rst} |\Psi_{abc}^{rst}\rangle + \cdots,$$
(6)

where $|\Psi_0\rangle$ is HF wavefunction, $|\Psi_a^r\rangle$ is a singly excited one, and $|\Psi_{ab}^{rs}\rangle$ is a double excited one, etc.   Coefficients c are determined by a linear variational method.   In principle, CI including all excited trial functions (full CI) provides an exact solution of the many-electron problem.   In practice, however, full CI calculations within all MO space are usually out of the question because of enormous trial functions.   Hence, we perform full CI calculation within only sufficient MO space known as active space, which is called CASCI calculation [11].   Here, CASCI$\{m, n\}$ denotes calculation with m electrons and n orbitals.

2.1.4. Coupled Cluster approximation

The CASCI method includes only nondynamical correlation arising from orbital degeneracy.   In order to investigate the electronic structure of the strong electron correlated systems, we need to perform the high accuracy calculation involving not only nondynamical

correlation but also dynamical one resulting from electron-electron repulsion. Perturbation theory methods sometimes provide some relief because the wavefunction usually contains the dynamical correlation to some degree. However, the inclusion of the correlations often fails. The coupled cluster (CC) [12, 13] approach is a method to introduce interactions among electrons within clusters as well as coupling among these clusters of electrons. The CC wavefunction $|\Psi_{CC}\rangle$ can be expressed with the HF wavefunction $|\Psi_0\rangle$ and the excitation operator T as

$$|\Psi_{CC}\rangle = \exp(T)|\Psi_0\rangle, \tag{7}$$

2.1.5. Density Functional Theory

Density Functional Theory (DFT) [4, 5] provides a convenient approach for investigating electronic structures of atoms, molecules, and solids. It is theoretically simple, conceptually meaningful, and computationally effective. Much effort has been devoted to its development in recent decades. According to the Hohenberg–Kohn theorems, every atomic or molecular ground-state property is a functional of the electron density. In the Kohn–Sham DFT scheme, in which the concept of orbital is still retained, the exact exchange (HF) for a single determinant is replaced by a more general expression, the exchange-correlation functional, which can include terms accounting for both exchange energy and the electron correlation which is omitted from Hartree–Fock theory:

$$E_{KS} = -\frac{1}{2}\sum_i \int \phi_i(r_1)^* \nabla^2 \phi_i(r_1) dr_1 + \sum_A \int \frac{Z_A}{|R_A - r_1|}\rho(r_1)dr_1 + \frac{1}{2}\sum_i \frac{\rho(r_1)\rho(r_2)}{|r_1 - r_2|}dr_1 dr_2 + E_{XC}, \tag{8}$$

$$\rho(r_1) = \sum_i \phi_i(r_1)^* \phi_i(r_1). \tag{9}$$

The first term is the electronic kinetic energy, the second term shows the electron–nuclei attraction energy, the third term expresses the electron–electron repulsion energy and the last term is the exchange–correlation energy. In the Kohn–Sham DFT scheme, only E_{XC} is unknown. Recently, a lot of exchange and correlation functionals are developed. In this study, BLYP exchange–correlation functional has been employed, which consists of Slater exchange functional,

Becke's exchange correction [14], Vosko, Wilk, and Nusair (VWN) correlation functional [15] and the correlation correction of Lee, Yang, and Parr (LYP) [16].

2.1.6. Hybrid DFT approach

In addition to pure DFT methods, hybrid DFT calculation, in which the exchange functional is a linear combination of the Hartree–Fock exchange and a functional integral of the above form, is useful for the elucidation of the magnetic and electronic structure of the strong correlated systems.   In the hybrid DFT calculations, exchange-correlation potentials are generally defined by

$$E_{XC} = C_1 E_X^{HF} + C_2 E_X^{Slater} + C_3 \Delta E_X^{Becke88} + C_4 E_C^{VWN} + C_5 \Delta E_C^{LYP}, \tag{10}$$

where the first, second and third terms in the right hand of eq. (10) indicate HF and Slater exchange functionals and Becke's exchange correction involving the gradient of the density, respectively. The fourth and fifth terms mean VWN correlation functional and the correlation correction of LYP which includes the gradient of the density, respectively. C_i (i = 1–5) are the mixing coefficients. For example, the parameter sets (C_1, C_2, C_3, C_4 and C_5) are taken as (0.2, 0.8, 0.72, 1.00 and 0.81) for B3LYP [17] and (0.5, 0.5, 0.5, 1.0 and 1.0) for B2LYP [18], respectively.

2.2 Computation of effective exchange integrals

The effective exchange interactions (J_{ab}) between magnetic sites in the highest- (HS) or the lowest- (LS) spin complexes have been described by the Heisenberg (HB) model, from the experimental grounds [19]

$$H(HB) = -2\sum J_{ab} S_a \bullet S_b, \tag{11}$$

where S_a and S_b represent the spins at sites a and b, respectively. J_{ab} can be experimentally determined by the measurement of magnetic susceptibility.   Recent developments of the ab initio computational techniques such as UHF and UCCSD(T), together with the spin polarized DFT (UDFT) methods, have enabled us to calculate J_{ab} values.   In fact, the UHF and UDFT solutions

for the LS states of magnetic transition metal complexes usually exhibit broken-symmetry (BS) problem [19–25]. Therefore, spin projection of the BS solutions should be carried out to eliminate spin contaminations in spin-polarized DFT and UHF methods. A useful scheme for spin projection has been developed on the basis of the isotropic HB Hamiltonian combined with UHF and UDFT calculations. The spin projections of these solutions are performed assuming energy splitting of the HB model, providing a practical computational scheme for J_{ab} values for linear uniform chains with N-spin sites [26, 27]. Our spin projection scheme has been applied to triplet methylene clusters $(CH_2)_N$ (N = 2–11) [26] and polycarbenes with m-phenylene bridge (N = 2–10) [27], providing reasonable J_{ab} values as compared to the experiments. In this thesis, since these models can be regarded as two ore three spin site systems, the J_{ab} values were calculated using different computational schemes, eqs. (12a)–(12c), by combination of UDFT with the Heisenberg model [19–25, 28–32] as

$$J_{ab}^{(1)} = \frac{^{LS}E_X - {}^{HS}E_X}{S_{max}^2},$$

(12a)

$$J_{ab}^{(2)} = \frac{^{LS}E_X - {}^{HS}E_X}{S_{max}(S_{max}+1)},$$

(12b)

$$J_{ab}^{(3)} = \frac{^{LS}E_X - {}^{HS}E_X}{^{HS}\langle S^2 \rangle_X - {}^{LS}\langle S^2 \rangle_X},$$

(12c)

where $^{Y}E_X$ and $^{Y}\langle S^2 \rangle_X$ denote the total energy and total angular momentum of the spin state Y by method X (X = UHF, UDFT), respectively, and S_{max} is the spin size of the HS state. The first scheme $J_{ab}^{(1)}$ has been derived by Ginsberg [28], Noodleman [29], and Davidson [30] (GND), while the second scheme $J_{ab}^{(2)}$ has been proposed by GND, Bencini [31], Ruiz [32] (BR) and co-workers. Scheme $J_{ab}^{(1)}$ is derived under the assumption that the overlap of magnetic orbitals is sufficiently small (weak orbital interaction region), while $J_{ab}^{(2)}$ is applicable when the overlap is sufficiently large (strong orbital interaction region). The third scheme $J_{ab}^{(3)}$ has been formulated by using our AP procedure [19–25]. The strength of the overlap varies J_{ab} ($J_{ab}^{(3)}$) from $J_{ab}^{(1)}$ to $J_{ab}^{(2)}$.

The above BS results should be examined using the symmetry-adapted multiconfiguration methods for quantitative purpose.   The configuration interaction (CI) type methods such as the complete active space (CAS) CI are applicable in order to elucidate not only reliability of the BS DFT approaches but also spin alignment mechanisms. J_{ab} values can be calculated using the energy gap between symmetry-adapted LS and HS states as follows:

$$J_{ab}(\text{CASCI}) = \frac{{}^{LS}E_{CASCI} - {}^{HS}E_{CASCI}}{S_{HS}(S_{HS}+1) - S_{LS}(S_{LS}+1)},$$

(13)

where ${}^{Y}E_{CASCI}$ denotes the total energy of the spin state Y by the CASCI method [10, 11].   The eq. (12c) is reduced to eq. (13) if the spin contamination in UHF and UDFT is small.   The CASCI can be used to elucidate the SOMO–SOMO and SP plus other contributions to effective exchange integrals.

Generally, the solutions in the LS state by UDFT methods suffer from spin contamination of higher spin states.   Our AP procedure can be applied to evaluate the total energy of the LS state eliminated spin contamination.   The total energy in the LS state is given by the AP scheme [33, 34] as

$$^{AP\text{-}LS}E_X = {}^{LS}E_X + J_{ab}(\text{AP-X})\left[{}^{LS}\langle S^2\rangle_X - S_{min}(S_{min}+1)\right],$$

(14)

where S_{min} is the spin angular momentum of the pure LS state.   This equation is derived from removal of a major part of the spin contamination errors so as to use it to depict the whole potential energy curves.

2.3. Natural orbitals and Chemical Indices

2.3.1. Natural orbitals

The molecular orbital (MO) picture is also feasible for elucidation of the origin and ligand coordination effects of the magnetic interaction and dioxygen binding process.   One of the reliable procedures for this purpose is to perform the CASSCF calculations, and natural orbitals (NOs)

obtained by CASSCF solutions are utilized for MO theoretical explanation of magnetic interaction. But it is time-consuming to perform the CASSCF calculations.   Fortunately, the NO analysis of UHF and UDFT solutions is a practical alternative to CASSCF as demonstrated previously [27, 35]. Here, in order to obtain MO-theoretical explanation of the magnetic coupling, the NOs of the UHF, hybrid DFT and pure DFT solutions were determined by diagonalizing their first-order density matrices [36] as

$$\rho(\mathbf{r},\mathbf{r}') = \sum n_i \{\phi_i(\mathbf{r})\}^* \phi_i(\mathbf{r}'),$$ (15)

where n_i denotes the occupation number of NO ϕ_i.   The occupation numbers of bonding and anti-bonding NOs were almost 2.0 and 0.0, respectively, except for the some magnetic NOs, for which the occupation numbers were close to 1.0.   The bonding magnetic orbitals are generally given by the in- and out-of phase combinations of the bonding (ϕ) and antibonding (ϕ^*) UHF NO (UNO) and DFT NO (DNO)

$$\psi_i^{\pm} = \cos\theta\phi_i \pm \sin\theta\phi_i^*,$$ (16)

where θ is the orbital mixing coefficient [25].

The orbital overlap $T_i = \langle \psi_i^+ | \psi_i^- \rangle$ between magnetic orbitals is a measure of the SE interaction, namely $T_i = 0$ for pure metal biradical and $T_i = 1$ for the closed-shell pair [36].   The occupation numbers of the bonding and antibonding UNO and DNO are expressed by the T_i value;

$$n_i = 1 + T_i, \quad n_i^* = 1 - T_i.$$ (17)

The total spin angular momentum for the BS solution is given by

$$^{LS}\langle S^2 \rangle = S_{\min}(S_{\min} + 1) + \sum (1 - T_i^2).$$ (18)

2.3.2. Chemical Indices

13

Since several chemical indices are equally defined by BS solutions as well as the symmetry-adapted (SA) CASCI and CASSCF ones, these indices are useful in terms of the occupation numbers of UNO and DNO in order to investigate the variations of chemical character. For example, the occupation number of the antibonding NO is not zero in the UNO and DNO analysis. Therefore, the effective bond order [37–39] is defined by

$$b_i = \frac{n_i - n_i^*}{2} = T_i.$$ (19)

Classical and quantum information theories and generalized entropies are now well-defined in several different fields to extract information. In chemistry, information entropy (I) [40–43] is employed to express the characteristic of chemical bonds. The Jaynes information entropy is defined by the occupation number of SONOs to express electron correlation

$$I = -n_i \ln n_i,$$ (20a)

The Jaynes information entropy for the spin-restricted DFT solution of closed-shell systems is given by

$$I_C = -2\ln 2.$$ (20b)

Then, the normalized Jaynes information entropy is defined as a measure of correlation correction as

$$I_n = \frac{I_c - I}{I_c}\left(0 \le I_n \le 1\right).$$ (20c)

The I_n value increases with the decrease of T_i in this definition, and it is parallel to the decrease of the effective bond order $\Delta b = 1 - b = 1 - T_i$ as shown below [37–39] The I_n and Δb values are, therefore, responsible for loss of bond information or covalent bonding.

Since the up- and down-spins enter into the different MOs in eq. (16), the spin density index [25a] appears even in the LS state described under the BS approximation as

$$Q = \sqrt{1-\left(T_i\right)^2} = \sqrt{n_i\left(2-n_i\right)}.$$ (21)

This means that the up- and down-spin densities are populated on the left and right copper atoms, respectively.   As discussed previously [27, 37], the sign and magnitude of spin densities are closely related to the spin correlation function instead of real spin densities under the BS approximation.   The antiparallel spin alignment (↑↓ or ↓↑) given by the BS solution, therefore, expresses the singlet-type (antiferromagnetic) spin correlation, which remains after its spin projection into the pure LS state.

On the other hand, the unpaired electron density U is defined as the deviation of the post SA HF and CI wavefunctions from the single Slater determinant [44], and it is also expressed by the occupation number as

$$U = 1 - \left(T_i\right)^2 = n_i\left(2-n_i\right).$$ (22a)

For the BS solution, the magnitude of unpaired electron density is nothing but the deviation of total spin angular momentum from the exact singlet value.   Therefore it is directly related to that of spin density obtained by the singlet BS solution,

$$U = \sqrt{1-\left(T_i\right)^2}\left|Q\right|.$$ (22b)

However, it is noteworthy that the sign of unpaired electron density is always positive in contrast to that of spin density index.   The U values are responsible for nondynamical electron correlations in diradical species.

The CASCI method [10, 11] is well-accepted approach to open-shell species.   Therefore, it is desirable to clarify mutual relations between the CI and BS methods.   The diradical character (Y) is defined by the weight of doubly excited configuration (W_D) involved in the projected BS solution in comparison with CASCI and CASSCF [37] as

15

$$Y = 2W_{\mathrm{D}} = 1 - \frac{2T_i}{1 + T_i^2} = \frac{n_i^2 - 4n_i + 4}{n_i^2 - 2n_i + 2}. \tag{23}$$

Thus, all the chemical indices introduced here are related each other through the occupation numbers of NOs, which can be calculated by both SA such as CASCF and BS solutions.

These indices are used as common criterion for chemical bonds.   The average normalized indices are defined to investigate the σ-, π- and δ-type chemical bonding nature for UHF and UDFT by

$$^{\kappa}I_n = \sum_{i=1}^{N} {}^{\kappa}I_n^i, \tag{24a}$$

$$^{\kappa}Q_n = \frac{1}{N} \sum_{i=1}^{N} {}^{\kappa}Q_i, \tag{24b}$$

$$^{\kappa}U_n = \frac{1}{N} \sum_{i=1}^{N} {}^{\kappa}U_i, \tag{24c}$$

$$^{\kappa}Y_n = \frac{1}{N} \sum_{i=1}^{N} {}^{\kappa}y_i, \tag{24d}$$

where N is the number of κ-type orbitals.

16

References of Part I

[1] Siegbahn, P. E. M. Electronic Structure Calculations for Molecules Containing Transition Metals. In *Adv. Chem. Phys.*; Prigogine, I., Rice, S. A., Eds.; Wiley: New York, 1996; Vol. XCIII, p. 333.

[2] Siegbahn, P. E. M.; Blomberg M. R. A.; Svesson, M. *Chem. Phys. Lett.* **1994**, *223*, 35.

[3] Armentrout, P. B.; Kickel B. L. In *Organometallic Ion Chemistry*, Freiser, B. S., Ed.; Kluwer: Dordrecht, 1995; p.1.

[4] Parr R. G.; Young, W. *Density Functional Theory of Atoms and Molecules*; Oxford University Press: Oxford, 1989.

[5] Trickey, S. B.ed., *Adv. Quantum Chem., Vol.21, Density Functional Theory of Many-Fermion Systems*; Academic Press: San Diego, 1990.

[6] Szabo, A.; Ostlund, N. S. *MODERN QUANTUM CHEMISTRY Introduction to Advanced Electronic Structure Theory* ; McGraw-Hill: New York, 1989.

[7] Møller, C.; Plesset, M. S. *Phys. Rev.* **1934**, *46*, 618.

[8] Head-Gordon, M.; Pople, J. A.; Frisch, M. J. *Chem. Phys. Lett.* **1988**, *153*, 503.

[9] Krishnan, R.; Pople, J. A. *Int. J. Quant. Chem.* **1978**, *14*, 91.

[10] Brooks, B.; Schaefer, H. F. *J. Chem. Phys.* **1979**, *70*, 5092.

[11] Yamaguchi, K.; Ohta, K.; Yabushita, S.; Fueno, T. *Chem. Phys. Lett.* **1977**, *49*, 555.

[12] Cizek, J. *Adv. Chem. Phys.* **1969**, *14*, 35.

[13] Pople, J. A.; Head-Gordon, M.; Raghavachari, K. *J. Chem. Phys.* **1987**, *87*, 5968.

[14] Becke, A. D. *Phys. Rev. A* **1988**, *38*, 3098.

[15] Vosko, S. H.; Wilk L.; Nusair, M. *Can. J. Phys.* **1980**, *58*, 1200.

[16] Lee, C.; Yang, W.; Parr, R. G. *Phys. Rev. B* **1988**, *37*, 785.

[17] Becke, A. D. *J. Chem. Phys.* **1993**, *98*, 5648.

[18] Becke, A. D., *J. Chem. Phys.* **1993**, *98*, 1372.

[19] Salem, L. *Electrons in Chemical Reactions: First Principle*; John Wiley and Sons: New York, 1982; Chapter7.

[20] Yamaguchi, K.; *Chem. Phys. Lett.* **1975**, *33*, 330.

[21] Yamaguchi, K. *Chem. Phys. Lett.* **1979**, *66*, 395.

[22] Yamaguchi, K.; Takahara Y.; Fueno, T. in: V. H. Smith, F. Scheafer III, K. Morokuma (Eds.), *Applied Quantum Chemistry*, D. Reidel, Boston, MA, 1986, p. 155.

[23] Yamaguchi, K.; Okumura, M.; Mori, W.; Maki, J.; Takada, K.; Noro, T. *Chem. Phys. Lett.* **1993**, *210*, 201.

[24] Yamanaka, S.; Kawakami, T.; Nagao, H.; Yamaguchi, K. *Chem. Phys. Lett.* **1993**, *210*, 25.

[25] Soda, T.; Kitagawa, Y.; Onishi, T.; Takano, Y.; Shigeta, Y.; Nagao, H.; Yoshioka, Y; Yamaguchi, K. *Chem. Phys. Lett.* **2000**, *319*, 223.

[26] Kawakami, T.; Yamanaka, S.; Takano, Y.; Yoshioka, Y.; Yamaguchi, K. *Bull. Chem. Soc. Jpn.* **1998**, 71, 2097.

[27] Mitani, M.; Mori, H.; Takano, Y.; Yamaki, D.; Yoshioka Y.; Yamaguchi, K. *J. Chem. Phys.* **2000**, *113*, 4035.

[28] Ginsberg, A. P. *J. Am. Chem. Soc.* **1980**, 102, 111.

[29] Noodleman, L. *J. Chem. Phys.* **1981**, 74, 5737.

[30] Noodleman, L.; Davidson, E. R. *Chem. Phys.* **1986**, 109, 131.

[31] Bencini, A.; Totti, F.; Daul, C. A.; Doclo, K.; Fantucci, P.; Barone, V. *Inorg. Chem.* **1997**, 36, 5022.

[32] Ruiz, E.; Cano, J.; Alvarez, S.; Alemany, P. *J. Comp. Chem.* **1999**, 20, 1391.

[33] Yamaguchi, K.; Jensen, F.; Dorigo, A.; Houk, K. N. *Chem. Phys. Lett.* **1988**, 149, 537.

[34] Yamaguchi, K.; Takahara, Y.; Fueno T.; Houk, K. N.; *Theoret. Chim. Acta* **1988**, 73, 337.

[35] Mitani, M.; Yamaki, D.; Takano, Y.; Kitagawa, Y.; Yoshioka, Y.; Yamaguchi, K. *J. Chem. Phys.* **2000**, 113, 10486.

[36] Yamaguchi, K.; Okumura, M.; Takada, K.; Yamanaka, S. *Int. J. Quant. Chem., Quantum Chemistry Symposium* **1993**, *27*, 501.

[37] Isobe, H.; Takano, Y.; Kitagawa, Y.; Kawakami, T.; Yamanaka, S.; Yamaguchi, K.; Houk, K. N. *Mol. Phys.* in press.

[38] Yamaguchi, K. In *Self-Consistent Field Theory and Applications*; Carbo, R.; Klobukowski, M., Eds.; Elsevier: Amsterdam, 1990.

[39] Nishino, M.; Yamanaka, S.; Yoshioka, Y.; Yamaguchi, K. *J. Phys. Chem. A* **1997**, *101*, 705.

[40] Shannon, C. E. *Bell. Syst. Tech.* **1948**, *27*, 379.

[41] Jaynes, E. In *Papers on Probability, Statics and Statistical Physics*; Rosencrantz, R., Ed.;

Reidel: Dordrecht, 1993, .

[42] Collins, D. M. *Z. Naturforsch* **1993**, *48A*, 68.

[43] Ramírez, J. C.; Soriano, C.; Esquivel, R. O.; Sagar, R. P.; Hô, M.; Smith Jr., V. H. *Phys. Rev. A* **1997**, *56*, 4477.

[44] Takatsuka, K.; Fueno, T.; Yamaguchi, K. *Theor. Chim. Acta* **1978**, *48*, 175.

Part II

Spin Alignment Rule of

Magnetic Interactions for

d-π-p and d-π-d Conjugated System

Including Phenylene Type Bridge

Part II

Chapter 1

General Introduction of Part II

Molecular magnetism is one of the central issues in molecular science. The molecule-based magnetic compounds [1–6] have indeed attracted both experimental and theoretical attentions in relation to possible candidates of ferro- or ferri-magnet, magnetic conductor [7–10], spin-mediated superconductor [11–13] and so on. Their magnetic properties may be also controlled or switched by several procedures such as photo-excitation [14–16]. Molecule-based magnets are not only important for the elucidation of spin alignment mechanisms but also promising as building blocks of magnetic materials from practical viewpoint of materials synthesis. Such bottom-up strategy becomes more and more significant for development of molecule-based electronic, magnetic and optical devices.

In 1967 Itoh and Wasserman et al. independently detected *m*-phenylenebis-(phenylmethylene) with a quintet electronic ground state by electron spin resonance (ESR) [17, 18]. A series of organic molecules consisting of π–π conjugated system with high spin multiplicities in the ground state have been reported ever since [7–10, 19, 20]. From the experimental and theoretical studies of effective exchange interactions in these systems, it has been demonstrated that the highest-spin (HS) ground state arises as a result of both Coulombic exchange and spin polarization (SP) effects. The SP rule predicts that spins with opposite sign appear alternatively at each of the neighboring atom sites in magnetic molecules. Therefore, it is obvious that organic magnetic molecules with ferro(antiferro)-magnetic ground state are *m*(*p* or *o*)-phenylene-bridged molecular structures. This leads to more stable high(low)-spin states with parallel(antiparallel)-spin configuration than lowest (highest)-spin states with antiparallel (parallel)-spin configuration between radical sites. The author investigated the ferromagnetic coupling of spins in *m*-phenylene bridged olygomers and polymers by density functional and molecular orbital treatments in the series of ab initio computational study [7–10].

Active controls of spins in molecular materials by chemical methods such as doping and by physical techniques such as pressure and laser irradiation have been investigated theoretical [14, 21–23] and experimental [24–34] studies in relation to construction of molecular memories and molecular electronic devices. It has been shown that the β-phase of *para*-nitrophenyl-nitronylnitroxide (*p*-NPNN) undergoes a pressure-induced phase transition from ferromagnetic state to antiferromagnetic one [24, 25]. It has also been demonstrated that a photo-induced ferrimagnetism is realized in the iron-cobalt prussian blue analogs and related species [26–28].

The surprising permanent residual enhancement of the magnetic susceptibility of iron-shiff base polymers after laser heating has been shown by Fujiwara et al. [29]. Recently UHF and DFT calculations were carried out to elucidate effective exchange interactions between transition metal ions in prussian blue analogs [30–32]. The pressure effect for the β-phase crystal of *p*-NPNN was theoretically elucidated by investigating variations of effective exchange integrals by possible conformational changes of *p*-NPNN under high-pressure [33]. Switching dynamics of spins in molecular magnets were also investigated by the quantum dynamic simulation [34].

If the spin sources are changed from carbene to transition metal ions, we can utilize the variety of the d-d and d-p interactions, use transition metal ions as bridges of the magnetic compounds, and expect the large spin state. The d-π-p and d-π-d conjugated systems [1–6, 35–39] appear to be one of the most promising candidates for novel molecule-based magnetic materials. In these d-π-p conjugated spin systems constructed of organic free radicals and transition metal ions, organic radicals serve as spin carriers as well as ligands to magnetic metal ions [1–6]. The d-π-d conjugated systems include the transition metal ions as the spin carriers. Therefore, we can design various types of magnetic molecules with parallel and antiparallel spin configurations by suitable combinations of building blocks, since magnetic molecules are constructed with two parts of the spin source and the coupling unit like π-conjugated system. Experimental efforts [1–6, 35–39] to synthesize magnetic dendrimers and polymers [40–46] have been made extensively, and magnetic couplings in these species have been determined by the magnetic measurement techniques [1–6]. However, theoretical studies for of these d-π conjugated magnetic systems have been limited, and the spin alignment mechanism of these systems has not clarified yet.

Magnetism is one of the characteristic properties in strongly electron correlated systems. The d-π-p and d-π-d conjugated complexes under present consideration are regarded as such electron correlated systems. It is desirable to perform post Hartree–Fock (HF) calculations such as coupled-cluster (CCSD(T)) and CASPT2 in order to investigate the magnetic interaction of d-π-p conjugated complexes as in the case of π-π conjugated organic polyradicals [7–10]. However, they are impossible for these large systems. In recent years, density functional (DFT) calculations [47–51] have been performed to large molecules to elucidate various properties such as binding and excitation energies. DFT has been accepted as an alternative approach for the post HF methods. In other series of papers [7–10, 52 ,53], Yamaguchi and co-workers have thoroughly examined the

applicability of DFT to organic polyradicals and magnetic polymers.   They concluded that DFT employing appropriate exchange-correlation functionals are practically useful for elucidation of electronic and magnetic properties of these species.

In Part I, the author has first investigate the magnetic couplings for $Mn(II)(hfac)_2\{di(4-pyridyl)phenylcarbene\}$ and $Cu(II)(hfac)_2\{di(4-pyridyl)phenylcarbene\}$ as the d-π-p conjugated systems and $Mn(II)_2$-pyrimidine, $Cu(II)_2$-pyrimidine and $Mn(II)Cu(II)$-pyrimidine as the d-π-d ones, using UHF, post-HF and DFT methods.   Implication of calculated results has been discussed in relation to the effective exchange integrals, charge and spin density distributions and the shape and symmetry of natural orbitals.   Finally, on the basis of these results, the author has proposed the spin alignment rules for the magnetic couplings of d-π-p and d-π-d conjugated systems via phenylene like bridge in order to predict the magnetic interactions.

Part II

Chapter 2

Magnetic Couplings and Spin Alignment Rule in d-π-p Conjugated System:

Mn(II)(hfac)$_2${di-(4-pyridyl)phenylcarbene}, Cu(II)(hfac)$_2${di-(4-pyridyl)phenylcarbene}

2.1 Introduction

Hybrid-type spin systems in metal complexes consisting of transition metals and organic radicals, d-π-p conjugated system, are of great interest to scientists aiming at construction of molecular magnetic materials [35–39]. For the construction of such molecule-based magnets, it is required to assemble as many spins as possible in the two and three-dimensional mesoscopic network and couple them in a ferro- or ferrimagnetic fashion. Many chemists have employed a strategy of constructing heterospin systems consisting of 3d transition metal ions and free radical 2p spins.

Iwamura, Koga and their collaborators have prepared bis(hexafluoroacetylacetonato(hfac)) manganese(II) coordinated with di(4-pyridyl)phenylcarbene, $Mn(II)(hfac)_2\{di(4-pyridyl)phenylcarbene\}$ (**1a**) and its copper analog, $Cu(II)(hfac)_2\{di(4-pyridyl)phenylcarbene\}$ (**2a**) (see **Figure 2.1**), by photolysis of the precursor transition metal complexes [54–56]. Magnetic measurements on the precursor complex of $Mn(hfac)_2$ or $Cu(hfac)_2$ with diazodi(4-pyridyl)phenylmethane indicated that the effective exchange interaction (J_{ab}) between the transition metal ions M(II) (M = Mn, Cu) through diazodi(4-pyridyl)phenylmethane group is essentially zero, namely $J_{ab}(M(II)-M(II)) \cong 0$. On the other hand, after irradiation to generate the triplet carbene site, the J_{ab} value between Mn(II) and carbene via 4-pyridyl group was found to be about -12.37 cm^{-1} [54], while the J_{ab} value for the Cu(II)-carbene pair was demonstrated to be ferromagnetic [55] Iwamura, Koga and their collaborators further reported that a 1:1 complex of $Mn(II)(hfac)_2$ with (4-pyridyl)phenylcarbene formed helical and zigzag infinite chains with *trans* and *cis* coordinations of pyridyl nitrogen atoms to Mn(II), respectively. The antiferromagnetic exchange coupling parameters (J_{ab}) for the former (**3T**) and latter (**3C**) chains were -16.96 and -24.18 cm^{-1}, respectively. On the other hand, the copper analog (**4T**) with the *trans* coordination structure exhibited the large positive J_{ab} value (46.43 cm^{-1}) [55]. In spite of great development of the experiments on d-π-p conjugated spin systems [1–6, 35–39, 54–56] theoretical works on them at ab initio level are still insufficient.

Very recently [57], Musin and Morokuma investigated the electronic structure, spin density distribution and mechanisms of exchange interactions in the series of complexes of $Cu(II)(hfac)_2$, $Mn(II)(hfac)_2$ and Cr(III)(mesotetraphenylporphyrinato) with 3- and 4-(N-oxyl-tert-

butylamino)-pyridines (3NOPy and 4NOpy). They showed that the contribution of indirect one-center exchange interaction to total exchange interaction in the complexes is predominant and allow one to give a possible explanation of the magnetic properties of such type of the complexes.

In this chapter, the author has performed UHF, DFT (UBLYP), and HF plus DFT hybrid calculations (UB2LYP and UB3LYP) to elucidate the nature of magnetic interactions in Mn(II)(hfac)$_2$\{di(4-pyridyl)phenylcarbene\}   (**1a**)   [54]   and   Cu(II)(hfac)$_2$\{di(4-pyridyl)phenylcarbene\} (**2a**) [55]. Several model complexes (**1b–1e** and **Ia** for **1a** and **2b–2e** and **Ib** for **2a**) for them shown in **Figure 2.1** have been also examined to clarify the ligand coordination effects in the complexes. The NO analysis of the UHF and DFT solutions of **1z** and **2z** (**z** = **a–e**) and CASCI calculations for **Ia** and **Ib** are performed to elucidate relative contributions of spin polarization (SP) and spin delocalization (SD) (or superexchange (SE)) interactions for determination of the sign of J_{ab} values. Implications of the calculated results have been discussed in relation to the photo-induced molecular magnetism of **1z** and **2z** (**z** = **a–e**) [54–56] from the view point of charge and spin density distributions, as well as the shape and symmetry of natural orbitals. Finally, spin alignment rules for d-π-p conjugated polyradicals via SD, SP and other mechanisms are discuss using the calculated results in combination with the experimental results available [54–56].

2.2 Spin Alignment Rules Based on the Configuration Interaction Model

Let us consider the orbital symmetry rule [58] for the d-π-p conjugated systems. Here, we utilize the intermolecular CI [59] picture for **1z** and **2z** (**z** = **a–e**) in order to investigate the mechanism of the effective exchange interactions for **1a** and **2a**. **1z** and **2z** have three magnetic sites. However, reported experimental results [54–56] showed that the J_{ab} values between the nearest neighbors play important roles to determine their magnetic properties. Two radical-site model (**I**) in **Figure 2.2** can be used for theoretical consideration of the effective exchange interactions. The model is formally divided into M(II) (M = Mn and Cu), 4-pyridyl group (pyr) and carbene (C:) fragments as shown in **I** of **Figure 2.2**. The direct exchange interaction between M(II) and :CH in **II** should be essentially zero [60, 61] because of relatively long intersite distance

(R(Mn–CH) > 5.0Å), as shown in **Figure 2.2**. Since the nitrogen site of 4-pyridyl group coordinates to the M(II) ion, the SD [59] mechanism should be operative between the dz^2 (dσ) half-occupied orbital of M(II) and N-lone pair as illustrated in **IIIa** of **Figure 2.2**. The through σ-bond interaction of the dz^2 (dσ) spin via the SP of the σ-bond network of 4-pyridyl group provides net ferromagnetic exchange integrals with π- and σ- radical electrons of carbene group as shown in **IIIb** [59]. The SP mechanism [59] through dπ(M)-π(4-pyridyl)-pπ(carbene) or dσ(M)-π(4-pyridyl)-pπ(carbene) network should provide an antiferromagnetic or a ferromagnetic exchange interaction, respectively, as illustrated in **IIIc** of **Figure 2.2**, where we utilize the spin vector model for pictorial understanding of the SP effect [7–10, 59]. The induced π-spin on N-atom of 4-pyridyl group via the SP mechanism interacts with the dσ- or dπ-orbital spin of M(II) in the ferro and antiferromagnetic manner, respectively. The spin alignment rule via the SP mechanism is therefore reversed for 3-pyridyl group as illustrated in **IIId**.

Next, the author considers the charge transfer (CT) interaction of M(II) with the π-orbitals of 4-pyridyl group as shown in **Figure 2.3**. The effective exchange interactions within CT configurations are antiferromagnetic due to the non-zero overlap integrals of the dπ(Mn(II))-π(second HOMO) or dπ(Mn(II))-π*(LUMO) orbitals, as illustrated in **IVa** and **IVb** of **Figure 2.3**. Their contributions are incorporated by the fourth-order perturbation (PT4) method [59], and these are the origins of the antiferromagnetic SE interactions in the orbital symmetry rule. The ferromagnetic SE interactions are also conceivable because of the orthogonal orbital interactions of π-second HOMO (or π*-LUMO) with other d-orbitals of M(II) such as the dσ orbital as shown in **IVc** and **IVd** of **Figure 2.3**.

Probably the total sum of the SE interactions in the Mn(II) complex (**1z**) remains antiferromagnetic because of the strong dπ-π(π*) orbital overlap integral. On the other hand, the SE interaction should be ferromagnetic in the Cu(II) complex (**2z**) because of the orthogonal dσ and π(π*) orbital interaction in **IVc** and **IVd**. The J_{ab} value for **2z** should be positive because of ferromagnetic SE interaction, in addition to the ferromagnetic SP effect. The orbital symmetry rules are useful for qualitative explanation of the experimental tendency. The selection rule via the SE mechanism for 4-pyridyl group is equally applicable to the Mn(II) or Cu(II) complexes with 3-pyridyl group, since the similar orbital overlap effects in **Figure 2.3** are operative. **Table 2.1** summarizes the SP plus SD (SE) spin alignment rules [10, 59–62], together with the experimental

results available. From **Table 2.1**, the sign of J_{ab} values in the meta-substituted systems is determined by subtle balances of the SP and SE effects. Moreover, quantitative calculations of the J_{ab} values are difficult on the basis of the CT models because of the nonorthogonality problem of the magnetic fragment orbitals [59].

2.3 Computational Method

2.3.1 Geometries of the complexes

The author performed UHF, UBLYP, UB2LYP and UB3LYP calculations for **1a** [54], **2a** [55] and these models (**1b–1e** and **2b–2e**) as shown in **Figure 2.1** by using the Wachters [63] (62111111/3312/32) plus Hay's diffuse basis sets [64] ($\alpha = 0.1054$ for Mn(II) and $\alpha = 0.1491$ for Cu(II)) for M(II), 6-31G* basis sets for C, N, O and F, and 6-31G basis sets for H by Pople et al [65, 66]. Then, the author determined the NO and their occupation numbers using eq. (15). In addition, the author has evaluated the J_{ab} values for **Ia** and **Ib** by UNO CASCI methods, and these results have been utilized for confirmation of the BS calculations and estimate of the contribution between SP and SD effects.

The geometries of **1a** and **2a** (L = hfac and Ph = phenyl group) were taken from the X-ray crystallographic results [54, 55] as shown in **Figure 2.1**. Their full geometry optimizations are impossible in our computer system. The author constructed simplified models (**1b–1e** and **2b–2e**) of **1a** and **2a** as shown in **Figure 2.1**. **1b** and **2b** are obtained by substitution of terminal phenyl groups of **1a** and **2a** (L = hfac and Ph = H) with hydrogen atoms. The geometries of them were the same to **1a** and **2a** except for C–H = 1.08 Å at carbene site. **1c** and **2c** are given by substitution of hfac in **1b** and **2b** with acetylacetone (acac) ligands (L = acac and Ph = H). **1d** and **2d** are constructed by removal of hfac in **1a** and **2a** (L = nothing and Ph = phenyl group). **1e** and **2e** are obtained by removal of hfac in **1c** and **2c** (L = nothing and Ph = H). The calculated results will clarify the roles of coordination ligands for the J_{ab} values.

2.3.2 Spin-adapted calculations

We can select active orbitals for magnetic interactions by using occupation numbers in eq.

29

(15). First, in order to investigate reliability of the BS DFT methods and to estimate direct exchange interaction between SOMOs, the full CI calculations within the seven (three) magnetic orbitals and seven (three) electrons $\{7, 7\}$ ($\{3, 3\}$) were carried out for LS and HS states of molecule **Ia** (**Ib**), and the J_{ab} values were calculated by eqs. (12c) and (13). Next, the full CI calculations were also performed by expanding the number (m) of active UNOs and number (n) of active electrons $\{m, n\}$: $\{11, 11\}$ for **Ia** includes the four π-UNOs of pyridyl group in addition to the seven SOMOs and $\{9, 9\}$ for **Ib** contains the six π-UNOs of pyridyl group with SOMOs.   The UNO CI $\{7, 7\}$ and $\{3, 3\}$ results are responsible for the SOMO–SOMO interactions of **Ia** and **Ib**, respectively.   These full CI calculations within the CAS $\{11, 11\}$ and $\{9, 9\}$ are referred to as UNO CASCI, which incorporates the SP and electron correlation (EC) effect of paired orbitals by the exchange interactions with SOMO electrons and other high-order excitations.   Here, UNO CASCI $\{m, m\}$ were carried out for both the LS and HS states using the UNO obtained from the LS singlet state [10, 59].

2.4 Computational Results of Manganese and Copper Complexes 1 and 2

2.4.1 Calculated J_{ab} values, and charge and spin densities

Table 2.2 summarizes J_{ab} values calculated for the full model (**1a** and **2a**) and simplified models (**1b–1e**, **2b–2c** and **2e**) of the manganese and copper complexes by AP-methods (eq. (12c)). No reasonable UB3LYP and UBLYP results for **2d** and **2e** have been obtained because of the strong charge transfer from 4-pyridyl carbene to Cu(II). The J_{ab} values calculated by the unprojected method (eq. (12b)) are also given in **Table 2.2**.

All the calculated values for **1** are negative in accordance with the experiments [54, 55], showing an antiferromagnetic interaction between Mn(II) and carbene sites via 4-pyridyl group. The UHF underestimates the magnitude of the J_{ab} value for **1**, while the UBLYP overestimates it as compared with the experimental value (-12.37 cm^{-1}) [54]. The J_{ab} values by UB3LYP reproduce the experimental value [54] quantitatively. On the other hand, all the J_{ab} values for **2** show ferromagnetic couplings between Cu(II) and carbene sites via 4-pyridyl group. The J_{ab} values by UB3LYP and UBLYP reproduce the experimental value (46.43 cm^{-1}) [55]. UHF overestimates

the ferromagnetic interaction. UCCSD(T) will be necessary for reliable post HF calculations of the J_{ab} value, though it can not be applied to such large systems. UDFT would be regarded as a practical alternative to UCCSD(T) even in this d-π conjugated system like π-π conjugated one [7–10]. The difference between the magnitude by eqs. (2b) and (2c) is not so large in all the models and methods, since the radical orbitals of **1** and **2** exhibit the small orbital overlaps, as expected for the magnetic materials [7–10]. Since the difference with respect to J_{ab} values is small in model **a–c**, the substitution of phenyl ring with H and CF_3 with CH_3 is not so serious. The magnitude of the J_{ab} values for model **1d** and **1e** is too large as compared with the experimental results [54, 55]. These results indicate the necessity of ligands in order to investigate the magnetic interaction quantitatively.

The Mulliken population analysis [67] is often useful for qualitative discussions of charge densities even in d-p systems [1–6]. **Table 2.3** shows the population of charge densities obtained on metal ion M(II), 4-pyridylcarbene group (4-PC) and ligand parts (hfac and acac) for the LS state of the models **a–e**. The formal charge (2.0) of the divalent manganese ion largely decreases because of the increase of charge transfers (CT) from hfac and acac to M(II). The charge density of Cu(II) is smaller than that of Mn(II), indicating that the CT of **2** is larger than that of **1**. The CT increases in the order: UHF < UB2LYP < UB3LYP < UBLYP. The same tendency is recognized for the CT from 4-PC group to M(II), in accordance with the trend in the magnitude of the calculated J_{ab} values. In comparison to the charge densities for **a–c**, those for **d** and **e** are overestimated, in conformity with the overestimation of the J_{ab} values. The charge distributions are therefore consistent with the conclusion that the reasonable computation of J_{ab} values for **a–c** by using UB3LYP method should be due to the decrease of the electron affinity of M(II) to which $(hfac)_2$ is added, and the SE mechanism is operative to determine the sign of them.

The DFT methods usually provide reasonable spin densities for radical species [68]. **Table 2.4** summarizes the population of spin densities for 4-pyridyl group part of **1a–1e**, together with those on Mn(II) and C of the carbene group. **Table 2.5** lists those of **2a–2c** and **2e**. Their signs for 4-pyridyl group change alternately to show the characteristic of the spin density wave (SDW), except the positive spin densities of Cu1 and N2 for **2** because of the orthgonality between dσ and pπ orbitals. These results correspond to SP effects [7–10]. Judging from the magnitude of the spin density, the UHF overestimates the SP effects of the 4-pyridyl ring. On the other hand,

the hybrid methods, especially UB3LYP, estimate the SP effects of the 4-pyridyl ring by spins on the M(II) and carbene sites appropriately. It is clear that the hybrid methods are appropriate to elucidate the J_{ab} values for the large d-π-p conjugated systems like **1a** and **2a**. The difference with respect to the population of spin density is not so large among **a–c**.

The ab initio calculations concluded that both the SE and SP effects favor the LS and HS ground state of **1** and **2**, respectively, in accordance with the selection rule in **Table 2.1**. This implies that SE and/or SP type explanations of the experiments are feasible for qualitative purpose.

2.4.2 Natural orbitals and orbital interactions

NOs are visualized for pictorial understanding of the SD and SP effects. The NOs for **1a** by UB3LYP are depicted in **Figure 2.4**, while **Figure 2.5** shows the NOs for the HS state of **2a** by UB3LYP. The occupation numbers of HOMO, SOMO and LUMO for LS states of **1a–1e** and those for HS and LS states of **2a–2c** and **2e** by UHF, DFT and their hybrid calculations are summarized in **Table 2.6** and **Table 2.7**, respectively.

From **Figure 2.4**, the NOs of SOMO+4 and SOMO–4 show the dπ-pπ interaction of the d orbital of the Mn(II) ion and the π orbital of the 4-pyridyl ring, indicating that Mn(II) ion and carbene show π-type antiferromagnetic SD or SE interaction via 4-pyridyl ring. The shapes of the three π-NOs (SOMO–4, SOMO+1 and SOMO+4) are indeed explained by the pπ-dπ-pπ orbital interactions of the dπ orbital of Mn(II) and pπ orbitals of bis(carbene) as illustrated in **V** in **Figure 2.6**. The orbital interactions should be similar even in the case of *cis* and *trans* 1:1 Mn(II)(hfac)$_2${(4-pyridyl)carbene} oligomer. The SOMO–3, SOMO+2 and SOMO+3 are regarded as the bonding, nonbonding and antibonding σ-type NOs, and the corresponding T_i value for **1a** by UB3LYP is only 0.004, indicating that the SE interaction via the σ-type interaction is weak.

From **Table 2.6**, the T_i values of SOMO±4 for **1a** are 0.04, 0.06, 0.10 and 0.26 by UHF, UB2LYP, UB3LYP and UBLYP, respectively, indicating that the π-type SOMO–SOMO interaction by UHF is weak, while that of UBLYP is strong. The author found that UHF underestimates the SD (of SE) interactions and UBLYP overestimates them. The small (large) magnitude of J_{ab} value by UHF (UBLYP) is due to small (large) SE effect, while UB3LYP can deal with it appropriately because of 80 % mixing of the BLYP component. The occupation numbers

of the three d-orbitals are 1.0, showing no significant contribution to the SE interaction. The occupation numbers of HOMO and LUMO are 1.862 and 0.138 by UHF, while those are 1.997 and 0.003 by UBLYP, respectively. This indicates the strong SP effect of the closed-shell orbitals under the UHF approximation as illustrated by **IIIc** in **Figure 2.2**, in sharp contrast to the BLYP case. Judging from the occupation numbers, the SP effect is also weak by UB3LYP. The NO analysis clearly demonstrates that the origin of the antiferromagnetic exchange interaction for **1a** is the pπ-dπ-pπ SE interaction as illustrated by **IVa** and **IVb** in **Figure 2.3** and **V** in **Figure 2.6**, together with the SP of π-network [10].

The five NOs for **2a** by UB3LYP in **Figure 2.5** are singly occupied since $S_{max} = 5/2$. The π-type SOMO+2 and SOMO−2 are mainly localized on the right and left pyridylcarbene groups, respectively. The σ-type SOMO+1 and SOMO−1 also show the same tendency, while the nonbonding σ-NO (SOMO+0) is mainly localized on the central Cu(II) plus (hfac)$_2$ group. Considering the orthogonality between the σ and π orbitals in each 4-PC group, the parallel spin alignment is preferable at the carbene site. The ferromagnetic SE interaction of the central σ orbital with the π orbitals is also expected since σ center has the small tails on the carbene sites and the π orbital (SOMO−2) has the small tail on the central Cu(II) ion. The NO analysis clearly indicates an important role of one-center exchange interaction suggested by Musin and Morokuma [57]. **Figure 2.6** illustrates these ferromagnetic SE interactions **VI** and **VII** at the Cu(II) and carbene sites, respectively.

As summarized in **Table 2.7**, the T_i values of SOMO±2 at the LS state of **2a** show that the σ-type antiferromagnetic SE interaction between Cu(II) ion and triplet carbenes via 4-pyridine ring is rather weak even at the UBLYP level. On the other hand, the π-type SE interaction is negligible as can be recognized from the fact that their occupation numbers are 1.0. This situation is quite different from that of **1a**. The occupation numbers of HOMO and LUMO for **2a** by UHF and UBLYP also show the large and small contributions of the SP effect, respectively. The J_{ab} values of **2a** become ferromagnetic since the ferromagnetic Coulombic and SE interactions overweigh the antiferromagnetic σ-type SE interaction, and the ferromagnetic SP effect is also operative. The ab initio calculations are consistent with the SP plus SD rules for **2a** in **Table 2.1**.

However, the exact calculation of relative contributions of the SD and SP effects remains to be a difficult task because they are sensitive to quality of basis sets and extent of correlation

corrections. For example, UNO analysis of **1a** and **2a** indicate that UNO CASCI {9, 9} and {5, 5} are necessary for discussion of the SOMO–SOMO interactions, while UNO CASCI {25, 25} and {21, 21} are inevitable for evaluation of SP and other effects because CAS {18, 18} is responsible for through-bond interactions via the π-network. Since such large CI calculations are impossible, computations of model systems are inevitable.

2.5 Comparisons with the Post HF Results of the Simplest Model Ia, Ib and Ic

As mentioned above, it is desirable to perform post HF calculations as well as UHF, DFT and their hybrid ones in order to elucidate the magnetic interaction for d-π-p conjugated systems. **Table 2.8** summarizes the calculated J_{ab} values for **Ia** and **Ib**, together with those of Mn(II)3-pyridylcarbene (**Ic**). All the calculated J_{ab} values for **Ia** are negative, reproducing the antiferromagnetic interaction determined by the experiment qualitatively [54]. The J_{ab} values by UHF showed a much stronger antiferromagnetic interaction than the experimental value, while its absolute value significantly decreased after the dynamical correlation corrections by UMP2 method. This tendency is attributable to the fact that UMP2 mainly incorporates the CT configurations. Therefore, the fourth-order corrections by UMP4 are crucial for inclusion of antiferromagnetic SE interactions. Inclusion of higher-order corrections such as UCCSD(T) retains the negativity of the J_{ab} values by UCCSD(T) accidentally close to that by UHF. These overshootings might remove if bis(hexafluoroacethylacetone) ligands, (hfac)$_2$, are added to Mn(II) ion since (hfac)$_2$ decreases the electron affinity of Mn(II). However, the UMP4 and UCCSD(T) calculations of such a large system are impossible in our computer system. This trend becomes more remarkable in the case of BLYP and B3LYP. The large negative J_{ab} values are related to the overestimation of the SD effect by BLYP and B3LYP, as usually recognized in other cases. The overestimation was remarkably reduced by the addition of (hfac)$_2$ or (acac)$_2$ ligands to Mn(II). While, all the calculated J_{ab} values for **Ib** show the ferromagnetic interaction determined by the experiments [55, 56]. The UHF calculation correctly reproduces the ferromagnetic J_{ab} value, but their magnitude is several times larger than the experimental value (46.43 cm^{-1}). The author performed DFT calculations of **Ib**, but no reasonable results were obtained because of strong CT from 4-pyridyl

group to Cu(II).   The magnitude by the UMP2(4) value is also too large as compared with the experimental one.   Coordination of ligands such as hfac and acac to M(II) ions removes such overshooting, because $(hfac)_2$ and $(acac)_2$ decrease the electron affinity of M(II) ions, in other words, the charge transfer from 4-PC to M(II) ions.   The calculated results in **Tables 2.2** and **2.8** show that the coordination ligands are crucial in order to estimate the magnetic interaction for these d-π-p conjugated systems.   The UCCSD(T) or QCISD computations of **a–c** should provide the same conclusion, though those are impossible in our computer system.

Both the UNO CASCI{7, 7} for **Ia** and {3, 3} for **Ib** would provide the SOMO–SOMO interaction.   On the other hand, UNO CASCI {11, 11} and {9, 9} include both the SP and higher-order correlation correction (EC) terms [58].   The J_{ab} values via the SOMO–SOMO interactions of **Ia** and **Ib** are –34.36 and 33.80 cm^{-1}, while, the UNO CASCI {11, 11} for **Ia** and {9, 9} for **Ib** are –26.99 and 48.87 cm^{-1}, respectively.   Using the J_{ab} values by CASCI calculations, we can estimate the SP and EC effects by π-orbital in pyridine ring.   These effects are 7.37 for **Ia** and 15.07 for **Ib**, respectively, and smaller than SOMO–SOMO interactions, also showing that SP and EC effects are less effective for the magnetic interaction of **Ia** and **Ib**.

The J_{ab} values for **Ic** by UHF and UCCSD(T) are positive, in accordance with the topological rule [1–10, 19, 70, 71] based on the SP effect, but they are negative under the UMP2(4) approximation.   The tendency is similar to that of *m*-phenylene-bridged polyradicals [7–10].   The UBLYP and UB3LYP also predict the large negative J_{ab} values because of the large estimation of the SE interaction.   The large estimation by DFT is responsible for the loss of ligand coordination. The magnitude of the calculated J_{ab} values would be largely decreased by the coordination of ligands to Mn(II).   The J_{ab} value by UNO CASCI {7, 7} for **Ic** indicates small antiferromagnetic interaction between SOMOs because of the SE interactions, while that by UNO CASCI {11, 11} shows small ferromagnetic interaction because of the inclusion of SP and EC interactions.   The CASCI computations clearly demonstrate that SD and (SP+EC) effects are competitive for *m*-phenylene bridged d-p complexes, supporting the selection rule in **Table 2.1**.   The sign of J_{ab} should be dependent on ligands and conformational effects of phenyl group as well as radical groups in these systems.   In fact, the experimental results by Koga and Iwamura group [19, 54–56] showed that the J_{ab} values of the *meta* analogs of **1, 2** and **3** are essentially zero because of this competition.   On the other hand, the SP effect is predominant for Cr(III) complex with *m*-

35

phenylene radical as discussed below.

2.6 Discussions and Concluding Remarks

2.6.1 Difference for the magnetic interaction between Mn(II) and Cu(II) ions

The author discusses the difference for the J_{ab} values between Mn(II) and Cu(II) ions using the intermolecular CI model and the above results.   Since Mn(II) ion in **1** contains five unpaired d electrons, Mn(II) complex **1** show dπ-pπ, dσ-pσ and dσ-pπ interactions.   NO analysis of **1a** and CASCI calculation for the simplest model **Ia** show that dπ-pπ interaction is more effective to the magnetic interaction than other interactions.   Judging from the intermolecular CI model, Mn(II)–carbene complex **1a** shows an antiferromagnetic coupling because the dπ-pπ interaction gives rise to an antiferromagnetic interaction.   On the other hand, Cu(II) ion in **2** contains one unpaired d electron which occupied dz^2 orbital.   NOs and their occupation numbers of **2a** and CASCI calculation of **Ib** indicate the d unpaired electron contributes to dσ-pσ and dσ-pπ .   According to the CI model, the dσ-pσ and dσ-pπ couplings for **2a** provide a ferromagnetic interaction.

In conclusion, the difference of the symmetries [58] of magnetic orbitals occupied by d unpaired electrons between Mn(II) and Cu(II) give rise to the difference of orbital interaction; dπ-pπ interaction or dσ-pσ and dσ-pπ interactions, leading to the antiferromagnetic interaction of **1** and ferromagnetic interaction of **2**.

2.6.2 Dependence of the model on the magnetic interaction for 1 and 2

Here, the author considers the model dependence on the J_{ab} values and charge and spin density distributions in order to understand what controls the magnetic interaction.   The J_{ab} value and charge and spin density distributions for **a–c** are similar, indicating that the change of groups from hfac to acac or from phenyl group to H is hardly effective to these properties.   No hfac or acac ligand model can not provide the appropriate charge or spin density distributions.   **1b**, **1c** and **2c** obtained by addition of acac ligand to **1d**, **1e** and **2e** show the proper J_{ab} values and charge and spin density distributions.   Compared with **Ia** and **1e**, the J_{ab} values are reduced from –281.2 to

36

-73.76 cm^{-1} by the UB3LYP method. The author finds that the coordination effect of 4-PC to Mn(II) ion plays a key role in the J_{ab} values for **1**. NOs in **Figure 2.5** also show that the coordination effect of 4-PC is important for the J_{ab} value. In addition, the J_{ab} value is close to the experimental result, when the ligand such as hfac and acac are coordinated to Mn(II).

Then it is concluded that both the ligand coordination effects of 4-pyridylcarbene and hfac or acac play crucial role for the determination the J_{ab} values, but the ligand coordination effect of hfac or acac is more important for the active control of charge and spin density distributions.

2.6.3 Spin alignment rules in d-π-p conjugated polyradicals

Recently, several transition metal-radical complexes have been synthesized, and their magnetic properties have been elucidated experimentally [1–6, 54–56]. **Figure 2.8** illustrates the molecular structures of such species (**1Z–12Z**), which are classified into *p*-phenylene and *m*-phenylene types, depending on the positions of radical groups: phenyl carbene group (**A**) and *t*-butyl nitroxide (**B**). **Table 2.1** summarizes the observed J_{ab} values for **1Z–12Z**. It is seen from **Table 2.1** and present theoretical results that both the SE and SP effects favor the LS ground state of 1:2 Mn(II)(hfac)$_2$(*p*-phenylene type radical)$_2$ complexes and 1:1 Mn(II)(hfac)$_2$(*p*-phenylene type radical) polymers (oligomers), predicting the total negative (antiferromagnetic) J_{ab} values. The experimental results [54–56] are completely compatible with the SP plus SD rules [7–10, 59, 68, 69] for molecular magnets. On the other hand, the sign of the total J_{ab} values is determined by subtle balances between the SD ($J < 0$) and SP ($J > 0$) effects in the cases of 1:2 Mn(II)(hfac)$_2$(*m*-phenylene type radical)$_2$ complexes and 1:1 Mn(II)(hfac)$_2$(*m*-phenylene type radical) polymers (oligomers). The experimental χT plots for these species [54–56] indicated that the J_{ab} values are essentially zero.

Both the SD and SP effects predict the ferromagnetic exchange interactions in the cases of 1:2 Cu(II)(hfac)$_2$(*p*-phenylene type radical)$_2$ complexes and 1:1 Cu(II)(hfac)$_2$(*p*-phenylene type radical) polymers (oligomers). The available experimental results are consistent with the SP plus SD rule as shown in **Table 2.1**. On the other hand, the SD and SP effects are competitive in the cases of the corresponding *m*-phenylene type radical complexes such as **8B**. The experiments for **8B** demonstrated the total antiferromagnetic interaction, leading to the conclusion that the SP effect overweighs the SD effect in the Cu(II) complexes with *m*-phenylene bridge.

The SP plus SD rules in **Table 2.1** are consistent for the experimental results for tetraphenylporphyrine (TPP) chromium(III) complexes with *p-* or *m-* phenylene type radical (**11B** and **12B**). The observed J_{ab} value for the *p*-isomer (**11B**) was antiferromagnetic because of dπ-pπ interaction as **1**, while it became ferromagnetic for the *m*-isomer (**12B**).

Design of magnetic polymers and dendrimers [1–6, 19, 40–46] is also feasible on the theoretical and experimental grounds as summarized in **Table 2.1**. In fact, many applications of these rules to d-p conjugated polyradicals are conceivable. Synthesis of such novel systems is interesting not only for photo-induced magnetism but also for magnetooptics [70] and optoelectronics [71, 72]. Bose-Einstein condensation of singlet or triplet exciton [73] will be an interesting future problem in these dendrimers [74].

2.6.4 Application of approximately spin projection method for BS DFT solution

The AP-scheme in eq. (14) is applicable to full or partial geometry optimizations of the Mn(II) complexes **1z** (**z** = **a–c**) and Cu(II) complexes **2z** (**z** = **a–c**), though we have not performed such expensive computations. From the experimental J_{ab} values for **1a**, **3T** and **3C** presented in **Table 2.1**, it is clear that their magnitude is sensitive to geometries and solid state structures, though the sign is not changed. Therefore, the geometry optimizations of **1z** (**z** = **a–c**) and **2z** (**z** = **a–c**) are interesting future problems for quantitative calculations of J_{ab} values. Applications of the AP-scheme to radical reactions [75–77] have attracted recent interest in relation to biologically important binuclear transition metal complexes involved in enzymes [75–77]. Since the J_{ab} values for these complexes have been determined experimentally, the AP-DFT calculations of them are effective for examination of reliabilities of the DFT solutions (UBLYP, UB3LYP and others) for searching transition structures of enzyme reactions.

2.6.5 Concluding remarks

UHF, DFT and HF plus DFT hybrid calculations were performed for **1a**, **2a** and their models to elucidate the mechanisms of the effective exchange interactions between transition metal ion and carbene sites. The natural orbital (NO) analyses of these solutions followed by UNO CASCI are very useful for the purpose. The author concluded as follows: (i) Mn(II) complex **1a** shows an antiferromagnetic interaction because of the π-type antiferromagnetic SE effect and the π-

type SP effect; (ii) the positive J_{ab} value for Cu(II) complex **2a** is explained by the fact that ferromagnetic SE interactions due to orbital orthogonality and the σ-type ferromagnetic SP effect are more effective than the σ-type antiferromagnetic SE interaction; (iii) both the ligand coordination effects play crucial role in the J_{ab} value; (iv) the ligand coordination effect of hfac is important to the appropriate charge or spin densities; (v) the UB3LYP calculation provides reasonable effective exchange integrals for **1a** and **2a**; (vi) the SP plus SD (SE) rules in **Table 2.1** are reliable on the theoretical grounds, together with the experiments available.

Table 2.1.   Spin alignment rules and experimental results for several d-π-p conjugated systems

Metal	Type	SD (SE)	SP	Total	Experimental results[a,b]		
$Mn(II)(hfac)_2$	*para*	$J_{SD} < 0$	$J_{SP} < 0$	$J_{TOTAL} < 0$	**1A** (–12.4),	**3T** (–17.0),	**9A** ($J < 0$)
					1B (–8.62),	**3C** (–24.2),	**9B** (–17)
$Cu(II)(hfac)_2$	*para*	$J_{SD} > 0$	$J_{SP} > 0$	$J_{TOTAL} > 0$	**2A** ($J > 0$),	**2B** (40.7),	**4T** (46.4),
					6B (2.96),	**10A** ($J > 0$),	**10B** (47)
	meta	$J_{SD} > 0$	$J_{SP} < 0$	$J_{TOTAL} > 0$ or < 0	**8B** ($J < 0$)		
$Cr(III)(TPP)$	*para*	$J_{SD} < 0$	$J_{SP} < 0$	$J_{TOTAL} < 0$	**11B** (–53.6)		
	meta	$J_{SD} < 0$	$J_{SP} > 0$	$J_{TOTAL} > 0$ or < 0	**12B** (8.5)		

[a]The observed J_{ab} values (cm^{-1}) are given in parentheses.   [b]The molecular structures for **1Z–12Z** are given in **Figure 2.7**.

Table 2.2. Effective exchange integrals $(J_{ab}(\text{AP-X}))^a$ calculated for $Mn(II)(hfac)_2\{di(4$-pyridyl)phenylcarbene$\}$ (**1z**) and $Cu(II)(hfac)_2\{di(4$-pyridyl)phenylcarbene$\}$(**2z**) (**z** = **a–e**) by UHF and DFT methods[b, c]

| | Method | Ligands z | | | | |
		a	**b**	**c**	**d**	**e**
1z[d]	UHF	–2.722	–2.640	–1.922	–27.86	–28.81
		(–2.723)	(–2.640)	(–1.923)	(–27.78)	(–28.73)
	UB2LYP	–7.734	–5.272	–4.900	–31.66	–23.32
		(–7.746)	(–5.272)	(–4.900)	(–31.70)	(–23.32)
	UB3LYP	–10.06	–8.576	–8.637	–187.7	–73.76
		(–10.07)	(–8.580)	(–8.641)	(–192.1)	(–74.32)
	UBLYP	–18.78	–21.01	–74.18	–280.1	*f*
		(–18.71)	(–21.07)	(–75.15)	(–288.9)	*f*
2z[e]	UHF	134.9	135.8	135.6	*f*	35.90
		(136.0)	(136.9)	(136.7)	*f*	(35.98)
	UB2LYP	71.82	73.87	73.06	*f*	104.3
		(72.19)	(74.22)	(73.43)	*f*	(102.4)
	UB3LYP	67.14	66.15	64.20	*f*	*f*
		(67.29)	(66.33)	(64.36)	*f*	*f*
	UBLYP	63.46	61.06	48.81	*f*	*f*
		(63.55)	(61.19)	(49.02)	*f*	*f*

$^aJ_{ab}$ are by eq. (12c) shown in cm^{-1}. ^{b}The geometries were taken from Ref. 54 and 55. $^cJ_{ab}(X)$ values by eq. (13) are given in parentheses. $^dJ_{ab}$ by the experiment is -12.37 cm^{-1}. $^eJ_{ab}$ by the experiment is 46.43 cm^{-1}. ^{f}The calculations were not converged.

Table 2.3. Charge densities calculated for the lowest-spin state of Mn(II)(hfac)₂{di(4-pyridyl)phenylcarbene} (**1z**) and Cu(II)(hfac)₂{di(4-pyridyl)phenylcarbene} (**2z**) (**z** = **a–e**) by the UHF, UB2LYP, UB3LYP, UBLYP and UBLYP methods

M	Method	a M	a 4-PC[a]	a hfac[b]	b M	b 4-PC[a]	b hfac[b]	c M	c 4-PC[a]	c acac[c]	d M	d 4-PC[a]	e M	e 4-PC[a]
Mn(II)(**1z**)	UHF	1.703	0.005	−0.856	1.703	0.004	−0.856	1.692	0.008	−0.837	1.653	0.174	1.660	0.170
	UB2LYP	1.433	0.051	−0.767	1.434	0.049	−0.766	1.421	0.033	−0.743	1.450	0.275	1.477	0.261
	UB3LYP	1.258	0.076	−0.704	1.259	0.073	−0.702	1.244	0.055	−0.676	1.083	0.459	1.267	0.367
	UBLYP	1.111	0.090	−0.645	1.112	0.085	−0.641	1.112	−0.002	−0.567	0.906	0.547	*d*	*d*
Cu(II)(**2z**)	UHF	1.583	0.073	−0.861	1.584	0.072	−0.860	1.584	0.052	−0.841	*d*	*d*	1.441	0.280
	UB2LYP	1.243	0.149	−0.770	1.248	0.145	−0.767	1.243	0.121	−0.742	*d*	*d*	1.190	0.405
	UB3LYP	1.003	0.195	−0.656	1.004	0.190	−0.691	0.998	0.160	−0.657	*d*	*d*	*d*	*d*
	UBLYP	0.825	0.213	−0.626	0.826	0.204	−0.617	0.822	0.171	−0.582	*d*	*d*	*d*	*d*

[a] 4-PC = 4-pyridylcarbene. [b] hfac = hexafluoroacetylacetone. [c] acac = acetylacetone. [d] The calculations were not converged.

Table 2.4. Spin densities calculated for the LS state of Mn(II)(hfac)$_2${di(4-pyridyl)phenylcarbene} (**1z**) (**z** = **a**–**e**) by the UHF, UB2LYP, UB3LYP and UBLYP methods

Methods	Models	Mn1[a]	N2[a]	C3[a]	C4[a]	C5[a]	C6[a]	C7[a]	C8[a]
UHF	**1a**	4.945	−0.594	0.632	−0.726	0.829	−0.745	0.643	−2.074
	1b	4.945	−0.603	0.642	−0.739	0.850	−0.759	0.650	−2.137
	1c	4.942	−0.615	0.649	−0.742	0.856	−0.762	0.658	−2.139
	1d	5.094	−0.485	0.465	−0.582	0.673	−0.608	0.479	−2.008
	1e	5.093	−0.505	0.492	−0.616	0.722	−0.641	0.504	−2.100
UB2LYP	**1a**	4.842	−0.203	0.175	−0.266	0.289	−0.285	0.179	−1.733
	1b	4.842	−0.221	0.192	−0.292	0.332	−0.314	0.193	−1.909
	1c	4.839	−0.225	0.192	−0.291	0.334	−0.313	0.194	−1.911
	1d	5.012	−0.184	0.060	−0.157	0.143	−0.179	0.065	−1.600
	1e	5.027	−0.194	0.096	−0.203	0.232	−0.226	0.098	−1.858
UB3LYP	**1a**	4.775	−0.128	0.086	−0.179	0.171	−0.198	0.087	−1.620
	1b	4.774	−0.141	0.098	−0.201	0.210	−0.225	0.097	−1.839
	1c	4.767	−0.144	0.098	−0.200	0.211	−0.223	0.097	−1.840
	1d	4.628	−0.130	0.005	−0.010	0.058	−0.114	0.006	−1.389
	1e	4.893	−0.142	0.029	−0.132	0.134	−0.155	0.028	−1.738
UBLYP	**1a**	4.632	−0.089	0.037	−0.131	0.100	−0.151	0.036	−1.504
	1b	4.638	−0.100	0.045	−0.151	0.135	−0.177	0.043	−1.759
	1c	4.454	−0.107	0.041	−0.140	0.126	−0.165	0.039	−1.666
	1d	4.495	−0.120	−0.001	−0.086	0.036	−0.105	−0.002	−1.297

[a]These site numbers are shown in **I** of **Figure 2.2**.

Table 2.5.   Spin densities calculated for the LS state of Cu(II)(hfac)$_2${di(4-pyridyl)phenylcarbene} (**1z**) (**z** = **a–e**) by the UHF, UB2LYP, UB3LYP and UBLYP methods

Methods	Models	Mn1[a]	N2[a]	C3[a]	C4[a]	C5[a]	C6[a]	C7[a]	C8[a]
UHF	**2a**	0.872	0.648	–0.619	0.757	–0.843	0.728	–0.643	2.071
	2b	0.872	0.654	–0.624	0.761	–0.844	0.736	–0.649	2.100
	2c	0.874	0.674	–0.641	0.772	–0.857	0.746	–0.666	2.102
	2e	0.957	0.446	–0.439	0.608	–0.679	0.590	–0.467	2.051
UB2LYP	**2a**	0.787	0.318	–0.185	0.327	–0.311	0.292	–0.196	1.724
	2b	0.787	0.328	–0.197	0.345	–0.342	0.311	–0.211	1.864
	2c	0.787	0.330	–0.201	0.346	–0.347	0.311	–0.215	1.867
	2e	0.899	0.229	–0.092	0.249	–0.224	0.221	–0.102	1.805
UB3LYP	**2a**	0.654	0.271	–0.092	0.239	–0.186	0.204	–0.100	1.609
	2b	0.654	0.274	–0.097	0.251	–0.213	0.216	–0.108	1.792
	2c	0.645	0.269	–0.098	0.251	–0.216	0.214	–0.109	1.794
UBLYP	**2a**	0.545	0.250	–0.050	0.203	–0.121	0.167	–0.056	1.570
	2b	0.545	0.250	–0.052	0.215	–0.144	0.177	–0.062	1.726
	2c	0.544	0.241	–0.047	0.208	–0.141	0.169	–0.056	1.721

[a]These site numbers are shown in **I** of **Figure 2.2**.

Table 2.6. Occupation numbers of the natural orbitals for the LS state of $Mn(II)(hfac)_2\{di(4-$pyridyl)phenylcarbene\} (**1z**) (**z** = **a–e**) by the UHF, UB2LYP, UB3LYP and UBLYP methods

Method	Model	HOMO	SOMO–4	SOMO–3	SOMO–2 to +2	SOMO+3	SOMO+4	LUMO
UHF	**1a**	1.862	1.038	1.001	1.000	0.999	0.962	0.138
	1b	1.867	1.040	1.002	1.000	0.998	0.960	0.133
	1c	1.866	1.039	1.002	1.000	0.998	0.961	0.134
	1d	1.876	1.051	1.003	1.000	0.997	0.949	0.124
	1e	1.906	1.049	1.003	1.000	0.997	0.951	0.094
UB2LYP	**1a**	1.980	1.062	1.002	1.000	0.998	0.938	0.020
	1b	1.979	1.063	1.004	1.000	0.996	0.937	0.021
	1c	1.979	1.063	1.004	1.000	0.996	0.937	0.021
	1d	1.986	1.176	1.010	1.000	0.990	0.824	0.014
	1e	1.986	1.120	1.008	1.000	0.992	0.880	0.014
UB3LYP	**1a**	1.993	1.103	1.004	1.000	0.996	0.897	0.007
	1b	1.992	1.103	1.009	1.000	0.991	0.897	0.008
	1c	1.992	1.109	1.011	1.000	0.989	0.981	0.008
	1d	1.994	1.671	1.018	1.000	0.982	0.329	0.006
	1e	1.993	1.390	1.021	1.000	0.979	0.610	0.007
UBLYP	**1a**	1.997	1.263	1.046	1.000	0.954	0.737	0.003
	1b	1.997	1.237	1.054	1.000	0.946	0.763	0.003
	1c	1.997	1.497	1.098	1.000	0.902	0.503	0.003
	1d	1.994	1.786	1.040	1.000	0.960	0.214	0.006

Table 2.7.   Occupation numbers of the natural orbitals for the LS (HS)[a] state of Cu(II)(hfac)$_2${di(4-pyridyl)phenylcarbene} (**2z**) (**z** = **a–e**) by the UHF, UB2LYP, UB3LYP and UBLYP methods

Method	Model	HOMO	SOMO–2	SOMO–1 to 1	SOMO+2	LUMO
UHF	**2a**	1.869 (1.866)	1.001 (1.000)	1.000 (1.000)	0.999 (1.000)	0.131 (0.134)
	2b	1.872 (1.868)	1.002 (1.000)	1.000 (1.000)	0.998 (1.000)	0.128 (0.132)
	2c	1.867 (1.863)	1.002 (1.000)	1.000 (1.000)	0.998 (1.000)	0.133 (0.137)
	2e	1.918 (1.916)	1.011 (1.000)	1.000 (1.000)	0.989 (1.000)	0.082 (0.084)
UB2LYP	**2a**	1.980 (1.978)	1.005 (1.000)	1.000 (1.000)	0.995 (1.000)	0.020 (0.022)
	2b	1.977 (1.974)	1.008 (1.000)	1.000 (1.000)	0.992 (1.000)	0.023 (0.026)
	2c	1.977 (1.974)	1.008 (1.000)	1.000 (1.000)	0.992 (1.000)	0.023 (0.026)
	2e	1.978 (1.985)	1.088 (1.000)	1.000 (1.000)	0.912 (1.000)	0.022 (0.015)
UB3LYP	**2a**	1.993 (1.992)	1.013 (1.000)	1.000 (1.000)	0.987 (1.000)	0.007 (0.008)
	2b	1.992 (1.990)	1.021 (1.000)	1.000 (1.000)	0.980 (1.000)	0.008 (0.010)
	2c	1.992 (1.990)	1.021 (1.000)	1.000 (1.000)	0.979 (1.000)	0.008 (0.010)
UBLYP	**2a**	1.997 (1.996)	1.034 (1.000)	1.000 (1.000)	0.966 (1.000)	0.003 (0.004)
	2b	1.997 (1.996)	1.055 (1.000)	1.000 (1.000)	0.945 (1.000)	0.003 (0.004)
	2c	1.997 (1.996)	1.114 (1.000)	1.000 (1.000)	0.886 (1.000)	0.003 (0.004)

[a]Occupation numbers for the HS state are shown in parentheses.

Table 2.8. Effective exchange integrals $(J_{ab})^a$ calculated for Mn(II)(4-pyridyl)carbene (**Ia**), Cu(II)(4-pyridyl)carbene (**Ib**) and Mn(II)(3-pyridyl)carbene (**Ic**) by the UHF, UMP2(4), UCCSD(T), DFT and CASCI methods

Method	Ia[b]		Ib[c]		Ic	
	$J_{ab}(X)$	$J_{ab}(AP\text{-}X)$	$J_{ab}(X)$	$J_{ab}(AP\text{-}X)$	$J_{ab}(X)$	$J_{ab}(AP\text{-}X)$
Broken-symmetry						
UHF	−65.42	−65.70	184.4	181.6	58.54	58.23
UMP2	−8.377	−8.401	202.1	200.0	−15.77	−15.71
UMP4	−22.24	−22.31	320.8	317.4	−6.762	−6.734
UCCSD(T)	−56.50	−56.67	229.2	231.6	3.110	3.097
UB2LYP	−94.34	−93.94			12.83	12.79
UB3LYP	−288.9	−281.2			−174.3	−169.5
UBLYP	−511.3	−488.9			−292.7	−280.7
Symmetry-Adapted						
UNO CASCI {SOMO–SOMO}[d]		−34.36		33.80		−0.197
UNO CASCI {m, m}[e]		−26.99		48.87		3.862

[a] J_{ab} are shown in cm⁻¹. [b] J_{ab} by experiment is −12.37 cm⁻¹. [c] J_{ab} by experiment is 46.43 cm⁻¹.
[d] SOMO = 7 for **Ia** and **Ic**, and SOMO = 3 for **Ib**. m = 11 for **Ia** and **Ic**, and m = 9 for **Ib**.

1z (z = a–e)

1a	L = hfac
	Ph = phenyl group
1b	L = hfac
	Ph = H
1c	L = acac
	Ph = H
1d	L = nothing
	Ph = phenyl group
1e	L = nothing
	Ph = H

H F O C N Mn

2z (z = a–e)

2a	L = hfac
	Ph = phenyl group
2b	L = hfac
	Ph = H
2c	L = acac
	Ph = H
2d	L = nothing
	Ph = phenyl group
2e	L = nothing
	Ph = H

H F O C N Cu
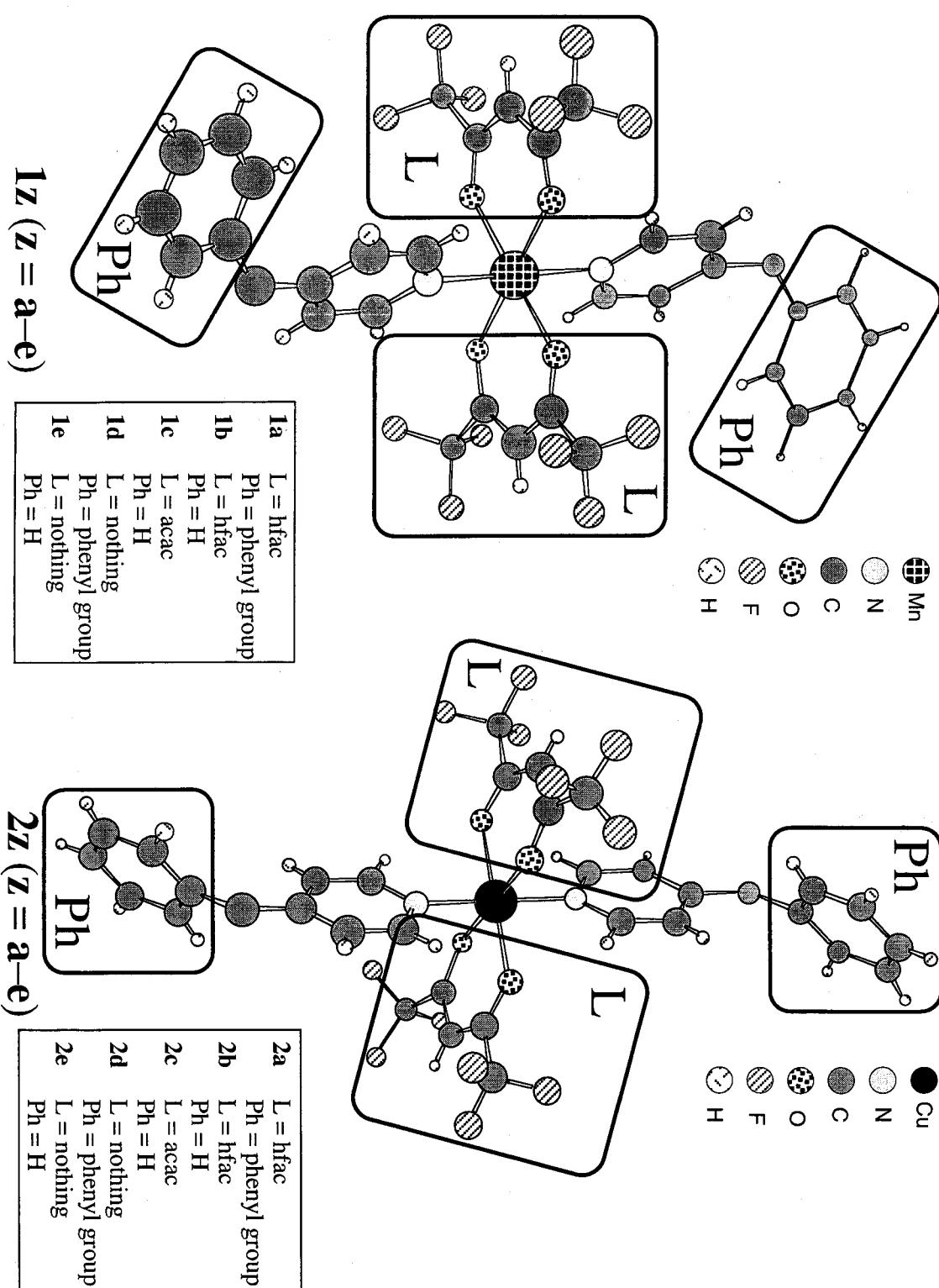
Figure. 2.1   The molecular structures of Mn(II)(hfac)$_2${di(4-pyridyl)phenylcarbene} (1a), Cu(II)(hfac)$_2${di(4-pyridyl)phenylcarbene} (2a), and the model complexes (1b–1e) and (2b–2e) for 1a and 2a, respectively.
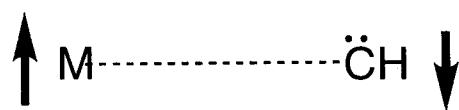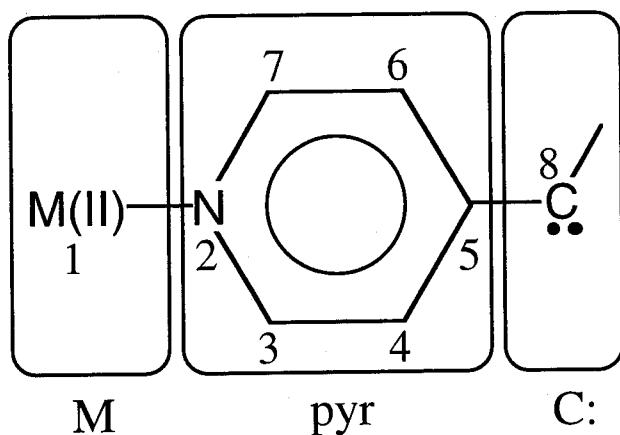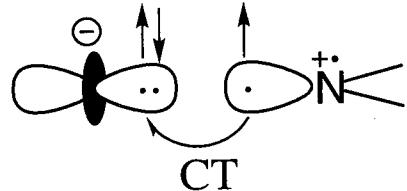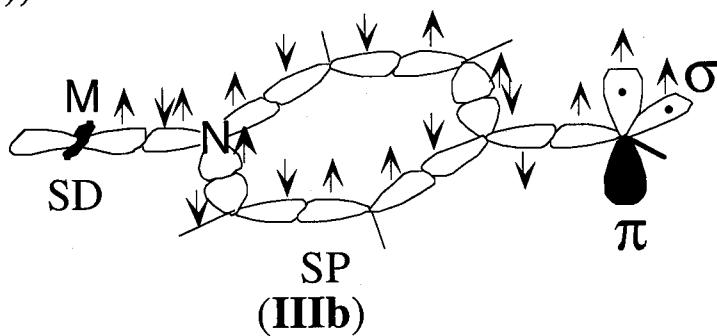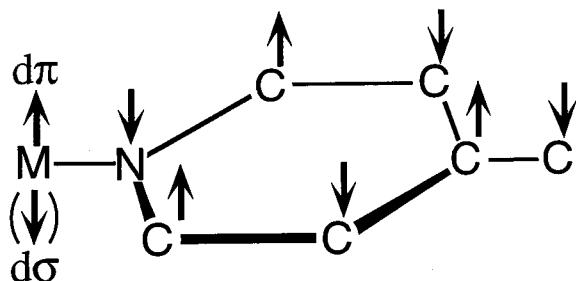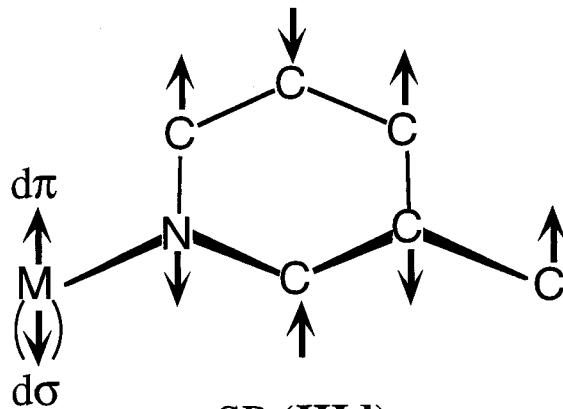
Figure 2.2. Through-bond interaction model of M(II)(4-pyridyl)carbene (**I**), direct effective exchange interaction (**II**) between transition metal ion (M) and CH, spin delocalization (SD) mechanism (**IIIa**) between dσ-electron of transition metal ion (M) and lone pair electrons of nitrogen atom in 4-pyridyl ring, the σ-type spin polarization (SP) mechanism (**IIIb**) through the 4-pyridyl ring for σ- and π-electrons of triplet carbene, the π-type SP interactions (**IIIc** and **IIId**) of 4- and 3-pyridylcarbenes with dσ- or dπ-electron of M(II).

Mn(II) (pyd)$^{+\bullet}$ $^{\ominus}$CH

IVa

dπ

second HOMO

(Nonorthogonal; <d|π> ≠ 0)

Mn(II) (pyd)$^{-\bullet}$ $^{\oplus}$CH

IVb

dπ

LUMO

(Nonorthogonal; <d|π> ≠ 0)

Cu(II) (pyd)$^{+\bullet}$ $^{\ominus}$CH

IVc

dσ

second HOMO

(Orthogonal; <d|π> = 0)

Cu(II) (pyd)$^{-\bullet}$ $^{\oplus}$CH

IVd

dσ

LUMO
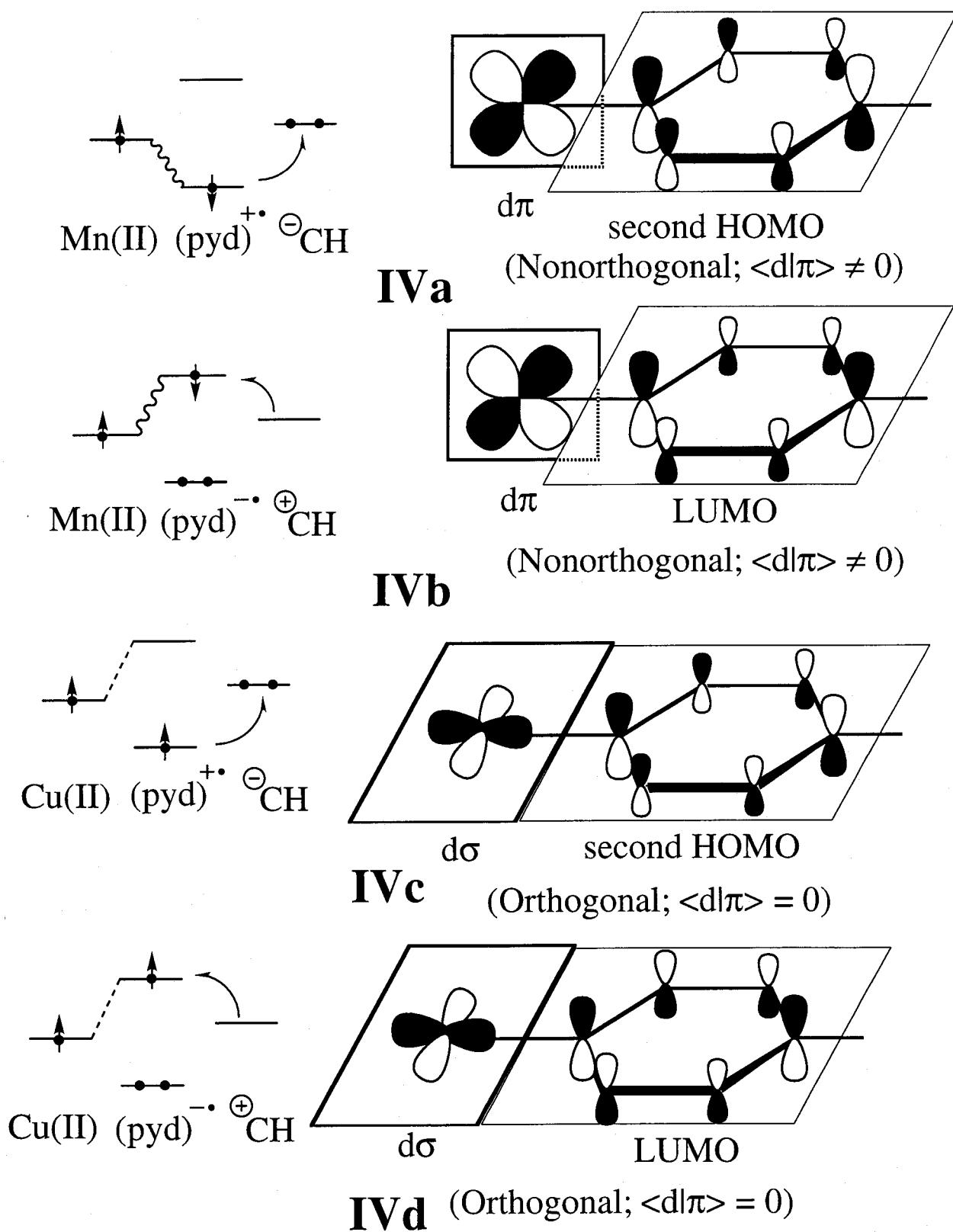
(Orthogonal; <d|π> = 0)

Figure 2.3. Antiferromagnetic superexchange (SE) interactions, **IVa** (dπ-π type), and **IVb** (dπ-π* type) between metal and 4-pyridyl moiety, respectively. **IVc** and **IVd** show the ferromagnetic SE interactions by orbital orthogonality. **IVc** is induced by the charge transfer (CT) from pyridyl moiety to carbene site, while **IVd** is induced by CT from methylene site to pyridyl moiety.
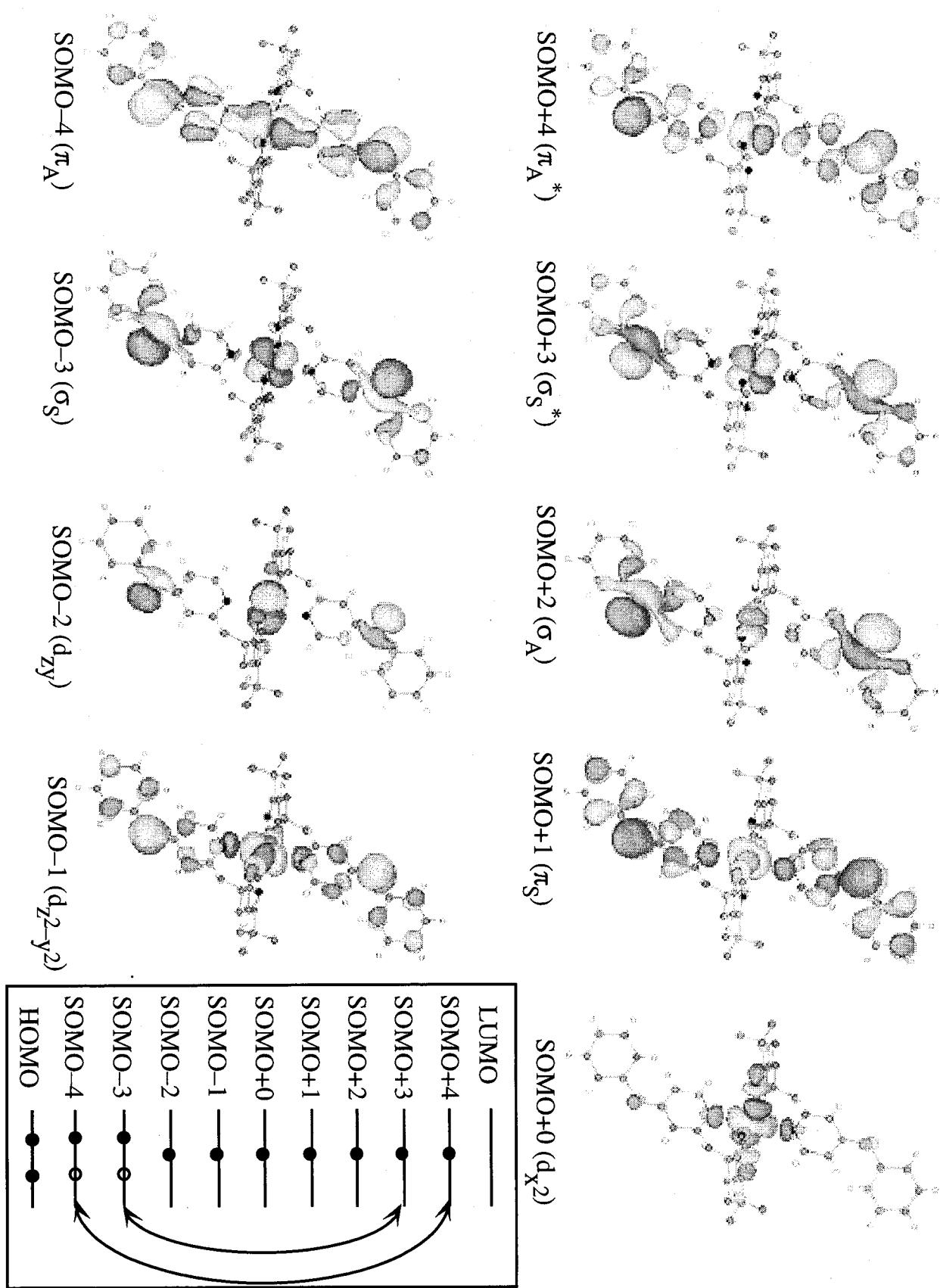
Figure 2.4.   Natural orbitals for the lowest spin (LS) state of Mn(II)(hfac)$_2${di(4-pyridyl)phenyl]carbene} **1a** by the UB3LYP calculation.

SOMO+2 (π^+_{right})

SOMO+1 (σ^+_{right})

SOMO+0 (σ_{center})

SOMO−2 (π_{left})

SOMO−1 (σ_{left})

SOMO+0 ———

SOMO−1 ——•—— SOMO+1

SOMO−2 ——•—— ——•—— SOMO+2
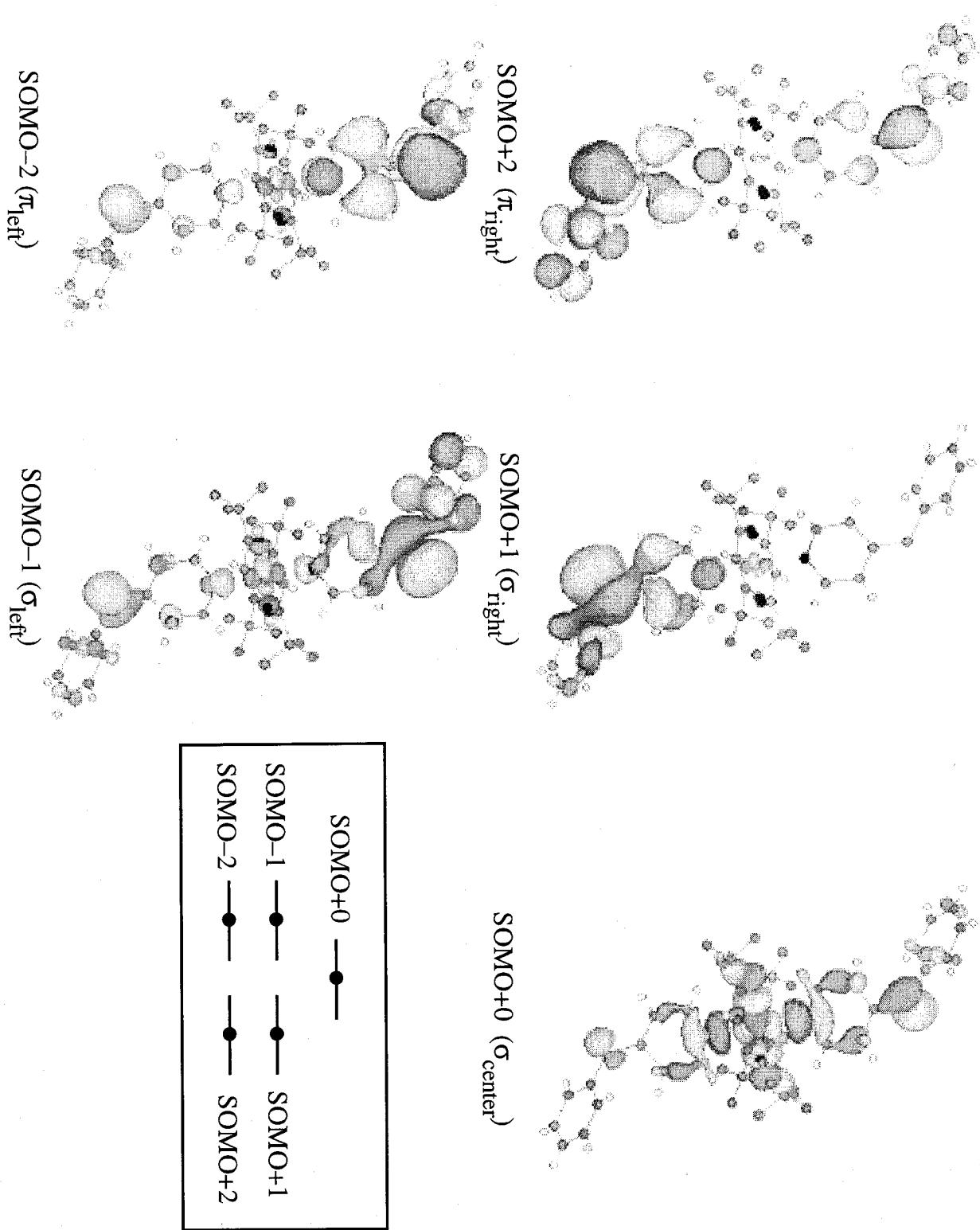
Figure 2.5.   Natural orbitals for the highest-spin (HS) state of Cu(II)(hfac)$_2${di(4-pyridyl)phenylcarbene} **2a** by the UB3LYP calculation.
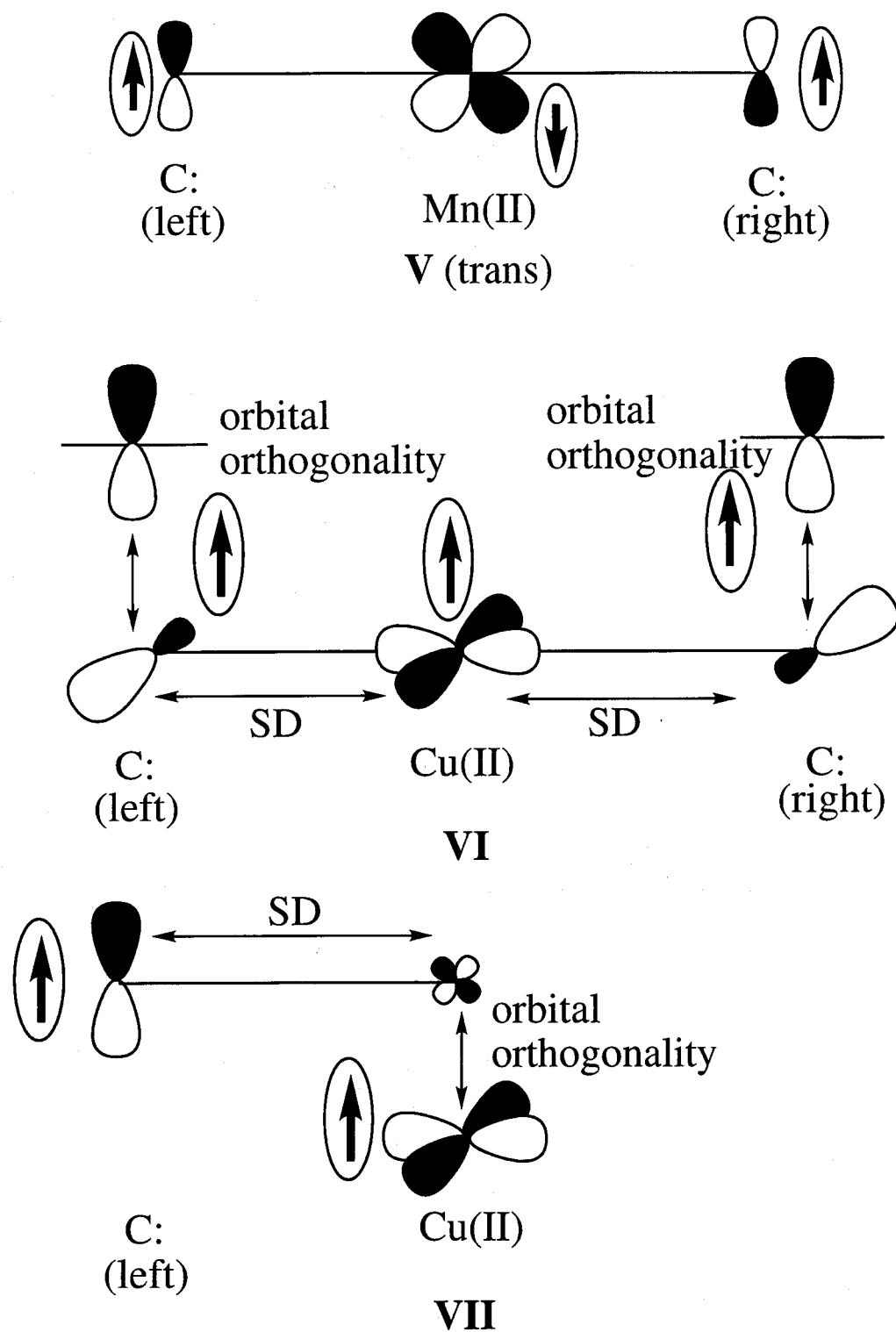
Figure 2.6. Orbital interaction schemes for π-type antiferromagnetic superexchange interaction **V** of Mn(II)(hfac)$_2$ {di(4-pyridyl)phenylcarbene} {**1a** (**3T**) and **3C**}, and σ-π type ferromagnetic superexchange interactions (**VI** and **VII**) for Cu(II)(hfac)$_2$ {di(4-pyridyl)carbene} (**2a**).
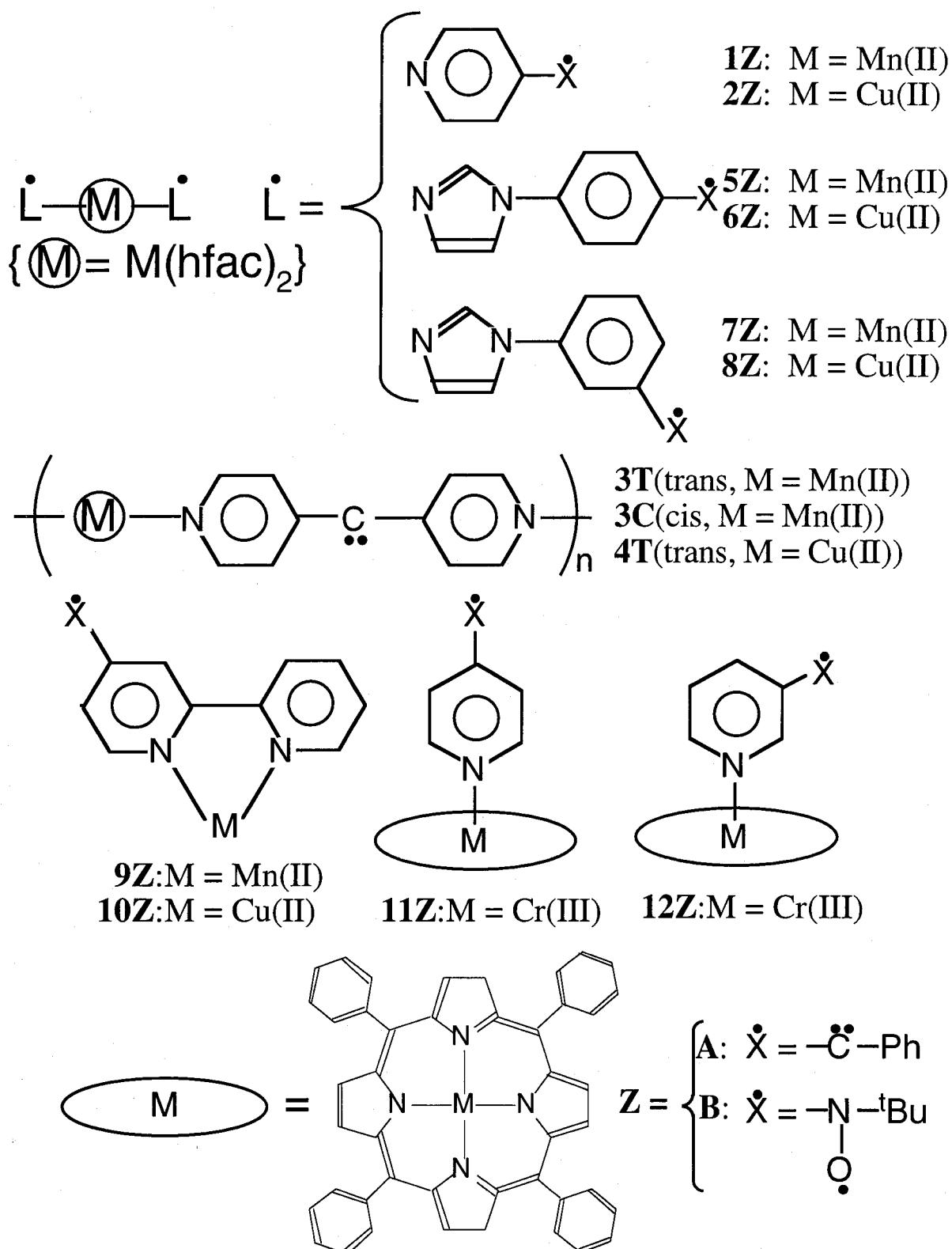
Figure 2.7.   The d-p conjugated magnetic systems (1–12) with *p*- or *m*-phenylene type bridges. M means transition metals such as Mn(II) and Cu(II). The observed J_{ab} values for these species are given in **Table 2.1**.

Part II

Chapter 3

The Effective Exchange Interaction of

d-π-d Conjugated Systems

Involving *m*-phenylene Type Bridge

3.1 Introduction

Molecular materials with strong magnetic properties have been extensively studied by both theoretical and experimental chemists [1–6]. The materials provide not only the deep insight into chemical bonding and the alignment of electronic spins, but also the possibilities of new functional materials such as ferro- or ferri-magnet, magnetic conductor, spin-mediated superconductor and photo-induced magnet.

It is well-known that oligo-carbenes and -radicals linked with *m*-phenylenes have highest-spin (HS) ground states [7–10, 17–19]. From a lot of theoretical and experimental studies, it is found that spin polarization (SP) and spin delocalization (SD) effects play important roles in the alignment of the spins on organic magnets [68, 71, 78]. The SP rule predicts that spins with opposite sign appear alternatively at each of the neighboring atom sites in magnetic molecules. On the other hands, the SD (superexchange(SE)) effect means that spins are delocalized due to charge transfer (CT). The SD effect is important for the magnetic interactions of radicals linked hetero atoms (O, N, S) and ion radicals.

However, it is not sufficiently clear whether an analogous rule holds for organometallic coordination compounds involving transition metals as spin sources. If the spin sources are changed from carbene to transition metal ions, we can utilize the variety of the d-d and d-p interactions, use transition metal ions as bridges of the magnetic compounds, and expect the large spin state. Experimental studies on these systems have been reported. Ishida, Nogami and their collaborators synthesized $(hfac)_2M(II)(DPPM)M(II)(hfac)_2$ (M = Mn(II) and Cu(II), hfac = hexafluoroacetylacetone, DPPM = 4,6-dipyridylpyrimidine) linked *m*-phenylene type bridge, pyrimidine, and measured their magnetic properties [79, 80]. Therefore, the effective exchange interaction (J_{ab}) between Mn(II) ions via pyrimidine for the Mn complex was found to be −0.14 cm^{-1}, showing an antiferromagnetic interaction. The J_{ab} value between Cu(II) ions via pyrimidine for the Cu complex also shows an antiferromagnetic interaction (−16.0 cm^{-1}). These complexes provide scientific interest for elucidation of the electronic and magnetic properties of the d-d conjugated systems. However, theoretical studies are rather limited at present.

Generally, we consider three problems for theoretical studies on effective exchange interaction of d-d conjugated systems. The first is design of building blocks. What kind of spin

sources should be chosen? What kind of coupler should be chosen? The second is about coordination effect of ligands. It is dispensable to consider the effect of ligands, because the charge transfer between transition metal ion and π-conjugated group can be controlled by coordination ligands. However, the system involving ligands is so large that the computational cost becomes very high. The third is about calculation methods. We must take account into electron correlation effect, when the magnetism of metal and metal complexes is investigated. Therefore, we should perform post Hartree-Fock (HF) calculation, such as many body perturbation theory and coupled cluster approximation, for metal complexes in order to elucidate the magnetic interaction of them. However the post-HF calculations take a great deal of computational cost.

In recent years, density functional theory (DFT) has been applied to large molecules to elucidate various properties such as binding energy and excitation energy [7–10]. DFT has been accepted as an alternative approach for the post Hartree-Fock methods to overcome the electron correlation problem.

In this chapter, the author paid attention to the magnetism of the metal-π conjugated complexes, involving pyrimidine as *m*-phenylene type unit. First, the author focused the naked d-π-d part, because these parts are important to examine the magnetic interaction of d-π-d systems. Next, the author can estimate the effect of ligand for those systems. Especially, the author have investigated the d-π-d magnetic interaction via pyrimidine Mn(II)$_2$-pyrimidine (**1**), Cu(II)$_2$-pyrimidine (**2**) and Mn(II)Cu(II)-pyrimidine (**3**) as shown in **Figure 3.1** by ab initio calculations. The results by DFT have been compared to those by UCCSD(T), which is the most reliable method in this work, and the experimental value. The NO analysis of the UHF and DFT solutions of **1–3** has been performed to elucidate relative contributions of SP and SD (or SE) interactions for determination of the sign of J_{ab} values. Implications of the calculated results have been discussed in relation to the molecular magnetism of Mn(II) and Cu(II) complexes from the viewpoint of charge and spin density distributions and natural orbitals. Finally, the author considered ligand effects for the elucidation of the magnetic interactions of d-π-d conjugated complexes. UBLYP and UB3LYP calculations have been performed for the Mn(II)$_2$-pyrimidine with ten hydrides complex (**4**) in order to examine the dependence of the J_{ab} on the coordination distance R of hydrides (ligands) as shown in **Figure 3.1**.

3.2 Calculation method

3.2.1 Configuration interaction model

For lucid explanation of the calculated results, the author considers the orbital symmetry rule [59] for the d-π-d conjugated systems.   Here, the author utilizes the intermolecular configuration interaction (CI) [59] picture for **1–3** in order to investigate the mechanism of the effective exchange interactions.   The M_2-pyrimidines can be divided into M(II) (M = Mn and Cu), pyrimidine or pyridine (pyd) and M(II) fragments as shown in **5** of **Figure 3.2**.   Judging from previous computations of transition metal-methylene complexes (M = CH_2) [59], the direct exchange interactions between M(II) and M(II) should be essentially zero because of relatively long intersite distance; R(M–M) > 5.0Å.   Since the nitrogen site of pyd group coordinates to the M(II) ion, the SD [70, 71] mechanism should be operative between the dσ half-occupied orbital of M(II) and N-lone pair as illustrated in **6** of **Figure 3.2**.   The through σ-bond interaction of the dσ spin via the SP of the σ-bond network of pyd group for **1–3** provides net antiferromagnetic exchange integrals with the dσ spin of M(II), as shown in **7a** of **Figure 3.2**.   On the other hand, the SP effect through π-bond network in **1–3** should also provide a ferromagnetic interaction as illustrated in **7b** of **Figure 3.2**.   Here, the author utilizes the spin vector model for pictorial understanding of the SP effect.

Secondary, the author must consider the CT interaction of Mn(II) with the π-orbital of pyrimidine group as shown in **8a** and **8b** of **Figure 3.2**.   The CT from the π-orbitals to the d-orbital of Mn(II) is conceivable, since the d-π orbital overlap integral is not zero (<d|π> = 0) as shown in **8a**.   The J_{ab} shows antiferromagnetic, because the exchange interaction between the spins of π-orbital and d-orbital is expressed due to the CT, as shown in **8b**.   This is an origin of the antiferromagnetic SE interaction.   Therefore, the sign of J_{ab} should be determined by relative contribution of the SP and SE (SD) effects; $J_{ab} > 0$ (SP > SE) and $J_{ab} < 0$ (SP < SE).   Thus the orbital symmetry rules are useful for qualitative explanations of the experimental tendency.   But quantitative calculations of the J_{ab} values are difficult on the basis of the CT models because of the nonorthogonality problem of the magnetic fragment orbitals [59].

3.2.2 Computational geometries

The geometrical parameters of **1–3** were taken from the literature [59] as shown in **Figure 3.1** for a qualitative purpose. The M–N distance was assumed to be 2.0 Å. The C–C and C–N distance were 1.40 Å, while C–H distance was 1.08 Å as standard geometrical parameters. All the bond angles were assumed to be 120.0°. The UHF, UMP4, UCCSD(T), and DFT (UBLYP, UB3LYP and UB2LYP) for **1–3** with the above assumed geometry were performed by using the Tatewaki-Huzinaga [81] MINI and their MIDI plus Hay's [64] diffuse basis sets and Wachters basis set [63] for Mn(II), and 4-31G and/or 6-31G* basis sets for C, N, and H by Pople et al. [65, 66]. **Table 3.1** [63–66, 81] lists the four combinations **I–IV** of the basis sets employed for calculations.

In order to investigate the dependence of the J_{ab} values for **4** on the coordination distance R, UBLYP/**IV** and UB3LYP/**IV** were performed. The geometrical parameters of **4** were the same as that of **1** for Mn(II)$_2$-pyrimidine part. Five hydrides were coordinated to each Mn(II) ion to form octahedral structure with N-atom in pyrimidine group as shown in **Figure 3.1**. The distance Mn-H$^-$ was varied from 1.7 Å to 2.5 Å.

3.3 Magnetic Interaction for 1–3

3.3.1 Effective exchange interaction (J_{ab})

In order to estimate the magnitude of the magnetic interaction for **1–3**, we have evaluated J_{ab} values for **1–3** by ab initio calculations. **Table 3.2** summarizes the J_{ab} of **1–3** by approximately projected (AP) post Hartree-Fock and DFT methods (eq. (12c)).

In the case of **1**, the J_{ab} value by UHF/**IV** shows ferromagnetic interaction between the Mn(II) ions via pyrimidine. This is inconsistent with the experiment (–0.14 cm^{-1}) [79]. This implies that UHF overestimates SP effects. On the other hand, the J_{ab} values estimated by UBLYP, UMP4 and UCCSD(T) show antiferromagnetic interactions, even though the *m*-phenylene type bridge is employed. These methods can reproduce the experimental value qualitatively. Especially, UCCSD(T) and UBLYP estimate J_{ab} values close to the experiment. The sign of J_{ab} value is negative for Mn(II)$_2$-pyrimidine due to the proper inclusion of an antiferromagnetic SE effect. UB2LYP and UB3LYP evaluate positive J_{ab} values by basis **I**, **II**, and **IV**, because of the

inclusion of ferromagnetic UHF character.

From the J_{ab} value for **2**, UB2LYP, UMP4 and UCCSD(T) provide negative J_{ab} values. However, in comparison with UCCSD(T) and the experiment (-16.0cm^{-1}) [81], UMP4 overestimate the magnitude of J_{ab} values.   For evaluating the J_{ab} values of **2**, it is necessary to calculate at UCCSD(T) level in the post-HF calculations.   While, UB2LYP can reproduce the J_{ab} values for **2** qualitatively.   The author has performed UB3LYP and UBLYP calculations for **2**, but no reasonable results were obtained because of strong charge transfer from pyrimidine to Cu(II). These overestimations might be removed if (hfac)$_2$ ligands are added to Cu(II) ion, since (hfac)$_2$ decrease the electron affinity of Cu(II).

From the results for **3**, the J_{ab} values by UHF, DFT and UCCSD(T)/**III** show antiferromagnetic interactions.   UHF and DFT provide reasonable J_{ab} values qualitatively.   While, UMP4 and UCCSD(T)/**I** provide positive J_{ab} values, showing ferromagnetic interaction.   Therefore, in order to estimate the reasonable J_{ab} values for **3**, the author must perform the UCCSD(T) calculations at the level of triple zeta basis sets (**III**), if post-HF calculation are carried out.

3.3.2 Charge density populations

The author has investigated the population of charge densities of **1–3** in order to elucidate the magnitude of the J_{ab} values.   **Table 3.3** lists the population of the charge densities estimated by UHF/**IV**, UB2LYP/**IV**, UB3LYP/**IV** and UBLYP/**IV**.

In the case of **1**, the net charge densities on the Mn(II) ions are 1.895 and 1.703, by UHF and UBLYP, respectively.   UBLYP estimates the more proper charge transfer from pyrimidine group to Mn(II) ion than UHF.   Judging from J_{ab} values, UBLYP estimates the SE interaction more appropriately than UHF.

The net charge densities on the Cu(II) for **2** ions are 1.839 and 1.660, respectively.   The J_{ab} values by UB2LYP are reasonable, since UB2LYP calculation provides appropriate CT (0.330). Compared with **1**, the CT of Cu(II) ion is much larger than that of Mn(II) ion.

From the results for **3** in **Table 3.3**, the net charge densities on the Mn(II) (Cu(II)) are 1.897 (1.835), 1.840 (1.635), 1.796 (1.463) and 1.747 (1.342) by UHF, UB2LYP, UB3LYP and UBLYP, respectively.   These results indicate that the CT from pyrimidine to both Mn(II) and Cu(II) are increased in the order: UHF < UB2LYP < UB3LYP < UBLYP, and the CT to Cu(II) is

larger than that to Mn(II).

3.3.3 Spin density populations

The author has investigated the population of spin densities of **1–3** in order to elucidate the sign the J_{ab} values. **Table 3.4** lists the population of the spin densities estimated by UHF/IV, UB2LYP/IV, UB3LYP/IV and UBLYP/IV.

The magnitude of the spin densities on C- and N-atoms in the pyrimidine ring for **1–3** are 0.3 to 0.5 by UHF, and their signs change alternatively to show the characteristic of the spin density wave (SDW). Therefore, this is in conformity with the SP effect. However, judging from the magnitude of them, UHF overestimates the SP effect of the pyrimidine ring.

The population of spin densities calculated by the UBLYP does not exhibit the SDW-type spin alternation but shows that the sign of the spin density on Mn(II) ion is the same as that on N-atom in the pyrimidine ring, namely, SD pattern.

In both UHF and DFT, the sign of spin on Cu(II) is the same as that of neighbor N-atom in pyrimidine. These results are because of the SD effect and the orthogonality between dσ orbital of Cu(II) and π orbital of pyrimidine. While, the sign of spin on Mn(II) is the same as that of neighboring N-atom in the case of UBLYP, those on Mn(II) and neighbor N-atom are alternative in UHF, UB2LYP and UB3LYP. These results depend on the balance of SP and SD effect (SP >> SD by UHF, SP > SD by UB2LYP and UB3LYP and SD > SP by UBLYP).

3.3.4 Natural orbitals and occupation numbers

We have examined the singly occupied natural orbitals (SONO) of **1–3** by UHF and UBLYP calculations, respectively, in order to clarify the mechanism of the magnetic interaction of **1–3**.

First, **Figure 3.3** shows the shape of SONO for **1–3**. The localized natural orbitals are found on the M(II) ions at UHF level, indicating that UHF method underestimates SE interaction. Judging from this result and the population of spin density, J_{ab} becomes ferromagnetic due to the overestimates of the SP effect by the UHF theoretical treatment. On the other hand, from **Figure 3.3 B**, we can observe the NOs delocalized on the whole molecule at UBLYP level. UBLYP provides the antiferromagnetic SE interaction between M(II) ions via pyrimidine ring.

Table 3.5 lists the occupation numbers of HOMO, SONO and LUMO obtained for the lowest spin states of 1–3 by UHF and DFT calculations. The occupation numbers of SONO–5 (SONO–4) for 1 are 1.006 (1.005), 1.013 (1.010), 1.027 (1.020) and 1.057 (1.042) by UHF, UB2LYP, UB3LYP and UBLYP, respectively. SONO–5 and SONO+5 show σ-type orbital interaction, while SONO–4 and SONO+4 show π-type orbital interaction. From their occupation numbers, σ-type orbital interaction influences on the magnetic interactions of 1 as well as π-type orbital interaction. Therefore, the proper estimate of both σ- and π-type orbital interactions by UB3LYP and UBLYP causes the reasonable antiferromagnetic SE interaction.

The occupation numbers of SONO–1 for 2 are 1.0085, and 1.0664 by UHF and UB2LYP, respectively. SONO–1 and SONO+1 are σ-type orbitals. These orbitals show the σ-type antiferromagnetic SE interaction, and cause the negative J_{ab} values for 2.

The occupation numbers of SONO–3 for 3 are 1.008, 1.042, 1.142 and 1.211 by UHF, UB2LYP, UB3LYP and UBLYP, respectively. SONO–3 and SONO+3 show the σ-type orbital interaction. These results indicate that SONO+3 by UB3LYP and UBLYP interacts with SONO–3 on pyrimidine ring strongly. Therefore, both UB3LYP and UBLYP calculations overestimate antiferromagnetic SE interaction because of strong σ-type orbital interaction.

Finally, the occupation numbers of HOMO are about 1.99 by UHF, while these are about 2.00 by UB2LYP, UB3LYP and UBLYP. These results show that SP effect does not play predominant role in J_{ab} values. Therefore, SE interaction is more important to evaluate the effective exchange interaction than SP effect.

3.4 Ligand Effects of Mn(II)$_2$-pyrimidine Complex 4

The author has investigated ligand effects for the elucidation of the magnetic interactions of d-π-d conjugated complexes. **Figure 3.4** illustrates the dependence of the J_{ab} values by using UBLYP/IV and UB3LYP/IV on the distance between Mn(II) ion and hydride. It is found that the J_{ab} values are decreasing in both UBLYP and UB3LYP, when the hydrides are close to the Mn(II) ion. The author has also investigated the SONO and their occupation numbers of 4 at R = 2.0 Å (**Figure 3.5 A**) and 2.4 Å (**Figure 3.5 B**) to elucidate the dependence of J_{ab} values on the distance R.

The occupation numbers range from 0.22 to 1.78 at $R = 2.0$ Å, while they range from 0.87 to 1.13 at $R = 2.4$ Å. When hydrides are close to Mn(II), the range of the occupation number is expanding. This implies that the energy difference between SONO is increasing, because the s orbital of the hydride interacts with the d-orbital of Mn(II) ion. Therefore, the J_{ab} values are decreasing in both UBLYP and UB3LYP level because of the stabilization of LS state. Thus, when ligands are coordinated to Mn(II) ion in **4**, J_{ab} values are decreasing. Judging from above results, we can expect that the negative J_{ab} value is due to not only SE interaction but also ligand effect.

3.5 Discussion and Concluding Remarks

3.5.1 Ab initio computations of J_{ab}

Magnetic interactions of metal-π conjugated complexes involving *m*-phenylene type bridges have been investigated by using DFT (UBLYP, UB2LYP and UB3LYP) and post-HF (UMP4 and UCCSD(T)) calculations. The author especially has focused the effective exchange integrals, the population of charge and spin density, the shape of natural orbitals and their occupation numbers in order to elucidate the magnetic interaction of these complexes. The author has concluded as follows; (i) the J_{ab} values for **1** are antiferromagnetic by UBLYP and UCCSD(T) calculations due to the proper inclusion of antiferromagnetic SE effects; (ii) the magnetic interaction for **2** are antiferromagnetic because of SD effect, the orthogonality between dσ orbital of Cu(II) and π orbital of pyrimidine ring and σ-path SE interaction; (iii) the shape of SONO and their occupation numbers show the strong σ-type orbital interaction of **3**, indicating that UB3LYP and UBLYP calculations for **3** overestimate antiferromagnetic interaction; (iv) the CT of Cu(II) is much larger than that of Mn(II); (v) for evaluating the J_{ab} values for d-π-d conjugated systems as well as p-π-p conjugated systems [7–10], it is necessary to calculate at UCCSD(T) level in post-HF methods; (vi) UB2LYP calculation can reproduce the J_{ab} values for d-π-d conjugated systems.

3.5.2 Spin alignment rule for the magnetic couplings of d-π-d conjugated system via pyrimidine coupler

Here, the selection rule for the magnetic couplings of the d-π-d conjugated systems has

been proposed on the basis of these through-bond interactions such as SE and SP effects in order to predict the sign of J_{ab} values between transition metal ions, as shown in **Table 3.6**.   In this chapter, the calculated results showed that the dπ-π-dπ and dσ-σ-dσ SE interactions in d-π-d systems are more contributable to the coupling constants (J_{ab}) than their SP effects, in contrast to predominant role of the SP effect in p-π-p systems [7–10].   On the other hand, dπ-π-pπ conjugated systems show an intermediate character between d-π-d and p-π-p ones as described in the previous chapter. It is found from **Table 3.6** that SE interaction and SP effect are competitive for M_2-pyrimidine systems.   Therefore, the subtle balance between σ- and π- type SP effects and SE interaction is important for the magnetic couplings of these systems.

The author has compared the spin alignment rule to the calculated and experimental values. **Table 3.7** lists predicted magnetic interaction contributed by SP effect and SE interaction and calculated and experimental magnetic couplings of several M_2-pyrimidine complexes.   In the octahedral ligand field (**1, 2, 5–7**) [79, 82–84], the couplings are antiferromagnetic because of the larger contribution of SE interaction than that of the SP effects.   On the other hand, when the coordination ligands are distorted such as **6**, dπ-π-pσ SE interaction probably contribute the ferromagnetic magnetic couplings.   In addition, the insertion of O atom between transition metal ion and pyrimidine coupler strengthens the SP effects, leading to the ferromagnetic interaction of **7**. In order to predict the coupling constants considering the ligand coordination effects, the author should examine the coordination ligand effects.   Investigation of these results by ab initio calculation is under way.

3.5.3 Molecular design of magnetic polymers and lattices

In this chapter, Mn(II) and Cu(II) have been utilized as spin sources.   From above results, the magnetic interaction for d-π-d conjugated systems shows antiferromagnetic, since SE interaction is more effective to estimate the J_{ab} value for d-π-d conjugated systems than SP effect, which plays a predominant role in p-π-p conjugated systems.   While, the magnetic interaction for d-π-p conjugated systems depends on the balance between SP and SD (SE) effect.   When radical spins are introduced to the *meta* position of spin sites in the d-π-d conjugated systems, we expect that the exchange interaction for the d-π-d conjugated systems shows ferromagnetic, because radical spins strengthen SP effect of the d-π-d conjugated systems.   Using this idea, we can design

the lattice-type (**9**) and dendritic (**10**) ferromagnetic molecule, which provide the possibilities of spin dendrimer, as shown in **Figure 3.6**. Thus, these insight obtained in this work can lead us to be able to design new molecule-based ferromagnets which consists of d-π-d conjugated systems.

Table 3.1.   Basis sets employed for present calculations

Type	Metal	C, H, N
I	5333/533/5	4-31G
II	62111111/3312/32	6-31G*
III	533(21)/53(21)/41 + Hay's d diffuse function	6-31G*
IV	62111111/3312/32 + Hay's d diffuse function	6-31G*

Table 3.2. Effective exchange integrals $(J_{ab})^a$ calculated for **1–3** by UHF, UMP, UCC and DFT methods

Models	Methods	Basis sets[b]			
		I	**II**	**III**	**IV**
1	UHF	17.46	14.87	11.26	14.29
	UMP4	−139.9	−126.1	−128.4	−125.3
	UCCSD(T)	−15.56	−15.40	−19.72	−15.28
	UBLYP	−0.644	−0.134	−1.480	−0.780
	UB3LYP	0.211	0.311	−0.111	0.122
	UB2LYP	0.457	0.333	0.478	0.427
2	UHF	194.8	169.2	84.45	142.8
	UMP4	−2242	−1964	−1536	−1942
	UCCSD(T)	−240.0		−169.3	
	UB2LYP	−9.685	−84.67	−21.94	−56.92
3	UHF	−21.40	−20.23	−44.06	−31.84
	UMP4	74.08	90.43	157.2	108.2
	UCCSD(T)	7.847	11.45	−1.869	
	UBLYP	−38.07	−36.70	−56.38	−37.86
	UB3LYP	−13.98	−37.11	−50.06	−45.64
	UB2LYP	−2.462	−4.475	−13.15	−9.103

[a] J_{ab} are shown in cm^{-1}.   [b] Basis sets **I–IV** are given in **Table 3.1**.

Table 3.3. Charge densities of **1–3** by the UHF/IV[a], UB2LYP/IV[a] and UB3LYP/IV[a] and UBLYP/IV[a] methods

Model	Method	site number[b]							
		1	2	3	4	5	6	7	8
1	UHF	1.895	1.895	−0.243	0.236	0.236	−1.011	−1.011	0.354
	UB2LYP	1.828	1.828	−0.149	0.201	0.201	−0.874	−0.874	0.430
	UB3LYP	1.766	1.766	−0.091	0.180	0.180	−0.763	−0.763	0.373
	UBLYP	1.703	1.703	−0.040	0.175	0.175	−0.672	−0.672	0.353
2	UHF	1.839	1.839	−0.251	0.260	0.260	−1.017	−1.017	0.544
	UB2LYP	1.660	1.660	−0.149	0.221	0.221	−0.789	−0.789	0.465
3	UHF	1.897	1.835	−0.247	0.243	0.254	−1.014	−1.012	0.522
	UB2LYP	1.840	1.635	−0.148	0.208	0.214	−0.872	−0.782	0.448
	UB3LYP	1.796	1.463	−0.086	0.190	0.199	−0.759	−0.625	0.401
	UBLYP	1.747	1.342	−0.024	0.200	0.211	−0.672	−0.562	0.386

[a]Basis sets **I–IV** are given in **Table 3.1**.   [b]The site numbers are shown in **Figure 3.1**.

Table 3.4.   Spin densities of **1–3** by the UHF/$\mathbf{IV}^a$, UB2LYP/$\mathbf{IV}^a$ and UB3LYP/$\mathbf{IV}^a$ and UBLYP/$\mathbf{IV}^a$ methods

Model	Method	site number[b]							
		1	2	3	4	5	6	7	8
1	UHF	4.998	4.998	–0.507	0.378	0.378	–0.507	–0.507	0.548
	UB2LYP	4.962	4.962	–0.027	0.032	0.032	-0.011	-0.011	0.061
	UB3LYP	4.940	4.940	–0.011	0.028	0.028	0.010	0.010	0.045
	UBLYP	4.900	-4.900	0.000	0.003	-0.003	0.027	-0.027	0.000
2	UHF	0.948	0.948	0.447	-0.319	-0.319	0.362	0.362	-0.473
	UB2LYP	0.793	-0.793	0.000	-0.001	0.001	0.185	-0.185	0.000
3	UHF	4.996	-0.945	-0.478	0.355	0.341	-0.351	-0.385	0.512
	UB2LYP	4.960	-0.771	-0.043	0.032	0.029	-0.026	-0.229	0.058
	UB3LYP	4.928	-0.591	-0.051	0.023	0.004	-0.032	-0.299	0.045
	UBLYP	4.881	-0.481	-0.151	-0.042	-0.030	0.014	-0.143	-0.046

[a]Basis sets **I–IV** are given in **Table 3.1**.   [b]The site numbers are shown in **Figure 3.1**.

Table 3.5. Occupation numbers of the natural orbitals for the lowest-spin state of 1–3 by UHF, UB2LYP, UB3LYP and UBLYP calculations

Model	Methods	HOMO	SONO–5	SONO–4	SONO–3	SONO–2	SONO–1
1	UHF	1.998	1.006	1.005	1.004	1.004	1.003
	UB2LYP	1.998	1.013	1.010	1.001	1.001	1.000
	UB3LYP	1.997	1.027	1.020	1.002	1.002	1.000
	UBLYP	1.997	1.058	1.042	1.006	1.005	1.000
2	UHF	2.000					1.008
	UB2LYP	1.999					1.066
3	UHF	1.905			1.008	1.000	1.000
	UB2LYP	1.999			1.042	1.000	1.000
	UB3LYP	1.998			1.142	1.000	1.000
	UBLYP	1.998			1.211	1.000	1.000

Table 3.6.   Spin alignment rules for the magnetic couplings of M_2-pyrimidine   derived   for   SP

effects and SE interaction

path	$J_{ab}(SP)$	$J_{ab}(SE)$	$J_{ab}(total)$
dπ–π–dπ	> 0	< 0	< 0
dσ–σ–dσ	> 0	< 0	< 0
dπ–π–dσ	< 0	> 0	< 0 or > 0

Table 3.7. Predicted spin state and calculated and experimental magnetic couplings of several M_2-pyrimidine complexes in the octahedral ligand field

model	M	M'	SP	SE	J_{ab}(calc.)[a]	J_{ab}(exp.)[a]
1	$Mn^{2+}(d^5)$	$Mn^{2+}(d^5)$	F(π)	AF(π)	−19.72	−0.14[b]
2	$Cu^{2+}(d^9)$	$Cu^{2+}(d^9)$	F(σ)	AF(σ)	−169.3	−16.0[b]
5	$Ti^{3+}(d^1)$	$Ti^{3+}(d^1)$	F(σ)	AF(σ)		−1.4[c]
6	$V^{4+}(d^1)$	$V^{4+}(d^1)$	F(σ)	AF(σ)		>0[d]
7	$Fe^{3+}(d^5)$	$Fe^{3+}(d^5)$	F(π)	AF(π)		+0.65[e]

[a] J_{ab} are shown in cm^{-1}. [b]Ref. [79]. [c]Ref. [82]. [d]Ref. [83]. [e]Ref. [84].
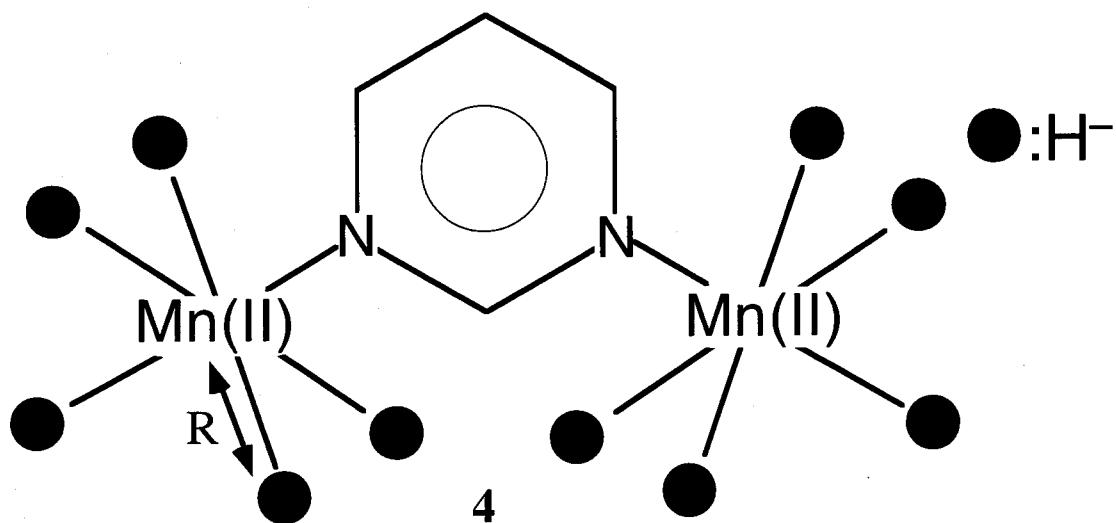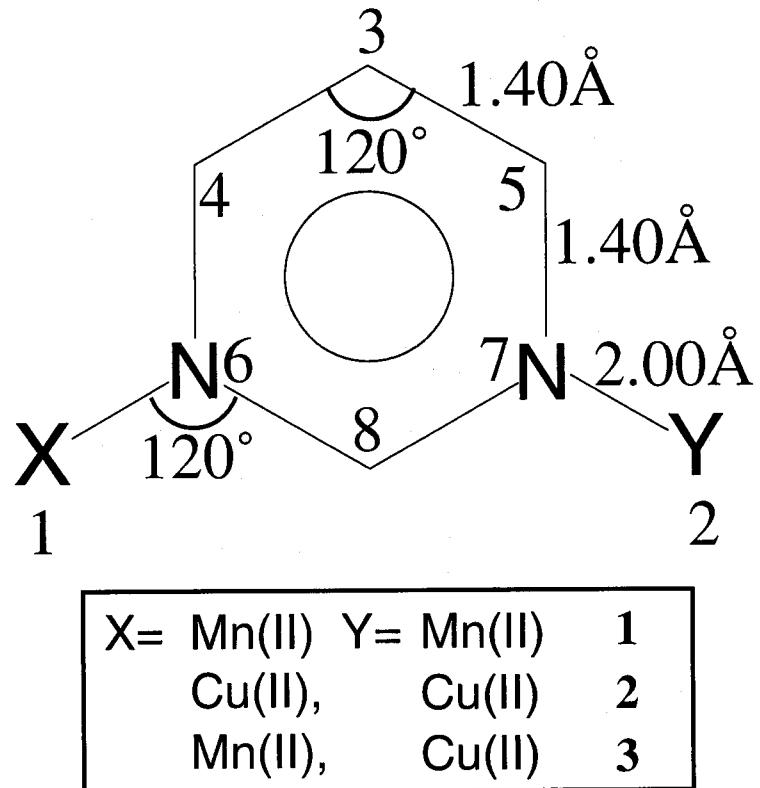
Figure 3.1.   The geometries and the site numbers of Mn(II)$_2$-pyrimidine, Cu(II)$_2$-pyrimidine, Mn(II)Cu(II)-pyrimidine are **1–3**, respectively.

4 is the Mn(II)$_2$-pyrimidine with ten hydrides complex to investigate the ligand effects.
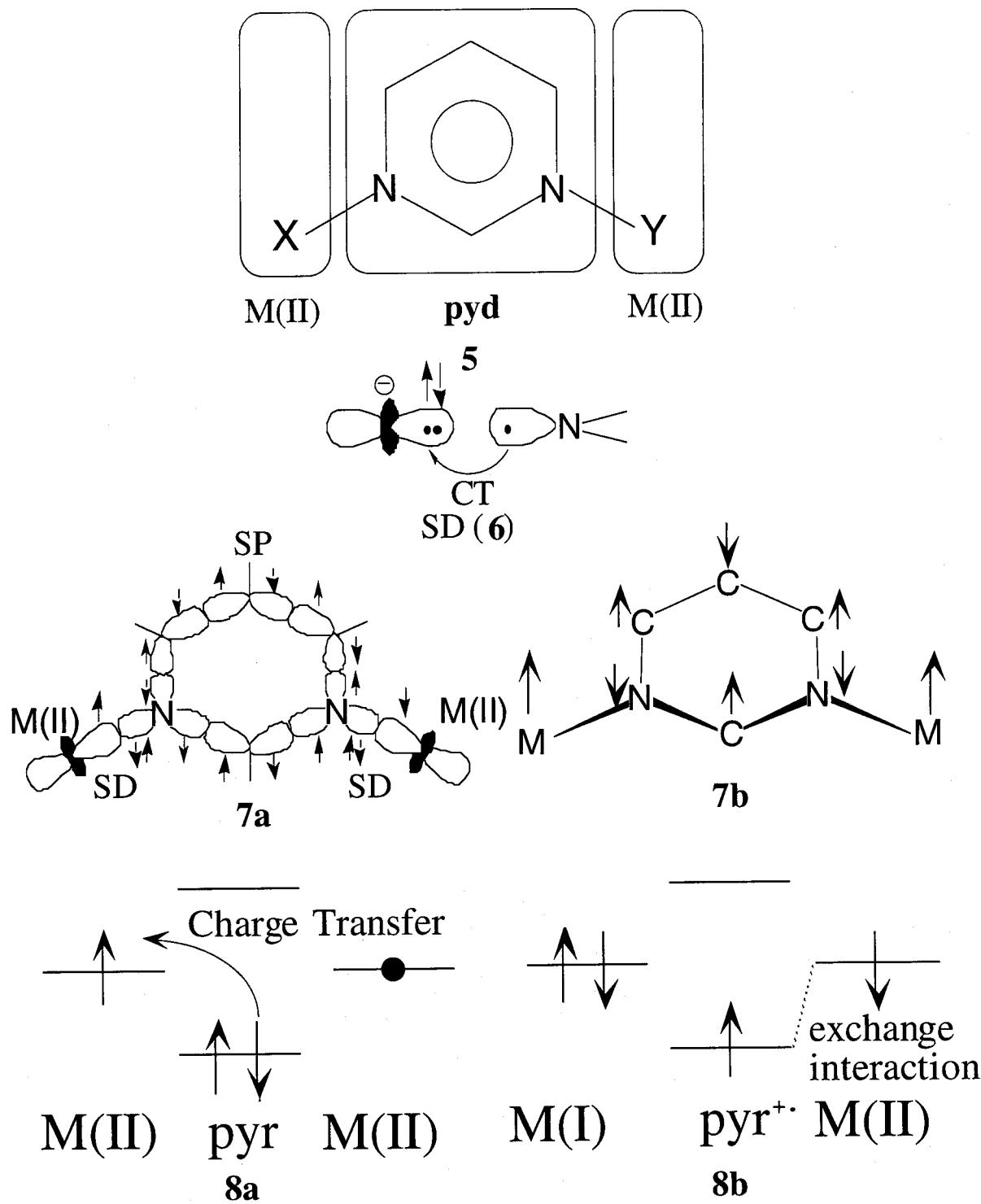
Figure 3.2.   **5** illustrates M(II), **pyd** and M(II) fragments. Spin delocalization (SD)

mechanism (**6**) between dσ-electron of transition metal ion (M) and lone

pair electrons of nitrogen atom in pyrimidine and pyridine ring. The spin

polarization (SP) mechanism through the pyrimidine via σ-networks is

explained by **7a**. The SP mechanism via π-network is illustrated by **7b**.

Antiferromagnetic superexchange interactions are shown between metal

and pyrimidine moiety in **8a** and **8b**.

1A

SOMO–5   SOMO–4   SOMO+4   SOMO+5

1B

SOMO–5   SOMO–4   SOMO+4   SOMO+5

2A

SOMO–1   SOMO+1

2B

SOMO–1   SOMO+1

3A

SOMO–3   SOMO+3

3B

SOMO–3   SOMO+3
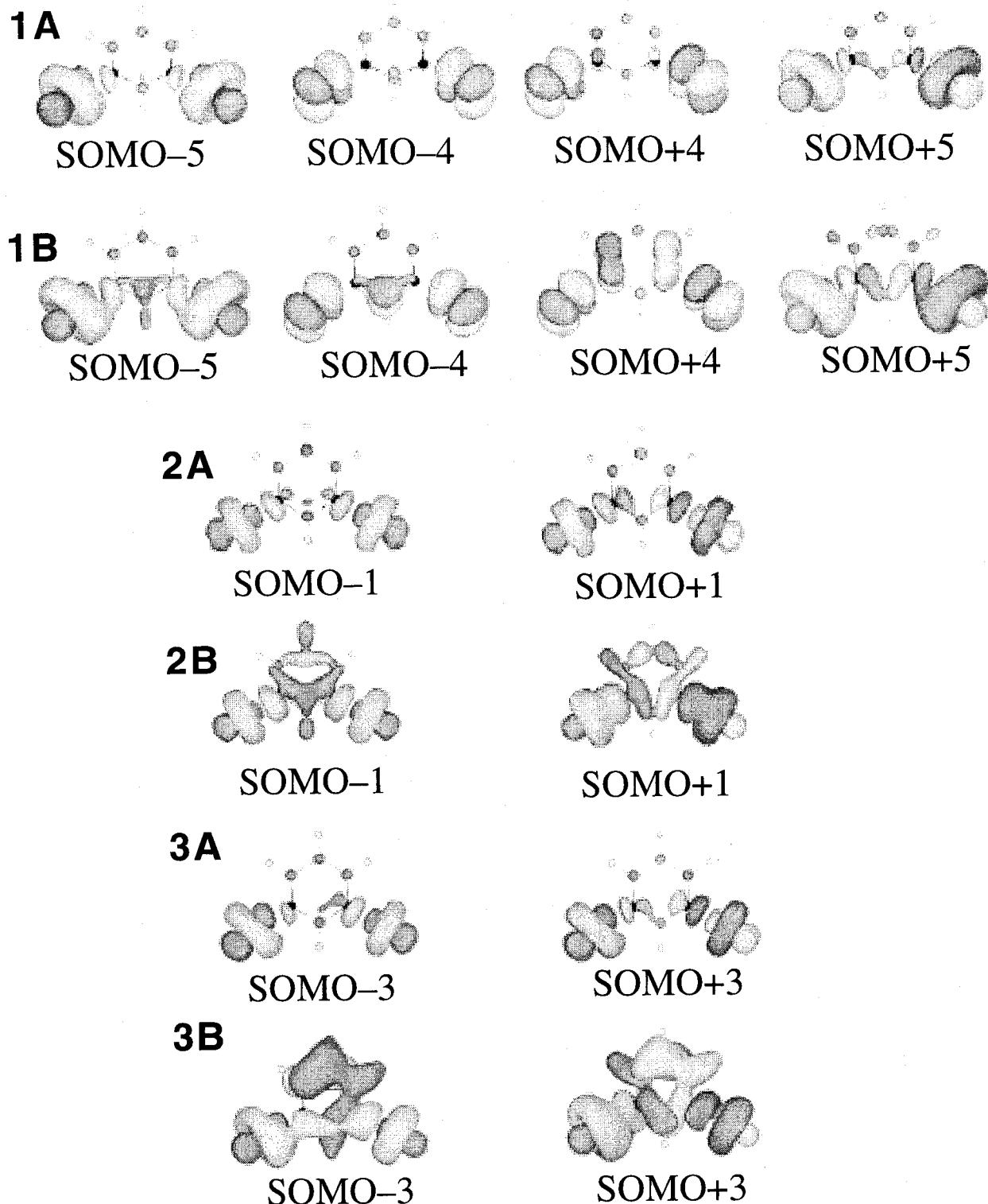
Figure 3.3.   Singly occupied natural orbitals (SONOs) of **1–3** by the UHF/**IV** (A)
and UBLYP/**IV** (B) methods at low spin state.
Basis set **IV** is shown in **Table 3.1**.
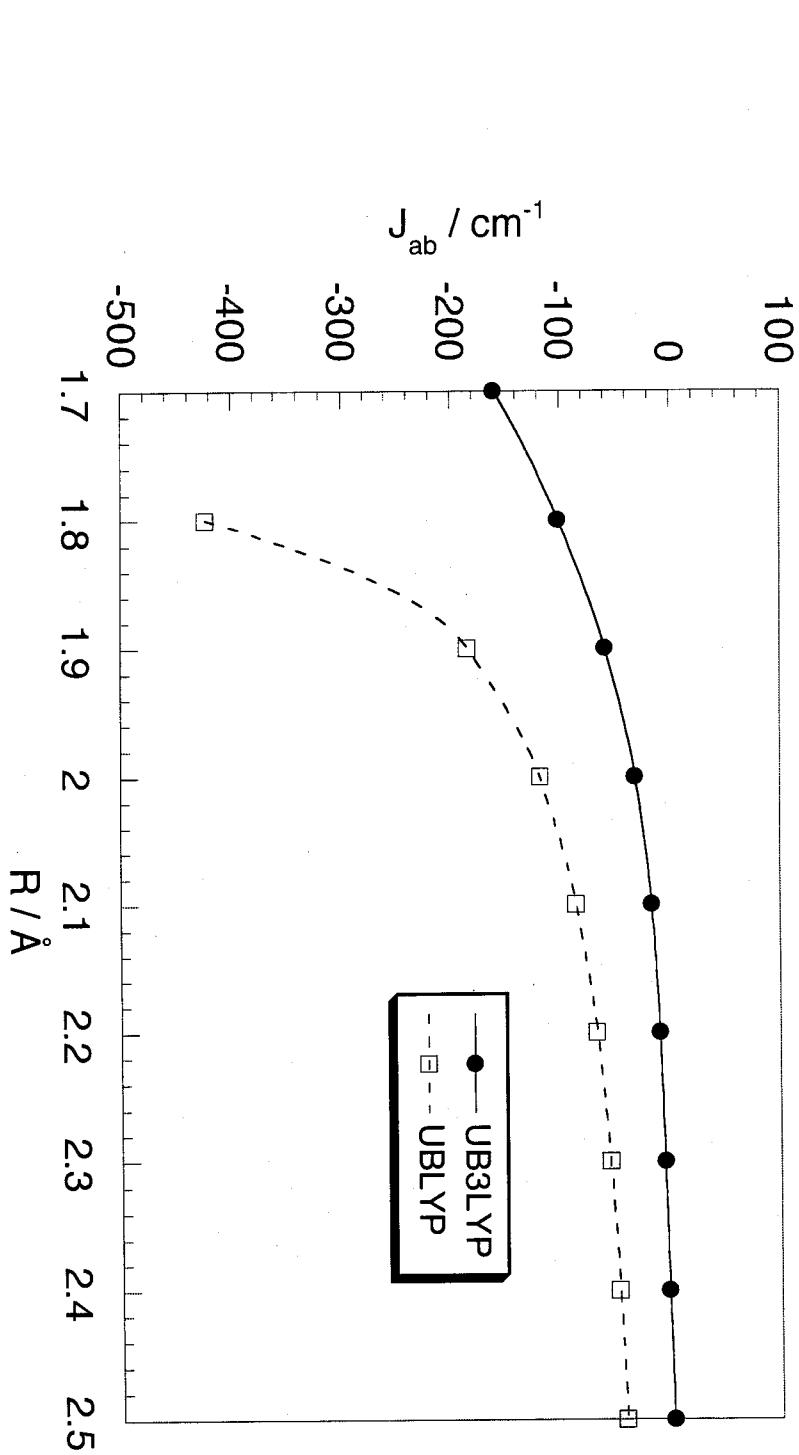
Figure 3.4   The dependence of J_{ab} values for **4** by UBLYP/IV and UB3LYP/IV on the coordination distance R between Mn(II) ion and hydride.

A $R = 2.0$ Å

1.77676

1.34049

1.01416

1.00686

1.00058

0.22324

0.65951

0.98584

0.99314

0.99942

B $R = 2.4$ Å

1.12782

1.06718

1.03686

1.00184

1.00066

0.87272

0.93282

0.96314

0.99816

0.99934
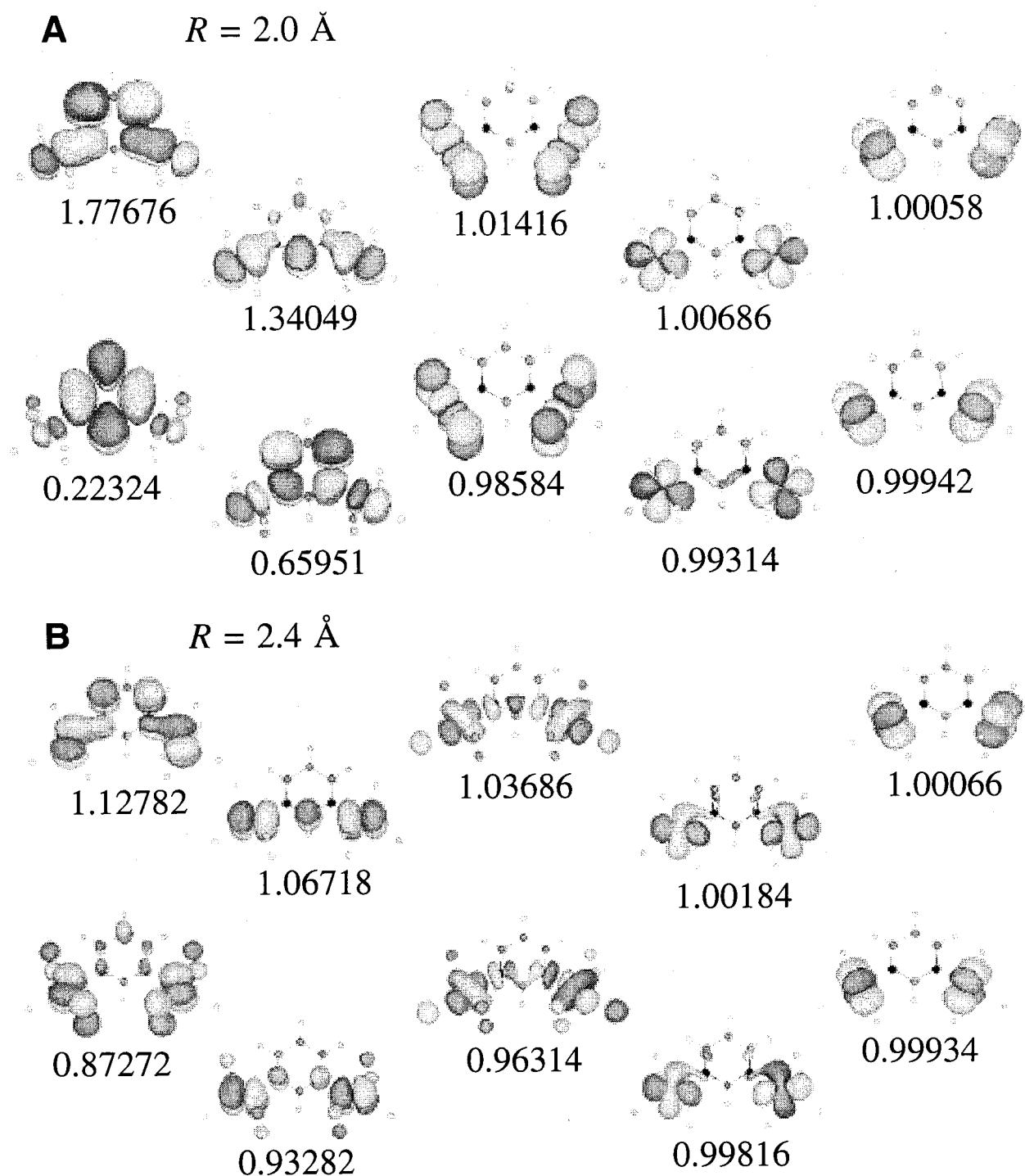
Figure 3.5.   SONOs and their occupation numbers of $Mn(II)_2$-pyrimidine with ten hydrides
complex **4** by the UB3LYP/**IV** methods at $R = 2.0$ Å (A) and 2.4 Å (B).
Basis set **IV** is shown in **Table 3.1**.

77

M=transition metal ion
R=organic radical

9

M=transition metal ion
R=organic radical

10
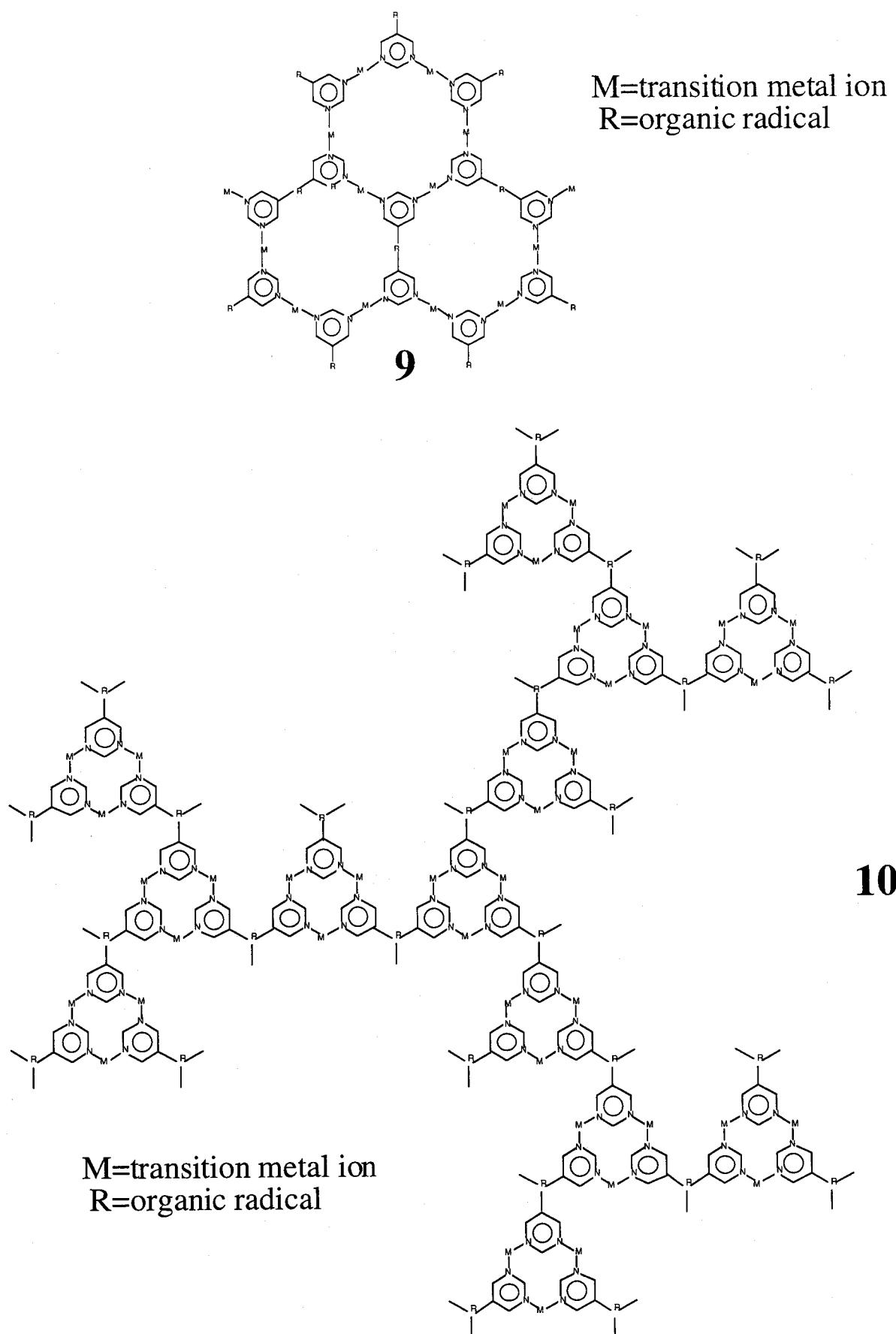
Figure 3.6.   Lattice-type (**9**) and dendritic (**10**) ferromagnetic polymer.

Part II

Chapter 4

Concluding Remarks of Part II

In this part, the author has investigated the electronic structures of d-π-p and d-π-d conjugated systems in order to elucidate the origin of the magnetic couplings and propose the spin alignment rule for these conjugated systems.

In chapter 2, bis(hexafluoroacetylacetonato(hfac))manganese(II) coordinated with di(4-pyridyl)phenylcarbene, $Mn(II)(hfac)_2\{di(4\text{-pyridyl})phenylcarbene\}$ (**A**) and its copper analog, $Cu(II)(hfac)_2\{di(4\text{-pyridyl})phenylcarbene\}$ (**B**) have attracted great interest from the viewpoint of photo-induced magnetism. The complexes **A** and **B** are regarded as the new d-π-p conjugated systems containing transition metal ion and carbene as spin sources. The magnetic measurements demonstrated antiferromagnetic and ferromagnetic effective exchange interactions for **A** and **B**, respectively. Here, we have performed UHF and UHF plus DFT hybrid calculations (UB3LYP) to elucidate the nature of the through-bond effective exchange interaction between Mn(II) (or Cu(II)) ion and triplet carbene sites in **A** (or **B**), and their model complexes. The natural orbital analysis of the UHF and UB3LYP solutions and CASCI calculations for the simplest models of **A** and **B** are performed to elucidate relative contributions of spin polarization (SP) and spin delocalization (SD) (or superexchange (SE)) interactions for determination of the sign of J_{ab} values. Mn(II) carbene complex **A** shows an antiferromagnetic interaction because of the π-type antiferromagnetic SE effect and the π-type SP effect, while the positive J_{ab} value for Cu(II) carbene complex **B** can be explained by the fact that ferromagnetic SE and SP interactions due to orbital orthogonality are more effective than the σ-type antiferromagnetic SE and SP interaction. Both the ligand coordination effects of 4-pyridylcarbene and hfac play crucial roles for determination of the J_{ab} values, but the ligand coordination effect of hfac is more important for the active control of charge or spin density distributions than that of 4-pyridylcarbene. The spin alignment mechanisms of **A** and **B** are indeed consistent with SE plus SP rule which is confirmed with the shape and symmetry of natural orbitals, together with charge and spin density distributions.

In this chapter 3, DFT and post HF calculations have been carried out for the metal-π conjugated complexes involving pyrimidine as *m*-phenylene type unit. Total energies for the LS and HS spin states are used for investigation of d-π-d magnetic interactions via pyrimidine of $Mn(II)_2$-pyrimidine (**C**), $Cu(II)_2$-pyrimidine (**D**) and Mn(II)Cu(II)-pyrimidine (**E**). The natural orbital analysis of the UHF and DFT solutions of these complexes has been performed to elucidate relative contributions of SP and SD (SE) interactions for determination of the sign of effective

exchange integrals. Implications of the calculated results have been discussed in relation to the molecular magnetism of Mn(II) and Cu(II) complexes from the viewpoint of charge and spin density distributions, shapes of the natural orbitals and their occupation numbers. The J_{ab} values of **C** are antiferromagnetic by UBLYP and UCCSD(T) calculations due to the proper inclusion of antiferromagnetic SE effects. The magnetic interaction of **D** is antiferromagnetic because of SD effect, the orthogonality between dσ orbital of Cu(II) and π orbital of pyrimidine ring and σ-path SE interaction. The shape of SONO and their occupation numbers show the strong σ-type orbital interaction of **E**. Therefore, UB3LYP and UBLYP calculations for **E** overestimate antiferromagnetic interaction. The CT of Cu(II) is much larger than that of Mn(II). For evaluating the J_{ab} values for d-π-d conjugated systems as well as p-π-p conjugated systems, it is necessary to calculate at UCCSD(T) level in post-HF methods. When hydrides are close to Mn(II), the range of the occupation number is expanding. This implies that the energy difference between SONO is increasing, because the s orbital of the hydride interacts with the d-orbital of Mn(II) ion. Therefore, the J_{ab} values are decreasing in both UBLYP and UB3LYP level because of the stabilization of low spin state. Thus, when ligands are coordinated to Mn(II) ion of **F**, J_{ab} values are decreasing. Judging from above results, we can expect that the negative J_{ab} value is due to not only SE interaction but also ligand effect.

References of Part II

(1) Miller, J. S.; Epstein, A. J. Angew. *Chem. Int. Ed. Engl.* **1994**, *33*, 385.

(2) Rajca, A. *Chem. Rev.* **1994**, *94*, 871.

(3) Kahn, O. ed. *NATO ASI Series C, Vol.484, Magnetism: A Supramolecular Function*; Kluwer Academic Publishers: Dordrecht, 1996.

(4) Itoh, K.; Kinoshita, M. eds. *Molecular Magnetism -new magnetic materials*; Kodansha-Godon and Breach, Tokyo, 2000.

(5) Gatteschi, D.; Kahn, O.; Miller, J. S.; Palacio, F. eds. *Magnetic Molecular Materials*; Kluwer Academic Publishers: Dordrecht, 1991.

(6) Conorado, E.; Delhais, P.; Gatteschi, D.; Miller, J. S. eds. *NATO ASI series E, Vol. 321, Molecular Magnetism: From Molecular Assemblies to the Devices*; Kluwer Academic Publishers: Dordrecht, 1996.

(7) Mitani, M.; Takano, Y.; Yoshioka Y.; Yamaguchi, K. *J. Chem. Phys.* **1999**, *111*, 1309.

(8) Mitani, M.; Mori, H.; Takano, Y.; Yamaki, D.; Yoshioka Y.; Yamaguchi, K. *J. Chem. Phys.* **2000**, *113*, 4035.

(9) Mitani, M.; Yamaki, D.; Yoshioka, Y.; Yamaguchi, K. *J. Chem. Phys.* **1999**, *111*, 2283.

(10) Mitani, M.; Yamaki, D.; Takano, Y.; Kitagawa, Y.; Yoshioka, Y.; Yamaguchi, K. *J. Chem. Phys.* **2000**, *113*, 10486.

(11) Yamaguchi, K. *Int. J. Quant. Chem.* **1990**, *31*, 167.

(12) Nagao, H.; Mitani, M.; Nishino, M.; Yoshioka, Y.; Yamaguchi, K. *Int. J. Quant. Chem.* **1997**, *65*, 947.

(13) Yamaguchi, K.; Kitagawa, Y.; Onishi, T.; Isobe, H.; Kawakami, T.; Nagao, H. *Coord. Chem. Rev.* **2001** in press.

(14) Gatteschi, D.; Yamaguchi, K. in ref. 1d, p561, 1996.

(15) Nishino, M.; Yamaguchi, K.; Miyashita, S. *Phys. Rev.* **1998**, *B58*, 9303.

(16) Nagao, H.; Nishino, M.; Shigeta, Y.; Yoshioka, Y.; Yamaguchi, K. *J. Chem. Phys.* **2000**, *113*, 11237.

(17) Itoh, K. *Chem. Phys. Lett.* **1967**, *1*, 235.

(18) Wasserman, E.; Murray, R. W.; Yager, W. A.; Trozzolo, A. M.; Smolinsky, G. *J. Am. Chem.*

Soc. **1967**, *89*, 5076.

(19) Iwamura, H. *Pure Appl. Chem.* **1993**, *65*, 57.

(20) Takui, T.; Kita, S.; Ichikawa, S.; Teki, Y.; Kinoshita, T.; Itoh, K. *Mol. Cryst. Liq. Cryst.* **1989**, *176*, 67.

(21) Yamanaka, S.; Kawakami, T.; Okumura, M.; Yamaguchi, K. *Chem. Phys. Lett.* **1995**, *233*, 257.

(22) Yamanaka, S.; Okumura, M.; Nagao, H.; Yamaguchi, K. *Chem. Phys. Lett.* **1995**, *233*, 88.

(23) Fujiwara, M.; Nishino, M.; Takamizawa, S.; Mori, W.; Yamaguchi, K. *Mol. Cryst. Liq. Cryst.* **1996**, *286*, 185.

(24) Takeda, K.; Konshi, K.; Tamura, M.; Kinoshita, M. *Phys. Rev. B*, **1996**, *53*, 3374.

(25) Mito, M.; Kawae, T.; Takumi, M.; Nagata, K.; Tamura, M.; Kinoshita, M.; Takeda, K. *Phys. Rev. B* **1997**, *56*, R14255.

(26) Sato, O.; Iyoda, I.; Fujishima, A.; Hashimoto, K. *Science*, **1996**, *271*, 49.

(27) Sato, O.; Iyoda, I.; Fujishima, A.; Hashimoto, K. *Science*, **1996**, *272*, 704.

(28) Ohkoshi, S.; Yorozu, S.; Sato, O.; Iyoda, T.; Fujishima, A.; Hashimoto, K. *Appl. Phys. Lett.* **1997**, *70*, 1040.

(29) Fujiwara, M.; Mori, W.; Yamaguhchi, K. *Mol. Cryst. Liq. Cryst.* **1995**, *274*, 175.

(30) Nishino, M.; Kubo, S.; Yoshioka, Y.; Nakamura, A.; Yamaguchi, K. *Mol. Cryst. Liq. Cryst.* **1997**, *305*, 109.

(31) Nishino, M.; Takeda, S.; Mori, W.; Nakamura, A.; Yamaguchi, K. *Synth. Metals* **1997**, *85*, 1763.

(32) Nishino, M.; Yoshioka, Y.; Yamaguchi, K. *Chem. Phys. Lett.* **1998**, *297*, 51.

(33) Okumura, M.; Kawakami, T.; Oda, A.; Yamaguchi, K.; Mito, M.; Takeda, K. *Mol. Cryst. Liq. Cryst.* **1999**, *335*, 623.

(34) Nishino, M.; Yamaguchi, K.; Miyashita, S. *Phys. Rev. B* **1998**, *58*, 9303.

(35) Stumpf, H. O.; Ouahab, L.; Pei, Y.; Grandjean, D.; Kahn, O. *Science* **1993**, *261*, 447.

(36) Iwamura, H.; Inoue, K.; Hayamizu, T. *Pure Appl. Chem.* **1996**, *68*, 243.

(37) Kitano, M.; Ishimaru, Y.; Inoue, K.; Koga, N.; Iwamura, H. *Inorg. Chem.* **1994**, *33*, 6012.

(38) Ishimaru, Y.; Kitano, M.; Kumada, H.; Koga, N.; Iwamura, H. *Inorg. Chem.* **1998**, *37*, 2273.

(39) Caneshi, A.; Gatteschi, D.; Sessoli, R.; Rey, P. *Acc. Chem. Res.* **1989**, *22*, 392.

(40) Rajca, A.; Rajca, S. *J. Am. Chem. Soc.*, **1996**, *118*, 8121.

(41) Rajca, A.; Lu, K.; Rajca, S. *J. Am. Chem. Soc.*, **1997**, *119*, 10335.

(42) Rajca, A.; Wongsriratankul, J.; Rajca, S.; Cerny, R., *Angew. Chem. Int. Ed. Engl.* **1998**, *37*, 1229.

(43) Kumada, H.; Sakane, A.; Koga N.; Iwamura, H. *J. Chem. Soc. Dalton Trans.* **2000**, 911.

(44) Yoshioka, N.; Pahti, P. M.; Kaneko, T.; Kuzumaki, Y.; Tsuchida, E.; Nishide, H., *J. Org. Chem.* **1994**, *59*, 4272.

(45) Nishide, H.; Kaneko, T.; Nii, T.; Katoh, K.; Tsuchida, E.; Yamaguchi, K. *J. Am. Chem. Soc.*, **1995**, *117*, 548.

(46) Kamachi, M.; Kajiwara, A.; Mori, W.; Yamaguchi, K. *Mol. Cryst. Liq. Cryst.* **1995**, *273*, 117.

(47) Parr R. G.; Young, W. *Density Functional Theory of Atoms and Molecules*; Oxford University Press: Oxford, 1989.

(48) Trickey, S. B.ed., *Adv. Quantum Chem., Vol.21, Density Functional Theory of Many-Fermion Systems*; Academic Press: San Diego, 1990.

(49) Labanowski, J. K.; Andzelm, J. W. eds. *Density Functional Methods in Chemistry*; Springer-Verlag: New York, 1991.

(50) Seminario, J. M.; Politzer, P. eds., *Theoretical and Computational Chemistry, Vol.2, Modern Density Functional Theory: A Tool for Chemistry*; Elsevier: Amsterdam, 1995.

(51) Seminario, J. M. ed., *Theoretical and Computational Chemistry, Vol.4, Recent Developments and Applications of Modern Density Functional Theory*; Elsevier: Amsterdam, 1996.

(52) Kawakami, T.; Yamanaka, S.; Takano, Y.; Yoshioka, Y.; Yamaguchi, K. *Bull. Chem. Soc. Jpn.* **1998**, *71*, 2097.

(53) Soda, T.; Kitagawa, Y.; Onishi, T.; Takano, Y.; Shigeta, Y.; Nagao, H.; Yoshioka, Y.; Yamaguchi, K. *Chem. Phys. Lett.* **2000**, *319*, 223.

(54) Koga, N.; Ishimaru, Y.; Iwamura, H. *Angew. Chem. Int. Ed. Engl.* **1996**, *35*, 175.

(55) Sano, Y.; Tanaka, M.; Koga, N.; Matsuda, K.; Iwamura, H.; Rabu, P.; Drillon, M. *J. Am. Chem. Soc.* **1997**, *119*, 8246.

(56) Karasawa, S.; Sano, Y.; Akita, T.; Koga, N.; Itoh, T.; Iwamura, H.; Rabu, R;. Drillon, M. *J. Am. Chem. Soc.* **1998**, *129*, 10080.

(57) Musin, R. N.; Morokuma, K. *Abstract of Papers of the 7th International Conference on Molecule-Based Magnets, San Antonio, TX, September 16–21, 2000.*

(58) Yamaguchi, K.; Yoshioka, Y.; Fueno, T. *Chem. Phys.* **1977**, *20*, 171.

(59) Kawakami, T.; Yamanaka, S.; Yamada, S.; Mori, W.; Yamaguchi, K. in: Turnbull, M. M.; Sugimoto, T.; Thompson, L. K. Eds. *Molecule-Based Magnetic Materials, Theory, Technique and Applications, ACS Symposium Series 644*, 1996, p30.

(60) Yamaguchi, K.; Takahara, Y.; Fueno, *T. Appl. Quant. Chem.*, 155, Smith, V. H. et al. Eds. Reidel, 1986.

(61) Yamaguchi, K.; Tsunekawa, T.; Toyoda, Y.; Fueno, T. *Chem. Phys. Lett.* **1988**, *143*, 371.

(62) Yamaguchi, K.; Fueno, T.; Ueyama, N.; Nakamura, A.; Ozaki, M. *Chem. Phys. Lett.* **1989**, *164*, 210.

(63) Wachters, A. J. H. *J. Chem. Phys.* **1970**, *52*, 1033.

(64) Hay, P. J. *J. Chem. Phys.* **1977**, *66*, 4377.

(65) Hariharan, P. C.;   Pople, J. A. *Theoret. Chim. Acta* **1973**, *28*, 213.

(66) Ditchfield, R.; Hehre, W. J.; Pople, J. A. *J. Chem. Phys.* **1971**, *54*, 724.

(67) Pople, J. A.; Gill, P. M. W.; Johnson, B. G. *Chem. Phys. Lett.* **1992**, *199*, 557.

(68) Yamaguchi, K.; Toyoda, Y.; Fueno, T. *Synthetic Metals* **1987**, *19*, 81.

(69) Yamaguchi, K.; Toyoda, Y.; Nakano, M.; Fueno, T. *Synth. Metals* **1987**, *19*, 87.

(70) Kiribayashi, S.; Kobayashi, T.; Nakano, M.; Yamaguchi, K., *Int. J. Quant. Chem.* **1999**, *75*, 637.

(71) Yamaguchi, K. in *Electronic and Optical Functional Polymers*, chapter 12; K. Yoshino ed. Koudansha Scientific, 1990: Tokyo (in Japanese).

(72) Nakano, M.; Fujita, H.; Takahata, M.; Yamaguchi, K. *J. Chem. Phys.* **2001**, *115*, 1052.

(73) Kotori, H.; Ido, T.; Isoda, Y.; Kuwata-Gonokami, M. *Phys. Rev. Lett.* **1999**, *82*, 1116.

(74) Nagao, H.; Nakano, M.; Ohta, K.; Shigeta, Y.; Kiribayashi, S.; Yoshioka, Y.; Yamaguchi, K. *Mol. Cryst. Liq. Cryst.* **2000**, *342*, 273.

(75) Yoshioka, Y.; Kubo, S.; Yamaguchi, K.; Saito, I. *Chem. Phys. Lett.* **1998**, *294*, 459.

(76) Siegbahn, P. E. M.; Blomberg, M. R. A. *Annu. Rev. Phys. Chem.* **1999**, *50*, 221.

(77) Siegbahn, P. E. M.; Blomberg, M. R. A. *Chem. Rev.* **2000**, *100*, 421.

(78) Yamaguchi, K.; Okumura, M.; Maki, J.; Noro, T. *Chem. Phys. Lett.* **1993**, *207*, 9.

(79) Ishida, T.; Mitsubori, S.-i.; Nogami, T.; Iwamura, H. *Mol. Cryst. Liq. Cryst.* **1993**, *233*, 345.

(80) Ishida, T.; Nogami, T.; *Recent. Res. Devel in Pure & Applied Chem.* **1997**, *1*, 1.

(81) Tatewaki, H.; Huzinaga, S. *J. Chem. Phys.* **1980**, *72*, 339.

(82) Francesconi, L. C.; Corbin, D. R.; Hendrickson, D. N.; Stucky, G. D. *Inorg. Chem.* **1979**, *18*, 3074.

(83) Mitsubori, S.-i.; Ishida, T.; Nogami, T.; Iwamura H.; Takeda, N.; Ishikawa M. *Chem. Lett.* **1994**, 685.

(84) Oshio, H.; Ichida, H. *J. Phys. Chem.* **1995**, *99*, 3294.

Part III

Chemical Bonding Character, Magnetic Coupling and Dioxygen Binding Process of Non-Heme Oxygen Transport Protein

Part III

Chapter 1

General Introduction of Part III

Dioxygen is one of the indispensable molecules for most life on earth [1]. For most of the enzymes, one of the reactants is dioxygen. The uncatalyzed reactions of O_2 with organic substrates are thermodynamically favorable but kinetically slow since they are spin forbidden and the one-electron reduction potential of O_2 is low. In nature, aerobic life forms actively transport O_2 from the atmosphere to the appropriate cellular apparatus where the oxidative power of the O–O linkage is utilized for biological oxidation such as respiration and detoxification. The first and seemingly simplest step in this process of respiration involves the reversible coordination of the O_2 molecule to the iron- or copper-containing active sites of the metalloproteins hemoglobin (Hb) [2], hemerythrin (Hr) [3] and hemocyanin (Hc) [4–6]. A lot of experimental and theoretical scientists have investigated the mechanism of reversible dioxygen binding [1–6]. Experimental studies such as crystallographic, spectroscopic and kinetic studies have greatly developed our understanding of the electronic structure of the oxygen transport proteins and the mechanism of dioxygen binding. However, the reversible dioxygen binding process has not been elucidated yet.

Recently, progress in the area of accurate quantum chemical treatments of systems containing transition metals has been much faster during the past few years than anyone could have expected [7, 8]. Only five years ago, the treatment of the severe dynamical and nondynamical correlation effects seemed almost impossibly difficult even for small transition-metal complexes, and today there are a number of studies using high-accuracy methods of enzyme complexes with models including up to 50 atoms and which contain several transition-metal atoms. There are two main reasons for the surprisingly fast development of accurate treatments of transition-metal systems. The first, and most important, reason is that density functional theory (DFT) has developed into a much more accurate tool than before. In particular, the introduction of terms depending on the gradient of the density to describe the exchange interaction has proven to substantially improve the accuracy. This improvement, together with the improvement obtained by introducing a few semiempirical parameters and a part of the Hartree–Fock (HF) exchange, has led to an accuracy that is not far away from that obtained by the most accurate ab initio methods at a small fraction of the cost. The second factor responsible for the recent development is simply the increased experience obtained from the large number of model studies of transition-metal complexes performed during the past decade. This experience has, for example, led to a good understanding of how ligands in detail affect chemical reactions and also of how they can be

modeled.

In this part, utilizing insights described above, the author have performed UHF, hybrid DFT and pure DFT calculations for the active sites of non-heme oxygen transport protein, Hc and Hr. In order to elucidate the ligand coordination effects for the magnetic interaction and the reversible dioxygen binding process and to make it clear how dioxygen is bound to the active sites in Hc and Hr, the calculated results have been discussed on the exchange effective integrals (J_{ab}), the shape of natural orbitals, potential energy surfaces and several chemical indices defined in chapter 2 of Part I.

Part III

Chapter 2

The Nature of the Copper–Oxygen Bonds in Hemocyanin by Hybrid DFT Calculation of Effective Exchange Integrals and Dioxygen Binding Energy via Ligand Coordination Effects

2.1 Introduction

Hc is an oxygen transport protein found in mollusks and arthropods [4–6] and it has been studied from experimental and theoretical aspects [9–38]. The former studies have provided many insights into the nature of Hc [9–25]. Hc changes from the deoxygenated form to the oxygenated one when dioxygen is bound to Hc. The oxidation state of copper ions in oxyhemocyanins **1** (oxyHc) is cupric, Cu(II), while that in deoxyhemocyanins **2** (deoxyHc) is cuprous, Cu(I). In X-ray crystal structures of subunit II of *Limulus poliphemus* hemocyanin determined by Magnus and Hazes [9, 10], the active core of oxyHc bound to dioxygen consists of $Cu(\mu-\eta^2:\eta^2O_2)Cu$ as shown in **Figure 2.1**. Each copper atom is tightly coordinated in a square planar geometry to both oxygen atoms and to the nitrogen atoms of the two closer histidine ligands. The third histidine ligand is placed axially. The distance between the two copper ions is 3.54 Å, and the oxygen atoms are 1.41 Å apart [9]. On the other hand, in deoxyHc each of the two Cu atoms is trigonally coordinated by three histidines with a Cu(I)–Cu(I) distance of 4.6 Å as illustrated in **Figure 2.1** [10]. In addition to structural data, many other experimental results, obtained using different spectroscopic methods [11–15] such as Raman, UV, EPR and EXAFS, are available for the dioxygen binding nature of oxyHc. OxyHc with dioxygen show a diamagnetic behavior because of a strong antiferromagnetic coupling. In the coupling constant $-2J$, a lower limit of 600 cm^{-1} has been determined by SQUID magnetic susceptibility measurements [16, 17].

Synthetic modeling approaches [18–25] have greatly developed our understanding of how O_2 interacts with the reduced binuclear copper site of Hc. Kitajima and collaborators synthesized $[Cu(HBpz_3)]_2(O_2)$ (HBpz$_3$ = hydrotris{3,5-diisopropyl-pyrazolyl}borate) [18, 19], which was first characterized a $Cu(\mu-\eta^2:\eta^2O_2)Cu$ structure for the active site of dioxygen binding oxyHc, before the X-ray crystal results were reported. Also, mechanistic investigations have been performed to elucidate O_2 binding by biomimetic model complexes of Hc proteins. Recently, Liang, Karlin and co-workers suggested to be a $Cu^I-Cu^{II}-O^{2-}$ species for $[Cu_2(N_n)(O_2)]^{2+}$ (N_n = –(CH$_2$)$_n$– (n = 3–5) linked bis[(2-(2-pyridyl)ethyl]amine, PY2) [20].

Several theoretical studies have been carried out for models of the copper-peroxide complexes [26–38]. These studies have given results in agreement with the experiment. Solomon

performed SCF-Xα-scattered wave calculations on a model compound formed by the $Cu(I)_2$-O_2 complex with four in-plane NH_3 ligands to emulate the histidine ligands [26–28]. Maddaluno carried out ab initio ROHF-GVB computations on various geometrical arrangements of the Cu(O–O)Cu complex without introducing any additional ligands to simulate the histidine molecules [29]. Eisenstein, Getlicherman, Maddaluno and their co-workers applied the extended Hückel theory to a model system with two copper cations ligated by six imidazole groups and bridged by a peroxide [30, 31]. Bernardi performed ab initio calculations on the active site of oxygenated hemocyanin using both density functional theory and CASSCF approach followed by a perturbation treatment up to second order (CASPT2) to evaluate the dynamic correlation contributions [32, 33]. Very recently, Metz and Solomon investigated the reaction coordinate of the reversible O_2 binding by UB3LYP calculations with Hc model, $(NH_3)_3Cu(O–O)Cu(NH_3)_3$ [38]. The calculated results showed following conclusions. The protein matrix which holds two copper(I) centers enables simultaneous 2-eletron transfer. The Cu–Cu distance can regulate the exothermic character of the O_2 binding, providing an explanation for the origin of O_2 cooperativity. The spin forbiddness of the reaction overcomes by delocalization of the exchange stabilization onto the two metal centers so that the energy difference between the triplet and the singlet states is small. However, their calculated $-2J_{ab}$ value was 7550 cm^{-1}, in disagreement with the experiment (> 600 cm^{-1}). Previous studies employed small models such as $(NH_3)_2Cu(O–O)Cu(NH_3)_2$, $(NH_3)_3Cu(O–O)Cu(NH_3)_3$ and naked Cu(O–O)Cu, showing limitations. Ab initio calculations for realistic models involving imidazole and histidine ligands are crucial.

First, the author has here examined the origin and the ligand coordination effect for magnetic interaction by UHF, hybrid density functional (HDFT) calculations such as spin polarized Becke's half and half LYP (UB2LYP) and UB3LYP, and pure DFT (UBLYP). The author has utilized NH_3 (**a**), methylimidazole (**b**) and histidine (**c**) groups as the ligands coordinated to the copper core, Cu(II)–Cu(II) (**1**) and Cu(I)–Cu(I) (**2**), as shown in **Figure 2.2**. Next, in order to elucidate dioxygen binding process and its ligand coordination effects, the author has also performed UB2LYP calculations for **1a_O2, 1b_O2, 2a_O2** and **2b_O2** using two parameters of O–O length, 1.2Å (**O2N**, N denotes neutral.) for molecular oxygen (O_2) and 1.4Å (**O2D**, D denotes dianion.) for peroxide (O_2^{2-}). Reversible dioxygen binding of Hc has been investigated in detail from the

viewpoint of the shape of potential energy surface, charge and spin density distribution.   We can depict the smooth variation of potential energy in the dioxygen binding process of **1z** and **2z** with an approximate spin (AP) projection scheme with eq. (14).   The calculated results indicated that the magnitude of J_{ab} values are sensitive to the computational scheme, showing an important role in the orbital overlap of magnetic orbitals and that the different ligand coordination between **1a** and **1b** (**c**), namely NH_3 and imidazole groups, influences the dioxygen binding process of the models of oxyHc due to the balance of repulsive interaction between **1z** (**z** = **a–c**) and dioxygen and symmetry-allowed orbital interaction between $d_{xy} \pm d_{xy}$ orbitals of **1z** and π^* orbitals of dioxygen.   Recently, several chemical indices have been proposed to elucidate the nature of chemical bonds in biological systems by the post HF and broken-symmetry (BS) density functional calculations.   Probably, transition metal–oxygen bonds are very interesting targets for the analyses since their valence states are labile.   Here, the effective bond-order, unpaired-electron density and information entropy were calculated in terms of occupation numbers of the natural orbitals of the UB2LYP solution in order to elucidate the nature of the Cu_2O_2 bonding in Hc.

2.2 Ab Initio Calculation

2.2.1. Orbital inter action

MO analysis is useful for the investigation of the magnetic coupling and electronic structure. On the basis of orbital symmetry and ligand field theory, the orbital interaction was considered between d-orbitals of the Cu–Cu active core in Hc and p-orbitals of dioxygen.   In dioxygen binding state, since each copper ion is ligated in a square planar geometry, an unpaired electron in the Cu(II) ion of Hc occupies the d_{xy} orbital, indicating that $d_{xy} \pm d_{xy}$ orbitals contributes the SOMO orbitals in the binding state.   The $d_{xy} \pm d_{xy}$ orbitals can interact with $\pi_\perp^*$, π^* and σ^* orbiltals of dioxygen, leading to the orbital diagram as shown in **Figure 2.3**.   As a consequence, SOMO–1 constructs of symmetrical $d_{xy}-d_{xy}$ and $\pi_\perp^*$ orbitals, and SOMO+1 is formed by the antibonding combination of $d_{xy}+d_{xy}$ and π^* orbitals.   Judging from these orbitals, the strong antiferromagnetic coupling for **1z_O2D** arises from σ- and π-path superexchange (SE) interactions.

2.2.2. Computational procedure

The author employed UB2LYP as the exchange-correlation functionals to investigate the magnetic interaction and to examine the dioxygen binding process of Hcs. Basis sets used in all the calculations were Tatewaki–Huzinaga MIDI (533(21)/53(21)/(41)) [39] plus Hay's d diffuse function (α = 0.1491) [40] for Cu(II) ions, Pople's 6-31G* [41] for C, O and N atoms and 6-31G [42] for H atoms.

The geometry parameters of **1_O2D** and **2** were taken from X-ray crystallographic studies [9, 10]. In the X-ray structure of **1_O2D**, the center of Cu–Cu axis are 0.4 Å apart from that of dioxygen as shown in **Figure 2.2**. In other words, the active core of **1_O2D** forms a butterfly structure. In order to elucidate the ligand coordination effects, we chose NH_3 (**a**), methylimidazole (**b**) and histidine (**c**) as the ligands coordinated to the Cu_2O_2 core of **1** and **2** as shown in **Figure 2.2**.

First, using eqs. (12a)–(12c), the author estimated the magnetic couplings of **1b** and **1z** with dioxygen (**O2D**) which are 1.4Å apart (**1z_O2D**) and determined the NOs and their occupation numbers with eq. (15). Next, the author calculated the total energies in HS and LS states with the change of the distance R between the centers of mass of dioxygen and the two Cu ions of **1z** and **2z** as shown in **Figure 2.2**. The distance between dioxygen, *r2*, were utilized two parameters: 1.2 Å for the oxygen molecule, O_2, (**O2N**) and 1.4 Å for peroxide, O_2^{2-} (**O2D**). The potential energy surfaces in dioxygen binding processes for **1z_O2X** and **2z_O2X** (**X** = D and N) before and after the AP correction are depicted with eq. (14). The author has also estimated the binding energy corresponding to

$$^1[LCu(I)-Cu(I)L]+^3O_2 -> {}^1[LCu(II)O_2Cu(II)L], \qquad (25)$$
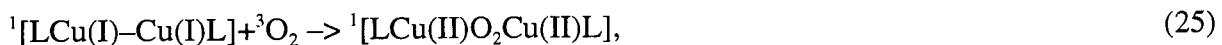
where L denotes ligands **a–c**. The author calculated the energies of $^1[LCu(I)-Cu(I)L]$ and $^3O_2$ (*r2* = 1.2 Å) separately and estimated the energy difference between $^1[LCu(II)O_2Cu(II)L]$ and $^1[LCu(I)-Cu(I)L]+^3O_2$. In order to elucidate the chemical bond character of **1z_O2**, several chemical indices were estimated using occupation numbers with eqs. (24a)–(24d).

Since these models were too large to optimize the geometries in our computer systems, other

parameters were fixed.   However, these model calculations should represent a significant advancement with respect to the ligand effects on the nature of the Cu_2O_2 bond and the reversible dioxygen binding process of Hc.

2.3 Magnetic Interaction of the Model Complex 1z_O2D

2.3.1 Effective exchange integrals and charge and spin density populations for 1z_O2D

To estimate the magnitude of the magnetic interaction for **1z_O2** and **1z**, the author has calculated the J_{ab} values.   **Table 2.1** summarizes the $J_{ab}^{(1)}$, $J_{ab}^{(2)}$ and $J_{ab}^{(3)}$ values for **1b_O2D** and **1b** estimated by eqs. (12a)–(12c).   All the calculated J_{ab} values are negative, showing strong antiferromagnetic interactions between the Cu(II) ions.   Present results are rather close to the experimental value [16, 17] as compared with previous ab initio values by other groups [11–38].   However, the estimated magnitude is still larger than the experimental value [16, 17].   The experimental J_{ab} value of oxyHc has not been determined precisely yet since it is difficult to determine the accurate coupling constant of Hc experimentally because of the high molecular weight and low metal concentration [16, 17].   UHF underestimates the absolute value of J_{ab} in comparison with the experimental values, $|J_{ab}| > 300$ cm^{-1}.   The J_{ab} values for **1b**, listed in **Table 2.1**, are much smaller than those for **1b_O2**, indicating that the direct exchange interactions between the Cu(II) ions are negligible.   However, the UBLYP calculation for **1b** was not converged.   These results prove that the negative J_{ab} values for **1b_O2** arise from the bridging dioxygen.

Table 2.2 summarizes the singlet-triplet splitting energy ΔE $(=-2J_{ab})$ for the models of oxyHc obtained by this and other works.   In other works, the calculated values for the coupling constant $-2J_{ab}$ cover a range from 2480 to 5209 cm^{-1}.   The coupling constant ΔE for the model coordinated with NH_3 is 5209 cm^{-1} by UB3LYP, in contrast to that with methylimidazole, 2730 cm^{-1} by the same method.   The constants by CASPT2 decreases as CASPT2(8in10) > CASPT2(12in14) > CASPT2(12in14)+relativistic correction, indicating that the ΔE values decrease gradually as the higher level computations are utilized.   The UB2LYP can qualitatively reproduce the CASPT2

results.   The constants for the model with methylimidazole ligand are much closer to the lower limit of the constants obtained by an SQUID experiment [16, 17] than that for the model with NH_3 by CASPT2.   These results show that the ligand coordination effect is crucial for investigating the magnetic interaction more quantitatively.

Next, We have investigated the coordination ligand dependence on the magnetic couplings. The $|J_{ab}|$ values for models **a–c** were estimated as **a < b < c** as shown in **Table 2.3**.   The difference of $J_{ab}^{(3)}$ values between models **a** and **b** (**c**) was 200–300 cm^{-1}, indicating that the substitution from histidine to NH_3 is effective to the magnetic interaction.   While that between **b** and **c** was approximately 10 cm^{-1}, showing that the substitution from histidine to methylimidazole group is not serious for the magnetic coupling.

As for UB2LYP and UB3LYP the differences between $J_{ab}^{(1)}$ and $J_{ab}^{(3)}$ values by our AP procedure were approximately 100 and 450 cm^{-1}, while those between $J_{ab}^{(2)}$ and $J_{ab}^{(3)}$ values were 600 and 400 cm^{-1}, respectively.   These results indicate that this system belongs to the intermediate orbital interaction region, $|J_{ab}^{(2)}| < |J_{ab}^{(3)}| < |J_{ab}^{(1)}|$; note that $J_{ab}^{(1)} \cong J_{ab}^{(3)}$ for weak interaction systems, while $J_{ab}^{(2)} \cong J_{ab}^{(3)}$ for strong interaction ones.   Since we can estimate the chemical bonding region of **1z_O2D** using different computational schemes eqs. (12a)–(12c), J_{ab} values can be regarded as the sensitive parameter to diagnose the chemical bonding between the active core of **1z** and dioxygen.

The author has investigated the charge and spin density distribution for **1z_O2D** to understand the characteristics of the magnetic interactions.   As listed in **Table 2.4**, the charge density of O–O group varies from formal charge (–2.0) in **I** to 0.0 in the VB configuration **II** in **Figure 2.4 A**, indicating the back charge transfer from O_2^{2-} to Cu (II) ions.   The back charge transfer implies that the SE interaction is responsible for the strong antiferromagnetic coupling of Hc.   The positive charge densities of ligands for **1z_O2D** increase as **c < a < b**, showing that the charge transfer from the ligands to the Cu_2O_2 core of **1z_O2D** increases in the above order.   This tendency is irrespective to the computational methods (UB2LYP and UB3LYP).   The ligand to core charge transfer would suppress the back charge transfer from O_2 dianion to Cu(II) sites, namely SE interaction between Cu(II) ions.

In **Table 2.4**, the spin densities on Cu(II) ions are about 0.6 and 0.4 by UB2LYP and

UB3LYP, respectively.   The spin density populations calculated by UB2LYP and UB3LYP indicate the resonance state between the one-electron transfer VB configurations **III** and **IV** in **Figure 2.4 A**.   The spin densities on O_2 group are cancelled out in this resonance state **V**, namely intermediate valence state.

Judging from charge and spin densities of Cu_2O_2 core, the copper ion lies in the intermediate oxidation (IO) state (I < IO < II), while dioxygen in turn exists in the intermediate reduction (IR) state ($O_2^{1-} < O_2^{m-} < O_2^{2-}$; $1 < m < 2$) as shown in **V** of **Figure 2.4**.   The intermediate valence structure **V** expresses the coupling between Cu(IO) and O_2(IR) anion.   The intermediate valence structure is expressed by the superposition of the VB structures **I**, **III** and **IV** in the case of the VB-CI method.

In the models **a–c**, the total charge densities on O sites (O3 and O4) are −1.042, −1.133 and −1.130, respectively, showing that the charge transfer from O_2^{2-} to Cu(II) sites in **1a_O2D** is larger than those in **1b_O2D** and **1c_O2D**.   This tendency is similar as that of the absolute value of J_{ab}. The magnitude of charge transfer from the ligand **a** to the Cu_2O_2 core is smaller than that from ligands **b** and **c**, showing that NH_3 groups would suppress the back charge transfer from O_2^{2-} to Cu(II) sites more weakly than imidazole groups.   On the other hand, the spin density populations among models **a–c** are very close, the change of coordination ligands does not control the spin density of Cu_2O_2 core.

2.3.2 Natural orbitals and occupation numbers of 1z_O2D

The orbital correlation diagram revealed by the NO analysis is illustrated in **Figure 2.3**.   The singly bonding (SONO−1) and antibonding (SONO+1) occupied natural orbitals (SONOs) and their occupation numbers are expected to clarify the origin and the ligand coordination effects of the magnetic interaction and the difference of the electronic structures for **1z_O2D**.   **Figure 2.5** illustrates the SONOs of **1z_O2D** (**z = a–c**) in LS state by UB2LYP calculation.   It is found that bonding symmetric (S) d_{xy}–d_{xy} orbital of **1z** interacts with S-type orbitals (σ^* and π_v^*) of dioxygen in SONO−1, while SONO+1 consists of antisymmetric (A) d_{xy}+d_{xy} orbital and π_h^* one: this in turn indicates that π_h^* is stabilized by the symmetry-allowed orbital interaction to afford HOMO as shown in **Figures 2.3** and **2.6**.   We can observe from **Figure 2.5** that the SONOs delocalize on the

whole Cu_2O_2 core at the UB2LYP level.   The delocalized orbital on the xy-plane can be attributed to the antiferromagnetic SE interaction between the Cu(II) ions via dioxygen.   The symmetry and shape of SONOs are similar in the models **a–c**, implying that the orbital interactions of SONOs of the active core Cu_2O_2 in **1z_O2D** at $R = 0.4$ Å are related to same orbitals, d_{xy} orbitals of Cu ions and π^* ones of dioxygen.

T_i values estimated from the occupation numbers of SONO–1 and SONO+1 in **Table 2.5** were about 0.310, 0.268 and 0.271 for models, **1a_O2D**, **1b_O2D** and **1c_O2D**, by UB2LYP calculations, respectively, also indicating that the Cu sites intermediately interact with each other through the binding dioxygen.   The Cu_2O_2 bond is not a closed-shell type MO configuration **VI** (n_i = 2.0) in **Figure 2.4 B**, but by an open-shell configuration **VII**, where electrons partially occupy the antibonding SONO+1.   However, this open-shell MO configuration guarantees the strong antiferromagnetic SE interaction.   The occupation numbers of HOMO and LUMO are 1.997 and 0.003 by UB2LYP, respectively.   This shows the very weak SP effect under both UB2LYP approximations.   The magnitude of the T_i values of SONOs increases as **1b_O2D** $\cong$ **1c_O2D** < **1a_O2D**, indicating the same tendency of that of $|J_{ab}|$ values for **1z_O2D**.   Judging from charge density and T_i values of SONOs, **1a_O2D** estimated SE interaction between Cu(II) ions larger than **1b_O2D** and **1c_O2D**, resulting in providing larger absolute value of J_{ab}.   On the other hand, the occupation numbers of HOMO and LUMO in models **a–c** are close each other, indicating that SP effects are much smaller than SE interaction.   The NO analysis clearly demonstrates that the origin of the antiferromagnetic exchange interaction of Hc is the SE interactions via dioxygen and that **1z** and dioxygen show an intermediate orbital interaction ($0 < T_i < 1.0$) between **VI** and **VIII**. Therefore, we should utilize the AP-scheme in which we can deal with the intermediate orbital interaction in order to examine the magnetic interaction and the dioxygen binding process in the models of Hc.

2.4 Reversible Dioxygen Binding Processes for 1z and 2z

2.4.1 Potential energy surfaces for 1z_O2 and 2z_O2

The author has investigated the reversible dioxygen binding process for Hc, depicting the potential energy surfaces of **1z_O2X** and **2z_O2X** (**z** = a–c and **X** = **D** and **N**) by UB2LYP calculation.   **Figures 2.7–2.9** illustrate the potential energy surfaces for **1z_O2X** and **2z_O2X** in the HS and LS states before and after the AP correction for BS problem by the use of eq. (14).

The AP correction stabilizes the energy for **1_O2** in the region of $0 < R < 1.0$ Å.   It is noteworthy that the energy difference between singlet and triplet dioxygen becomes improved from ≈ 10 to ≈ 25 kcal mol^{-1} before and after the AP correction, respectively, in comparison to the experimental value, ≈ 22.5 kcal mol^{-1} [43, 44].   These results imply that the AP correction is necessary to depict the potential energy surface in LS state.

Figure 2.7 A shows the potential energy curves for **1a_O2X** in the range: $0.0 \leq R \leq 3.4$ Å. At $R = 3.4$ Å, namely dissociation distance, HS state of **1a_O2N** is the most stable in all states.   As dioxygen becomes close to the active site of **1a**, HS state of **1a_O2N** slightly rises up in energy. This small activation barrier in spite of the symmetry-allowed orbital interactions between **1a** and $^3O_2$ indicates that the non-least motion association path is more favorable for **1a_O2X**, as demonstrated in a recent paper [38].   At $R = 1.0$ Å, HS state of **1a_O2N** intersects that of **1a_O2D**. In other words, the interatomic distance $r2$ between dioxygen elongates from 1.2 to 1.4 Å.   Then, an approximate crossing point between the profiles of AP-LS and HS states of **1a_O2D** was estimated to occur at $R \approx 0.8$ Å.   The energy in AP-LS state of **1a_O2D** is lower than that in HS state of **1a_O2D** in the region: $0.0 < R < 0.8$ Å, implying that spin state of **1a_O2X** changes from triplet ground state to singlet one.   The orbital orthogonality between the antisymmetric $d_{xy}+d_{xy}$ and π_v^* orbitals gives rise to the spin-orbit interaction for the intersystem crossing as shown in **Figure 2.10**.   AP-LS state of **1a_O2D** is the most stable at $R = 0.6$ Å, indicating that the active core of **1a_O2** forms a butterfly structure.   The binding energy is exothermic, 4.63 kcal mol^{-1}, and is so small that dioxygen is bound to **1a** very weakly.   Judging from these results, it is difficult for **1a_O2X** to form a stable complex.   While, **Figure 2.7 B** illustrates the potential energy surface for **2a_O2X**.   In the entire region, the energies of all states of **2a_O2N** are more stable than those of **2a_O2D**.   Especially, HS state of **2a_O2N** is the most stable.   As dioxygen is apart from **2a**, the total energy decreases, indicating that O_2 dissociates from **2a** when the structure of **1a** is converted to that of **2a**.   When the distance between dioxygen is 1.2 Å, namely **O2N**, dioxygen hardly

interacts with the active core of **2a**.

Figure 2.8 A depicts an energy profile for **1b_O2** in the region from $R = 0.0$ to 3.4 Å. From **Figure 2.8 A**, the energy in HS state of **1b_O2N** is the lowest at the dissociation distance $R = 3.4$ Å. When dioxygen approaches the active core in **1b**, HS state of **1b_O2N** becomes stable. This indicates no activation barrier for the association reaction between **1b** and $^3O_2$ because of the strong orbital interactions. HS state of **1b_O2N** crosses over that of **1b_O2D** at $R \approx 1.0$ Å. Then, intersystem crossing from triplet state to singlet one occurs at $R = 0.9$ Å, where the spin-orbit interaction should play a crucial role. At last, **1b_O2D** reaches a minimum point at $R = 0.6$ A, indicating a butterfly structure in agreement with the experiment [16, 17]. The binding energy of **1b_O2** is exothermic, 13.75 kcal mol^{-1}, implying that **1b_O2X** can be stable. While, from **Figure 2.8 B**, which shows the potential curve for **2b_O2X**, we found that HS state of **2b_O2N** is more stable than other states in the whole region, and that the energy in HS state of **2b_O2N** decrease as the distance R between dioxygen and **2b** becomes large.

Figure 2.9 shows the potential energy surface for **1c_O2X** in the region from 0.0 to 2.4 Å. This figure is similar to **Figure 2.8 A**. The potential curve for **1c_O2N** in HS state crosses over that for **1c_O2D** in HS state at $R \approx 1.0$ Å. Intersystem crossing of **1c_O2D** from triplet state to singlet one occurs at $R = 0.9$ Å. **1c_O2D** also has a minimum point at $R = 0.6$ Å in AP-LS state, also indicating a butterfly structure in agreement with the experiment [16, 17]. The binding energy estimated with eq. (25) was 14.08 kcal mol^{-1}, showing that **1c_O2D** also forms a stable complex. The results clearly demonstrate that the realistic model is essential even for the qualitative purpose.

2.4.2 Charge and spin density distributions of 1z_O2 and 2z_O2

The variation of charge and spin density distributions provide the insight into the electron transfer region in dioxygen binding of Hc. The author has examined the variations of charge and spin density of Cu_2O_2 core in **1z_O2D** and **2z_O2N** in the HS state estimated by UB2LYP calculation with the change of R. The site numbers 1–4 of Cu_2O_2 core are shown in **Figure 2.2**.

The charge density curves of Cu1, Cu2, O3 and O4 sites for **1c_O2D**, shown in **Figure 2.11** (**A1**), leads to the following results; (i) the net charge on Cu(I) of fragment **1c** is about 0.5, while it becomes about 1.0 for **1c_O2D**, (ii) electron transfer from the Cu sites to the O sites when the

dioxygen is close to **1z** by UB2LYP calculation and (iii) Cu ions are converted from the Cu(I) to the intermediate oxidation state, Cu(IO), and the oxygen molecule (O_2) changes to intermediate reduction (IR) state (O_2^{m-}; $1 < m < 2$) in the region from $R = 0.8$ to 1.6 Å. These results agree well with the experimental results. The change in the spin density with the variation of R has also been investigated for **1c_O2D**. As shown in **Figure 2.11 (B1)**, the spin densities on O sites reduces, while those on Cu sites increases, indicating that the spin density is transferred from O to Cu, namely the O_2 part changes from triplet oxygen molecule to trapped O_2 dianion as the intermolecular distance R decreases. The deviation between the spin densities on Cu1 and Cu2 sites is the largest at $R = 1.4$ Å, implying that the one electron transfer occurs to afford the Cu(I)–Cu(II) mixed valence state. The charge and spin density curves for **1a_O2D** and **1b_O2D** were also depicted in **Figures 2.12 and 2.13**, respectively. In all the models, charge and spin distribution show the same tendency, indicating that ligands **a–c** provide the same effects to the binding of dioxygen to oxyHc qualitatively.

On the other hand, the variation of the charge and spin density distributions for **2a_O2D** and **2b_O2D** are shown in **Figures 2.12 (A2)** and **(B2)** and **2.13 (A2)** and **(B2)**. We observe no change in the populations when R increases from 0.0 to 3.4 Å. These results reflect the repulsive interaction between the Cu ions of **2z** and dioxygen. The charge and spin density distributions of **2a_O2D** are similar to those of **2b_O2D** in the whole region, implying that the common repulsive interaction is more predominant in the dissociation of oxygen molecule from deoxyHc than the orbital interaction stabilization of ligands **a** and **b**.

2.4.3 Chemical Indices of 1z_O2D

The ab initio calculations of $J_{ab}^{(i)}$ ($i = 1$–3) and the NO analysis clearly demonstrate that the Cu_2O_2 bond exhibits an intermediate bonding. Therefore, effective bond order (b), decrease of effective bond order (Δb), unpaired electron density (U), information entropy (I), spin density index (Q) and diradical character (Y) should be useful indices for the investigation of bond character. Using the occupation numbers of SONOs, these indices for dioxygen binding process of **1a_O2D** and **1b_O2D** can be estimated with eqs. (24a)–(24d). **Figure 2.14** depicts variations of these chemical indices with change of the distance R by the UB2LYP method.

General tendencies of changes of the chemical indices for $Cu(\mu\text{-}\eta^2;\eta^2 O_2)Cu$ structure in the course of the reversible dioxygen binding of **1a** and **1b** are in the following order in the whole region.

$$Y < \Delta b \cong I < U < Q. \tag{26}$$

In **Figure 2.14**, spin density index Q changes from 1.0 to 0.9 with the approach of dioxygen to **1a** and **1b**, showing that the electron pair remains to be splitting because of the electron correlation (EC) effect. The similar behavior is recognized for the U value which is equivalent to the deviation for exact singlet value $^{LS}\langle S^2 \rangle = 0$ for the BS solution, indicating that the EC effect is significant for **1a** and **1b**. On the other hand, the open-shell character Y, which characterize the localization of electron occupying SONOs, sharply decreases from 1.0 to 0.4, implying that the electron delocalizes between spin sites. The information entropy I and the decrease of the effective bond order Δb exhibit intermediate behaviors between Q and Y values. Therefore, they could be regarded as useful indices to diagnose the bond nature. The bond order and information entropy are the measures of the strength of orbital interaction. Judging from the variation of these chemical indices, **1z_O2** belongs to the intermediate orbital interaction region when dioxygen is bound to **1z**. This is reason why the reversible dioxygen binding is feasible in Hc.

The variation of chemical indices of **1a_O2** in the dioxygen binding process by UB2LYP methods are illustrated in **Figure 2.14 A**. As dioxygen becomes close to **1a**, the indices suddenly reduce at $R = 1.2$ Å. This shows that the orbital interaction between dioxygen and **1a** in the region from 3.4 to 1.2 Å is weak, implying that the repulsive interaction predominantly contributes the total energy of **1a_O2**. Consequently, this would result in rising the total energy of the symmetry-constrained path for **1a_O2**. While, from **Figure 2.14 B**, it is found that the Y, Δb and I values smoothly reduce from the range: $R = 2.8$ Å in the course of the dioxygen binding of **1b**, and the U and Q values decreased at $R = 1.2$ Å, indicating that the symmetry-allowed orbital interactions are operate in $R = 1.2–3.4$ Å. Indeed, the orbital interaction is stronger than the repulsive one, resulting in stabilization of the total energy with the approach of dioxygen to **1b**. The chemical indices are wholly compatible with the energetics.

2.5 Discussion and Concluding Remarks

2.5.1 Comparison of the computational schemes of J_{ab} values

The author has compared three computational schemes (12a)–(12c) of the effective exchange integrals for the Cu_2O_2 cores in **1z_O2**. The calculated $J_{ab}^{(i)}$ (i = 1–3) are considerably different among them: note that our $J_{ab}^{(3)}$(AP) values are almost equal to $J_{ab}^{(1)}$(GND) in many molecular magnetic materials where the orbital overlaps (T_i) between magnetic orbitals are negligible. This in turn indicates that the copper–oxygen bond in Hc is specific because of the nonnegligible orbital overlap (T_i = 0.2–0.3 by UB2LYP, and T_i = 0.5–0.6 by UB3LYP). The orbital overlap T_i becomes close to 1.0 for copper oxides if pure DFT calculations such as BLYP are employed. This implies that the other scheme $J_{ab}^{(2)}$(GND BR) becomes rather useful for ab initio computations of J_{ab} values for the species. From present computational results, our scheme $J_{ab}^{(3)}$(AP) works well in whole region ($0 \leq T_i \leq 1$), being applicable to depict the potential energy curves as shown in **Figure 2.7**.

2.5.2 Ligand coordination effects to the magnetic interaction of dioxygen binding oxyhemocyanin

As mentioned in introduction, ammonia (NH_3) has been used as the simplest model for ligands in Hc in many previous ab initio computations. Here, the author has examined ligand coordination effects by replacing NH_3 (**a**) with methylimidazole (**b**) and histidine (**c**). It was found that the J_{ab} values are sensitive to change of ligands (**a, b** and **c**) because the Cu_2O_2 core lies in the labile bonding region. The ligand coordination effects are also remarkable for strength of the symmetry-allowed orbital interactions between symmetric (S) d_{xy}–d_{xy} of **1z** and π_v^* and σ^* of O_2 and between antisymmetric (A) d_{xy}+d_{xy} and π_h^*. In the present chapter, the orientations of ligands to the active core, which give rise to the ligand field, were similar in all the models. The author also estimates the magnetic coupling of geometry optimized **1a_O2D**, which is the geometry optimization correction to Cu_2O_2, by UB2LYP calculation (-1831 cm^{-1}). The difference of ligand coordination of NH_3 to the active core can be estimated approximately 400 cm^{-1}. Judging from these results, both the kind of ligands and the ligand coordination to the Cu_2O_2 core are influential to the

magnetic couplings, showing the necessity of realistic models for the theoretical calculations.

2.5.3 The nature of the copper–oxygen bond

In this chapter, the structural parameters of **1_O2** and **2_O2** were fixed in all calculations except for R and $r2$. Even under this assumption, the results show that the **1b_O2** and **1c_O2** forms stable complexes, while **1a_O2D** forms an unstable one. On the other hand, in **2a_O2** and **2b_O2** dioxygen dissociates from **2a** and **2b**, indicating that dioxygen dissociates from Hc when the structure of Hc is converted to the deoxygenated structure. Judging from the potential energy curve and the variation of the charge and spin density population of **1z_O2D**, we can demonstrate the dioxygen binding of **1z** as follows. When dioxygen is apart from **1z**, namely $R = 3.4$ Å, the electronic structures at the HS and LS states are $^1[Cu(I)–Cu(I)]+^3O_2$ and $^1[Cu(I)–Cu(I)]+^1O_2$, respectively. As the oxygen molecule becomes close to **1z**, first, the stepwise electron transfer occurs from antisymmetrical $d_{xy}+d_{xy}$ orbital to π_h^* one and from symmetrical $d_{xy}-d_{xy}$ orbital to π_v^* one, and they change to the formal two-electron transfer configurations at last: $^3[Cu(II)(\mu-\eta^2;\eta^2O_2^{2-})Cu(II)]$ and $^1[Cu(II)(\mu-\eta^2;\eta^2O_2^{2-})Cu(II)]$. However the back charge transfer from O_2^{2-} to Cu(II) ions take place because of intermediate ligand fields, affording the intermediate valence structure **VII**; $^{1,3}[Cu(IO)O_2^{m-}Cu(IO)]$, namely intermediate reduction state dioxygen (O_2^{m-}) plus intermediate oxidation state, Cu(IO), copper dimer, even if $r2 = 1.4$ Å is assumed. The electronic structure of this intermediate should be sensitive to ligand conformation and other effects, suggesting a possibility of active control of reversible oxygen transport.

2.5.4 Ligand coordination effects to the dioxygen binding process of hemocyanin

Two differences were found from the shape of potential energy surfaces for **1a_O2**, **1b_O2** and **1c_O2**. One is that the binding energies were 4.63, 13.75 and 14.08 kcal mol^{-1}, respectively. The difference of the binding energy can be understood from the orbital energies of bonding symmetrical (S) and antibonding antisymmetrical (A) $d_{xy}\pm d_{xy}$ orbitals of **1z**. As shown in **Figure 2.3**, the SONOs of **1z_O2** were constructed of bonding and antibonding $d_{xy}\pm d_{xy}$ orbitals of **1z** and π_h^* and π_v^* orbitals of dioxygen. In the NH$_3$ ligands **a**, the α and β orbital energies corresponding to symmetrical and antisymmetrical $d_{xy}\pm d_{xy}$ orbitals (-15.83 and -14.62 eV) were much smaller than

those of $\pi_h{}^*$ and $\pi_v{}^*$ orbitals of dioxygen (–10.91 and –0.932 eV), as shown in **Figure 2.15 A**, indicating that $d_{xy} \pm d_{xy}$ orbitals interact with π^* orbitals of dioxygen weakly. In the other words, the CT excitation energy from S and A-type MOs of **1a** to $\pi_h{}^*$ and $\pi_v{}^*$ orbitals of O_2 to afford the CT ($1a^+O_2^-$) state is large as shown in **Figure 2.15 B**, and the stabilization energy by the configuration mixing between CT ($1a^+O_2^-$) and no CT ($1a + O_2$) is small [44]. While, the α and β orbital energies corresponding to S and A-type $d_{xy} \pm d_{xy}$ orbitals (–13.65 and –12.30 eV for **1b** and –13.92 and –12.51 eV for **1c**) were closer to those of $\pi_h{}^*$ and $\pi_v{}^*$ orbitals of dioxygen than those for **1a**, showing that interactions between S and A-type $d_{xy} \pm d_{xy}$ and $\pi_h{}^*$ and $\pi_v{}^*$ orbitals in the imidazole ligands **b** and **c** are stronger than those in the NH_3 ligands **a**. Such the difference in CT energy between from A-type $d_{xy} + d_{xy}$ orbital to $\pi_h{}^*$ one and from S-type $d_{xy} - d_{xy}$ orbital to $\pi_v{}^*$ one; $E_{CT}(A) < E_{CT}(S)$, leads to the stepwise two-electron transfer mechanism in dioxygen binding of Hc. The CT excitation energies become smaller in these complexes as illustrated in **Figure 2.15 B**, indicating the strong configuration mixing [45]. Such strong CT interactions between **1b** (**1c**) and dioxygen are ascribed to the origin of the larger binding energy of **1b_O2** (**1c_O2**) than that of **1a_O2** as shown in **Figure 2.15 B**. The author describes from these results that [Cu(HBpz₃)]₂ ((HBpz₃) = hydrotris(pyrazolyl)borate) [18, 19] (**1d_O2**) synthesized by Kitajima and co-workers binds dioxygen irreversibly because $HBpz_3$ groups show electron-donating character and raise the orbital energy corresponding to S and A type $d_{xy} \pm d_{xy}$ orbitals of [Cu(HBpz₃)]₂ near that to π^* orbitals of O_2, giving rise to the strong bonding. Probably, strong CTs from ligands to the Cu_2O_2 core stabilize the formal two-electron transfer configuration: ${}^1[Cu(II)O_2{}^{2-}Cu(II)]$. From the MO picture in **Figure 2.4 B**, their complexes would be described by the stable closed-shell configuration **VI**, leading to nonreversible dioxygen binding. In addition to such electronic effect, steric and geometrical effects also play important roles in controlling the O_2-binding energy. For example, [Cu₂O₂(L)](PF₆)₂ (**1e_O2**) (L = 1,2-bis[2-{bis(6-methyl-2-pyridyl)methyl}-6-pyridyl]ethane) [21] exhibits reversible dioxygen binding because of distortion of the Cu_2O_2 core like Hc. For the planar Cu_2O_2 core, the $\pi_v{}^*$ orbital in SONO–1 is replaced by the σ^*-orbital of dioxygen because of symmetry requirement, and so we must discuss the oxygen activation instead of reversible dioxygen binding. Further studies on this point are in progress.

Secondary, the energy slightly increased for **1a_O2** while slightly decreased for **1b_O2** and

1c_O2 in the region from 3.4 to 1.5 Å as dioxygen approached **1z**. This small activation barrier for the least-motion association path of **1a_O2** implies that the nonleast-path is favorable as revealed very recently [38]. However, the energy difference between the least- and nonleast-association paths is not so large because of no activation barrier and symmetry-allowedness for **1b_O2** and **1c_O2** system. Probably, molecular dynamics calculations would be necessary for further discussions at this point.

2.5.5 Chemical bond indices

Here, the author has examined five chemical indices to elucidate the nature of the Cu_2O_2 bond and bond-formation process between **1z** and O_2. The effective bond order (*b*) and information entropy (*I*) exhibit similar behaviors responsible for the bond formation via electron delocalizations. On the other hand, spin density index (*Q*) and unpaired electron density (*U*) are responsible for the electron correlation (EC) effects and are about 0.7–1.0 throughout the reaction, indicating an important role of the EC effect. The electron delocalizations and electron correlations are competitive in the copper–oxygen systems. This is reason why the author should utilize UB2LYP calculation instead of UB3LYP and UBLYP ones. The open-shell character (*Y*) sharply decreases in the course of the association process between **1z** and O_2, showing that the contribution of the doubly excited configuration in CASSCF and CASPT2, if possible, shows the same tendency. Thus, the chemical indices are useful for elucidation of the nature of chemical bonds on the basis of the broken-symmetry (BS) DFT calculations.

2.5.6 Concluding remarks

The ligand coordination effect for magnetic interaction has been examined by hybrid density functional calculation (HDFT) such as UB2LYP calculations. The author employed NH_3 (**a**), methylimidazole (**b**) and histidine (**c**) as the ligands coordinated to the copper cores Cu(II)–Cu(II) (**1**) and Cu(I)–Cu(I) (**2**). Judging from investigation of the ligand coordination effects, the difference between NH_3 and imidazole as the ligands coordinated to the active site is influential to the magnetic couplings for **1z_O2**, but ligand field given by the coordination of ligands is also effective.

On the other hand, in order to understand the dioxygen binding process of Hc, the author has also performed UB2LYP calculation for **1z_O2** and **2z_O2** (**z = a–c**) using two parameters for O–O length, 1.2Å (**O2N**) for molecular oxygen and 1.4Å (**O2D**) for peroxide. With the respect to the dioxygen binding process, the author concludes as follow: (i) the structural two-electron from deoxy to oxyHc is expected to play a crucial role in controlling the stepwise charge transfer from antisymmetrical $d_{xy}+d_{xy}$ orbital to $\pi_h{}^*$ one and from symmetrical $d_{xy}-d_{xy}$ orbital to $\pi_v{}^*$ one of Hc, resulting in addition and dissociation of dioxygen; (ii) however, the back charge transfer from $O_2{}^{2-}$ to Cu(II) ions occurs to afford the intermediate valence structure $[Cu(IO)O_2{}^{m-}Cu(IO)]$ even for *r2* = 1.4 Å; (iii) the substitution of coordination ligands influences the binding energy and the shapes of potential energy surfaces of **1z_O2** due to the strength of the mixing between the ground and the charge transfer states; (iv) the orbital interactions between symmetrical and antisymmetrical $d_{xy} \pm d_{xy}$ orbitals and $\pi_h{}^*$ and $\pi_v{}^*$ ones in the imidazole ligands **b** and **c** are stronger than those in the NH_3 ligands **a**, leading to the larger binding energy of **1b_O2** (**1c_O2**) than **1a_O2**.

In this chapter, AP-scheme enables us to depict the smooth variation of potential energy surfaces for the dioxygen binding process of Hc. Applications of the AP scheme to the LS state have attracted recent interest in relation to biologically important binuclear transition metal complexes involved in enzymes [46, 47]. Since the J_{ab} values for these complexes have been determined experimentally, the AP-DFT calculations can be used for examination of reliabilities of the DFT solutions for searching the transition structures of enzyme reactions [46, 47]. The chemical indices such as effective bond order and information entropy are useful for elucidation of the nature of chemical bonds based on the broken-symmetry (BS) DFT calculation.

Table 2.1. Effective exchange interactions $(J_{ab})^{a,b}$ calculated for **1b_O2D** by UHF, UB2LYP, UB3LYP and UBLYP calculations

Model	Method	$J_{ab}^{(1)}$	$J_{ab}^{(2)}$	$J_{ab}^{(3)}$
1b_O2D	UHF	–217.1	–108.6	–216.4
	UB2LYP	–1310	–654.9	–1219
	UB3LYP	–1815	–907.6	–1365
	UBLYP	–2879	–1440	–1542
1b	UHF	1.001	0.500	1.001
	UB2LYP	–3.913	–1.957	–3.918
	UB3LYP	18.89	9.443	18.89

$^a J_{ab}$ are shown in cm^{-1}. ^{b} |J_{ab}(exp.)| > 300 cm^{-1} for **1_O2**.

Table 2.2.   Singlet–Triplet Splitting ΔE for models of oxyhemocyanin

Ligand	Method	$\Delta E \ (= -2J_{ab})^a$	Ref.
NH$_3$ **a**	VB-CI	2480	[26]
	UB2LYP	3362	
	UB3LYP	5209	[35]
	CASPT2(8in10)^b	4445	[35]
	CASPT2(12in14)^b	4288	[35]
	CASPT2(12in14)+relativistic corrections^b	4209	[35]
methylimidazole **b**	UHF	432.8	
	UB2LYP	2438	
	UB3LYP	2730	
	UBLYP	3084	
	exp.	>600	

^{a}In cm^{-1}. ^{b}Symbol ($m$in$n$) means m-electron and n-orbital in active space.

Table 2.3. Effective exchange interactions $(J_{ab})^{a,b}$ calculated for **1z_O2A** (z = a–c) by UB2LYP and UB3LYP methods

Ligand		$J_{ab}^{(1)}$	$J_{ab}^{(2)}$	$J_{ab}^{(3)}$
NH_3 **a**	UB2LYP	−1606	−803.0	−1461
	UB3LYP	−1585	−907.6	−1185
methylimidazole **b**	UB2LYP	−1310	−654.9	−1219
	UB3LYP	−1815	−908.0	−1365
histidine **c**	UB2LYP	−1327	−663.3	−1234
	UB3LYP	−1814	−907.2	−1361

$^a J_{ab}$ are shown in cm^{-1}. ^{b} |J_{ab}(exp.)| > 300 cm^{-1} for **1_O2**.

Table 2.4. Charge densities and spin densities of **1z_O2A** (z = a–c) by the UB2LYP and UB3LYP calculations in the LS state

model	Methods		Cu1[a]	Cu2[a]	O3[a]	O4[a]	Ligand
a	UB2LYP	Charge	0.944	1.079	−0.433	−0.609	1.019
		Spin	0.621	−0.639	0.038	−0.050	0.030
	UB3LYP	Charge	0.681	0.860	−0.281	−0.451	1.191
		Spin	0.359	−0.388	0.047	−0.035	0.017
b	UB2LYP	Charge	0.943	1.073	−0.490	−0.643	1.117
		Spin	0.671	−0.669	0.009	−0.059	0.048
	UB3LYP	Charge	0.622	0.814	−0.333	−0.485	1.382
		Spin	0.378	−0.420	0.039	−0.038	0.041
c	UB2LYP	Charge	1.076	0.941	−0.487	−0.643	1.113
		Spin	0.671	−0.668	−0.014	0.055	−0.044
	UB3LYP	Charge	0.817	0.620	−0.330	−0.485	1.378
		Spin	0.419	−0.373	−0.044	0.034	−0.036

[a] The site numbers are shown in **Figure 2.1.**

Table 2.5. Occupation numbers of HOMO, SONO and LUMO of **1z_O2A** (**z** = **a–c**) by the UB2LYP and UB3LYP calculations in the LS state

| model	method	HOMO	SONO	SONO'	LUMO
a	UB2LYP	1.997	1.310	0.690	0.003
	UB3LYP	1.999	1.576	0.424	0.001
b	UB2LYP	1.997	1.268	0.732	0.003
	UB3LYP	1.999	1.570	0.430	0.001
c	UB2LYP	1.997	1.271	0.729	0.003
	UB3LYP	1.999	1.573	0.427	0.001
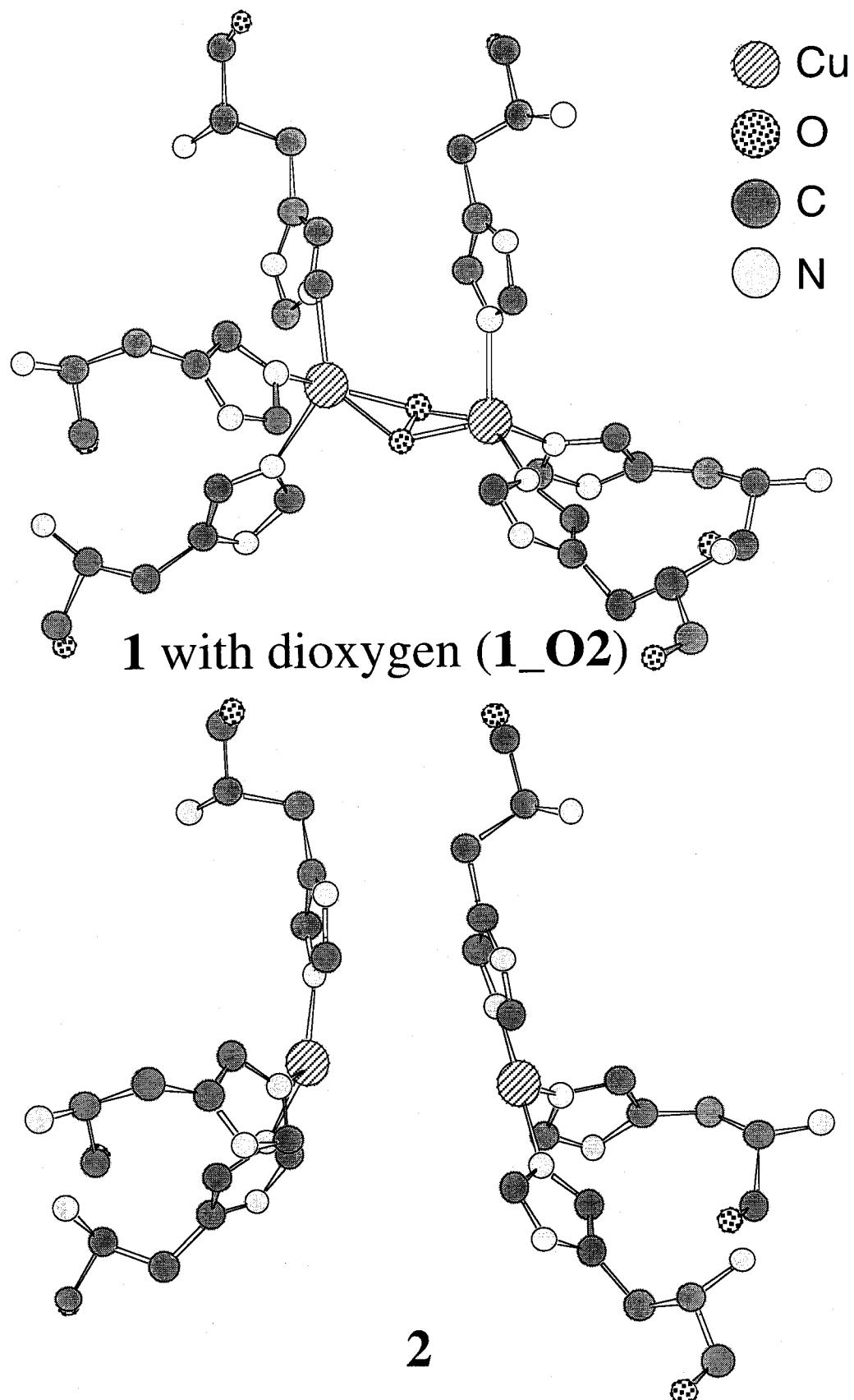
Figure 2.1.   X-ray crystallographic structures of a oxyhemocyanin (**1**) with oxygen (**1_O2**), and a deoxyhemocyanin (**2**), respectively.

$r1 = 3.54$ Å : oxy   **1**
       4.60 Å : deoxy **2**

$L = NH_3$ **a**

    $= -N$ (methylimidazole with CH_3) **b**

    $= -N$ (histidine with COOH, C–H, NH_2) **c**
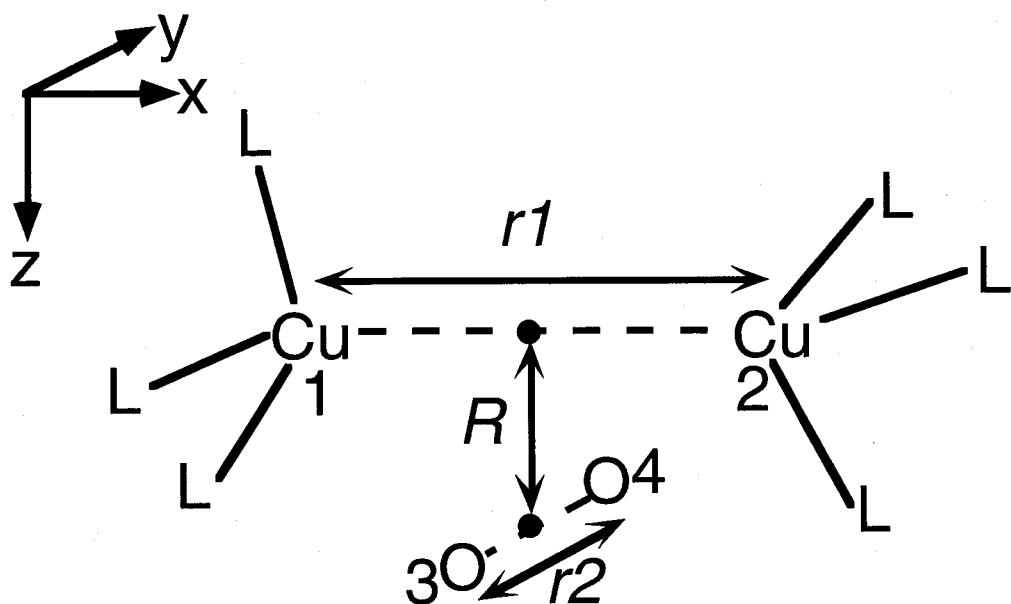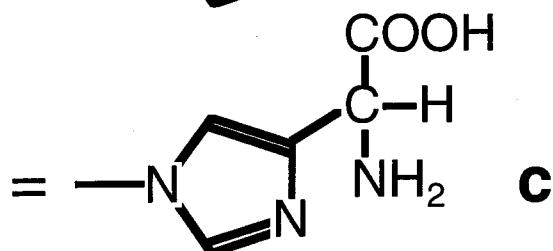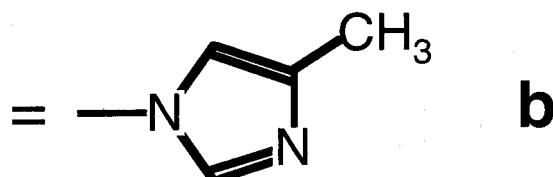
$r2 = 1.4$ Å : O_2^{2-} **O2D**
       1.2 Å : O_2 **O2N**

Figure 2.2.   A schematic model of hemocyanin with dioxygen **1z_O2** and **2z_O2** (z = a–c). L denotes the ligands **a** (NH3), **b** (methylimidazole) and **c** (histidine) utilized in the present study. The distance between dioxygen represents *r1*. The distance *R* between the centers of Cu–Cu and O–O axes is shown in **1z_O2** and **2z_O2**. Site numbers 1–4 are illustrated in **1z_O2** and **2z_O2**.
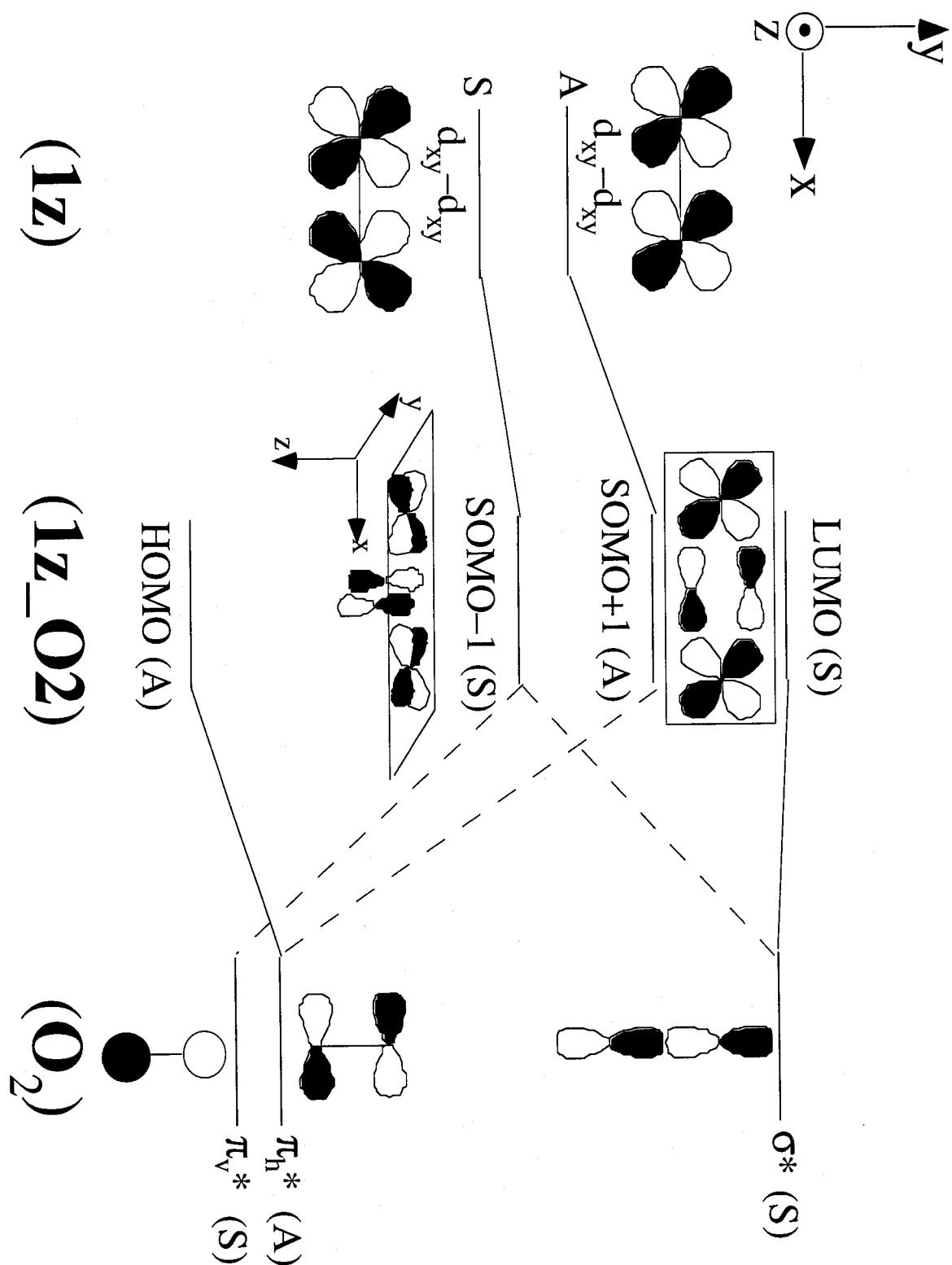
Figure 2.3. Orbital diagram of Cu_2O_2 bond and schematic representation of SOMOs.
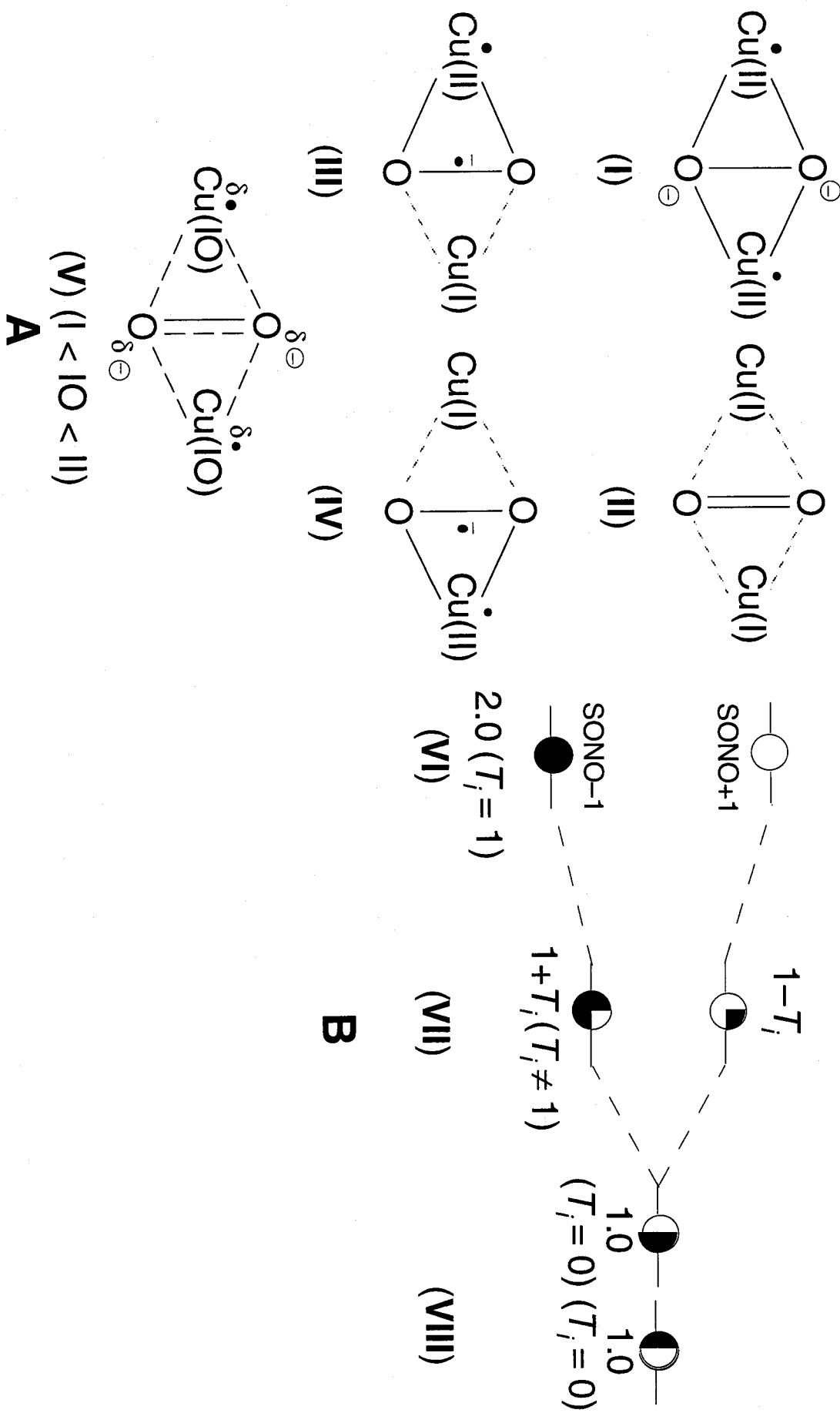
Figure 2.4. Valence bond description of Cu_2O_2 bond (**A**) and schematic representation of SONOs in the covalent (**VI**), intermediate (**VII**) and dissociation (**VIII**) bonding regions (**B**).
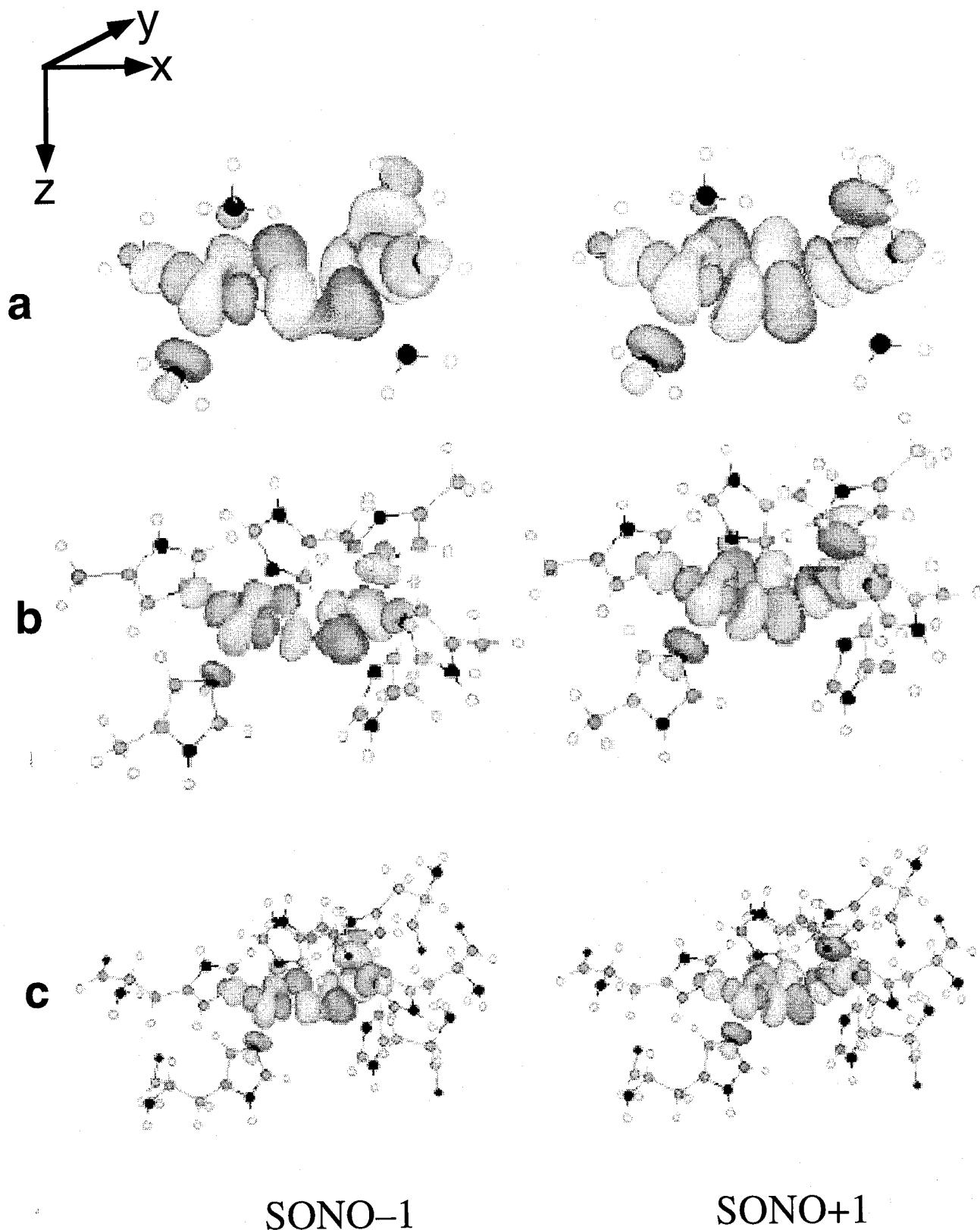
Figure 2.5. Singly occupied bonding (SONO–1) and antibonding (SONO+1) natural orbitals (SONOs) for the LS state of **1z_O2** by UB2LYP.
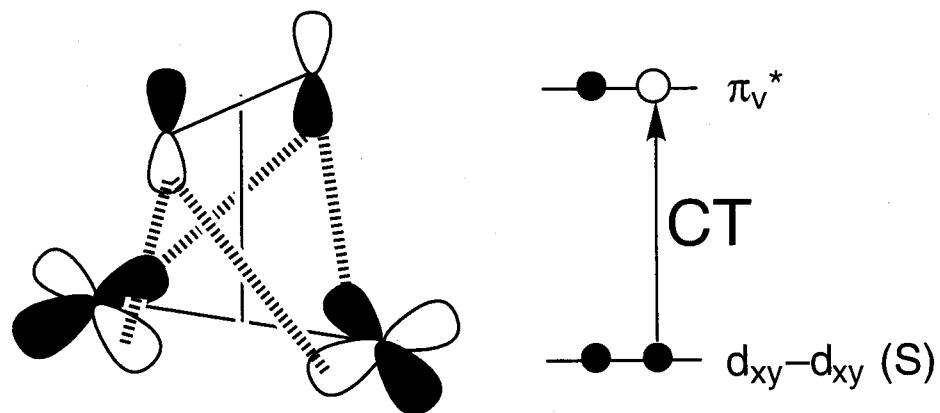
Symmetry-Allowed
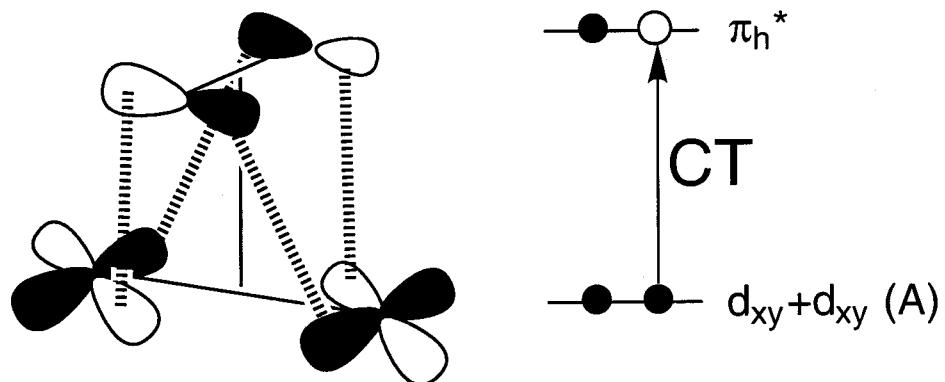
Symmetry-Allowed

Figure 2.6. Schematic represents of symmetry-allowed orbital interaction between d_{xy}–d_{xy} and π^* orbitals
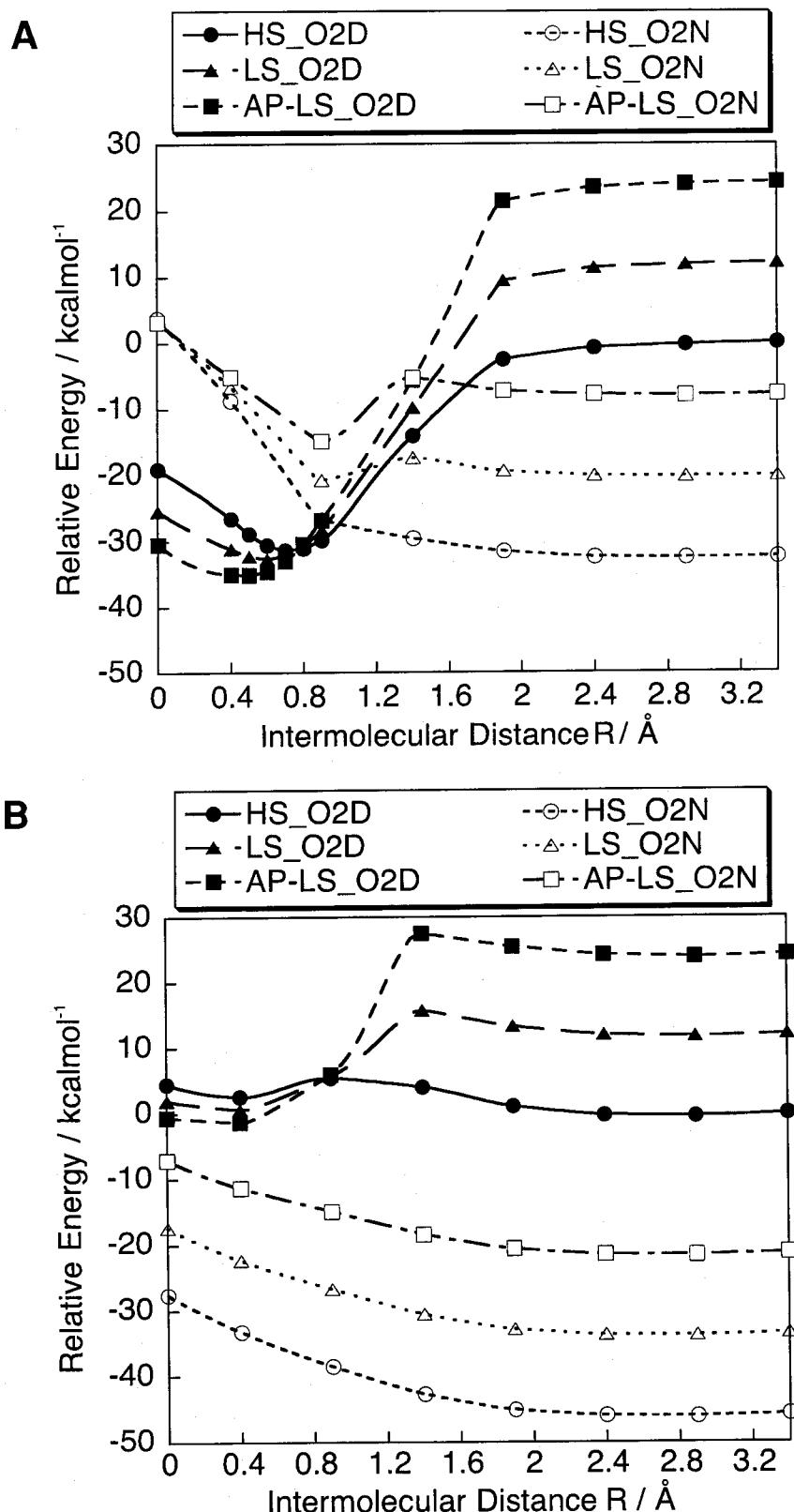
Figure 2.7. Potential curves at the HS, LS and AP-LS states of **1a_O2D** and **1a_O2N** (A) and **2a_O2D** and **2a_O2N** (B) by UB2LYP in the region from $R = 0.0$ to 3.4 Å.
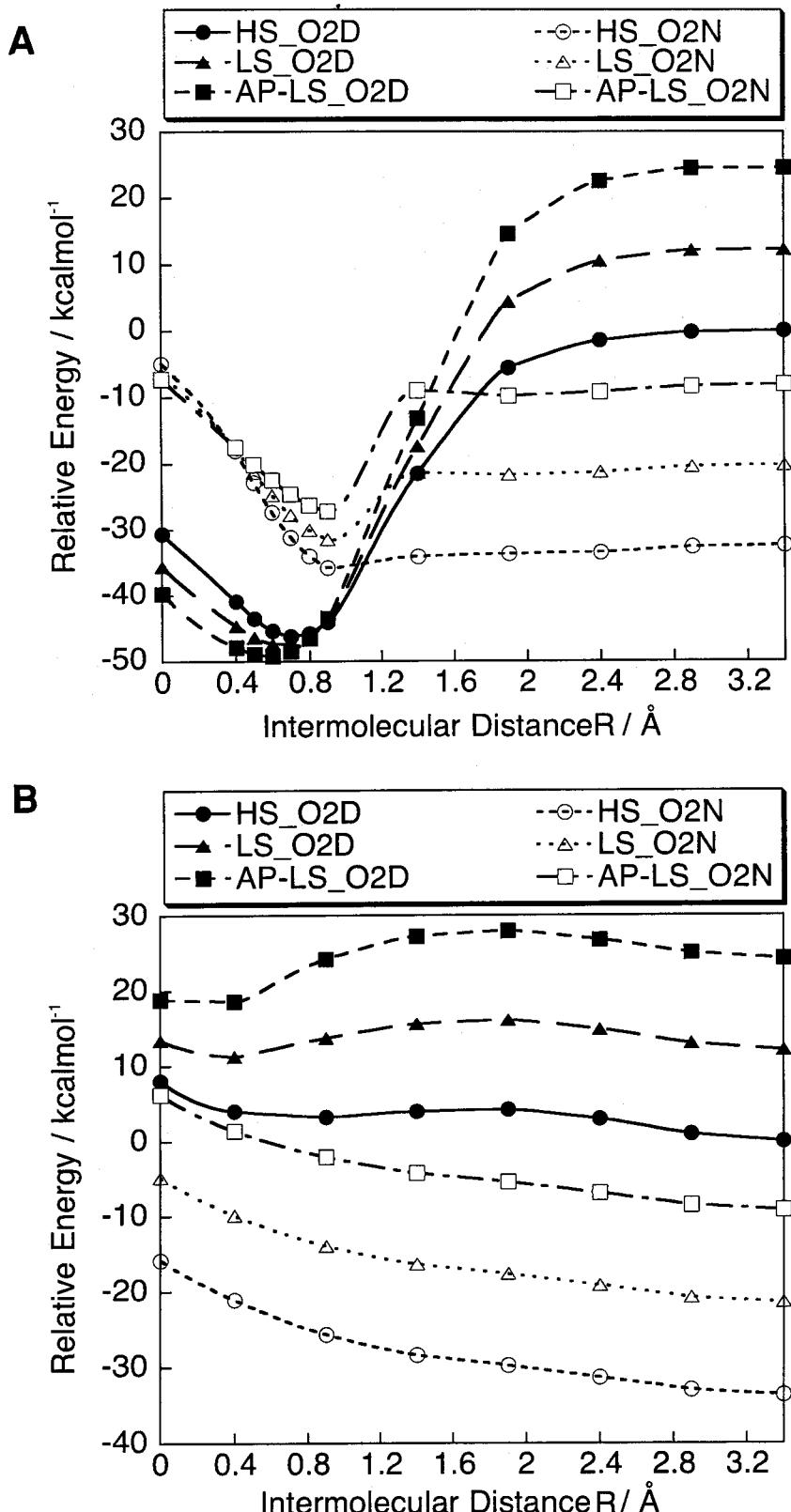
Figure 2.8.   Potential curves at the HS, LS and AP-LS states of **1b_O2D** and
1b_O2N (**A**) and **2b_O2D** and **2b_O2N** (**B**) by UB2LYP in the
region from R = 0.0 to 3.4 Å.
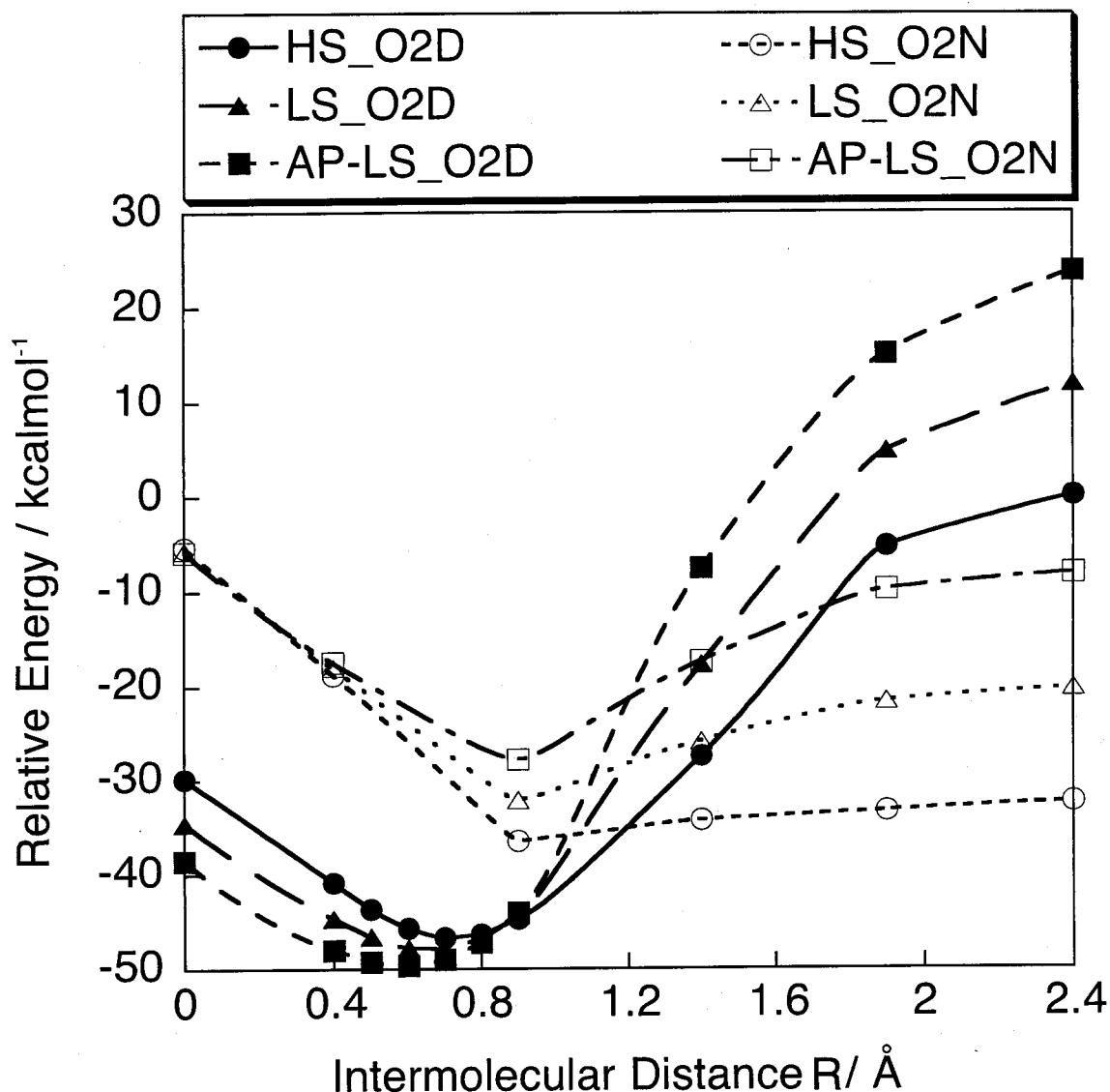
Figure 2.9.   Potential curves at the HS, LS and AP-LS states of **1c_O2D** and **1c_O2N** by UB2LYP in the region from R = 0.0 to 2.4 Å.

CT state
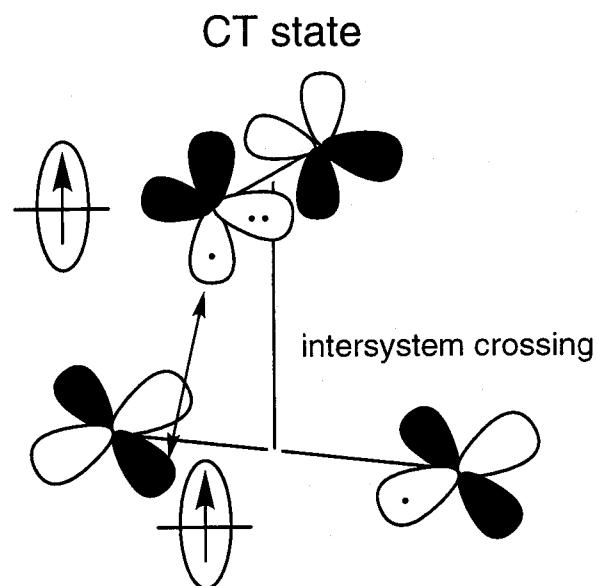
$$<\pi_v^* | S.O. | d_{xy} + d_{xy}\ (A)> \neq 0$$
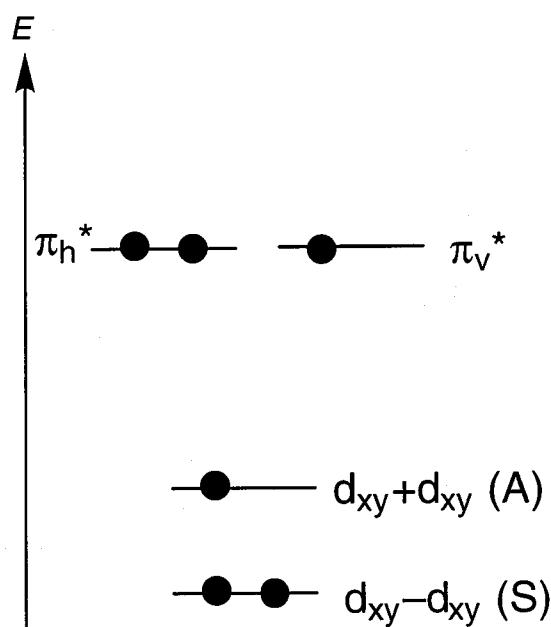
Figure 2.10   Schematic representation of the orbital orthogonality
between $d_{xy} + d_{xy}$ and π_v^* orbitals
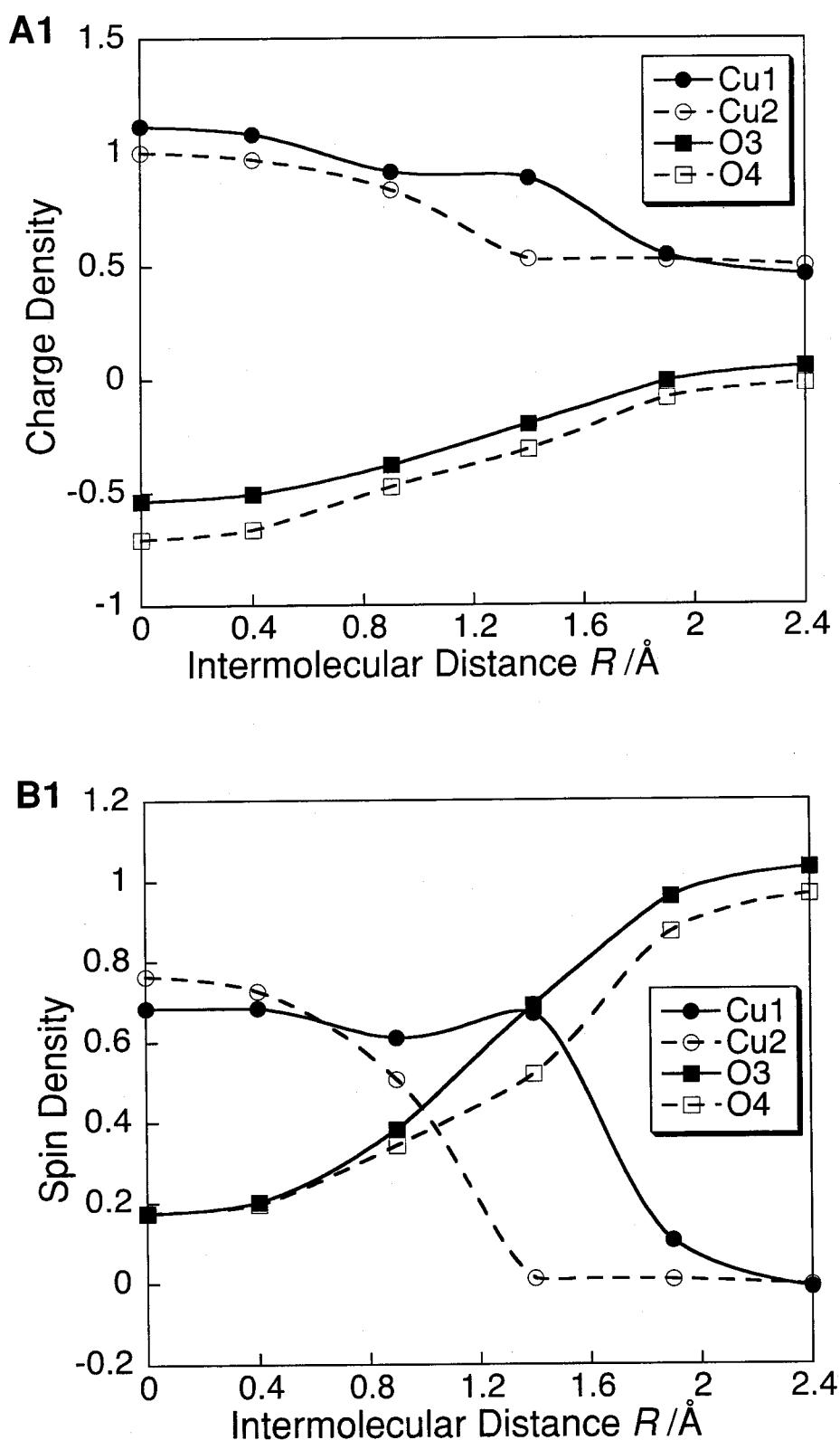
Figure 2.11.   Charge (A) and spin (B) densities at the HS states of **1c_O2** (**1**) by UB2LYP.
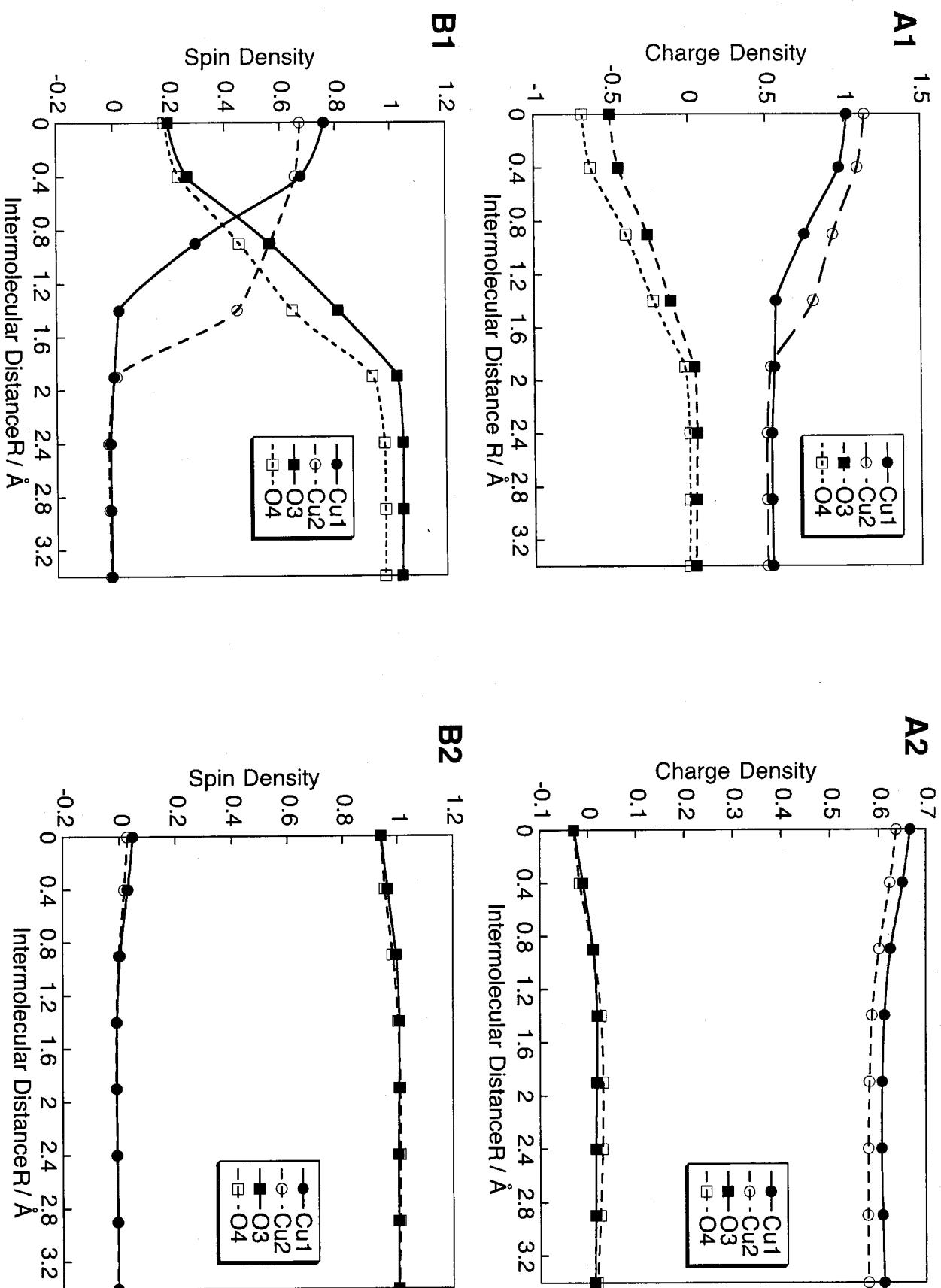
Figure 2.12.   Charge (A) and spin (B) densities at the HS states of **1a_O2** (1) and **2a_O2** (2) by UB2LYP.
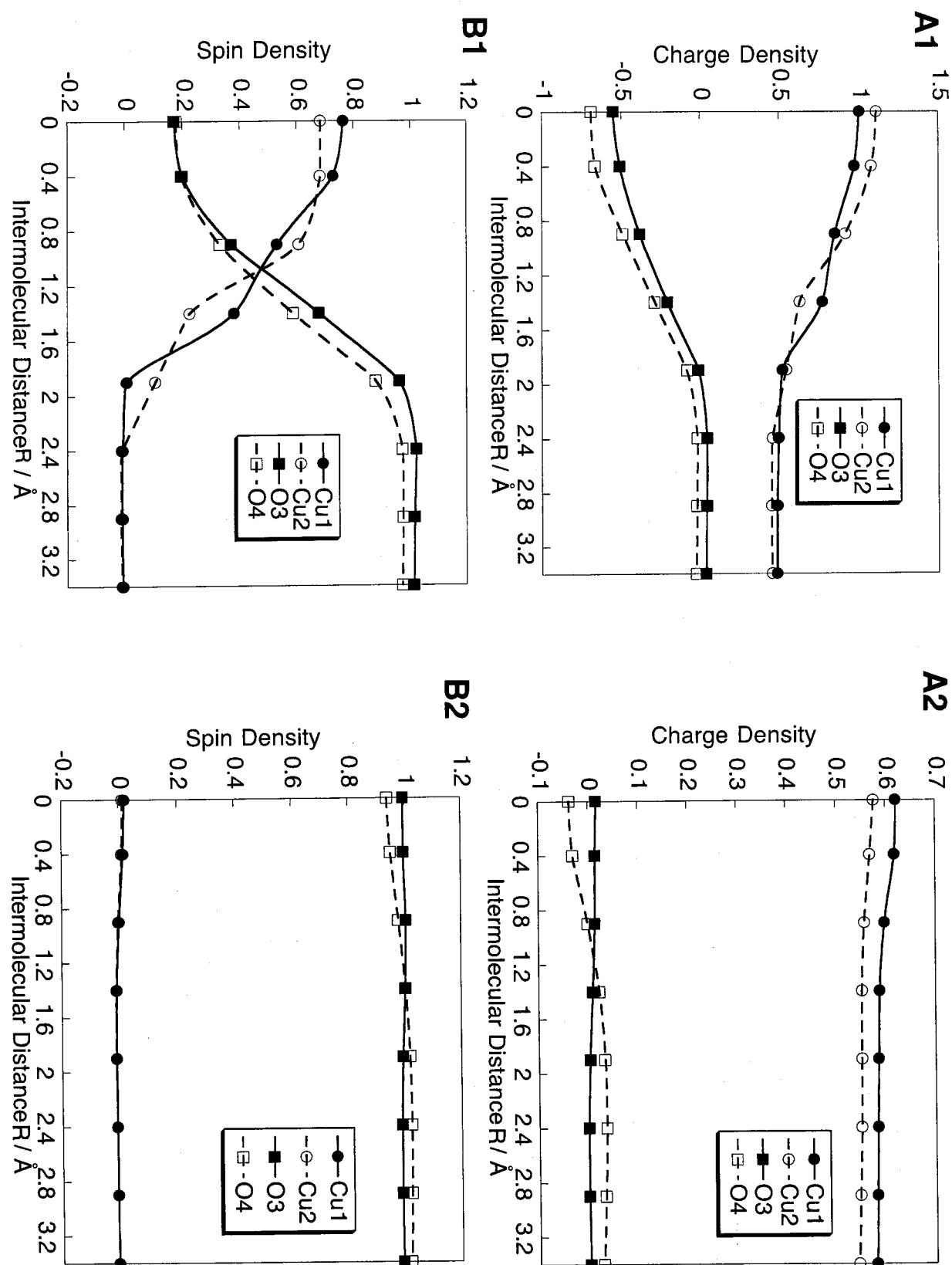
Figure 2.13. Charge (A) and spin (B) densities at the HS states of 1b_O2 (1) and 2b_O2 (2) by UB2LYP.
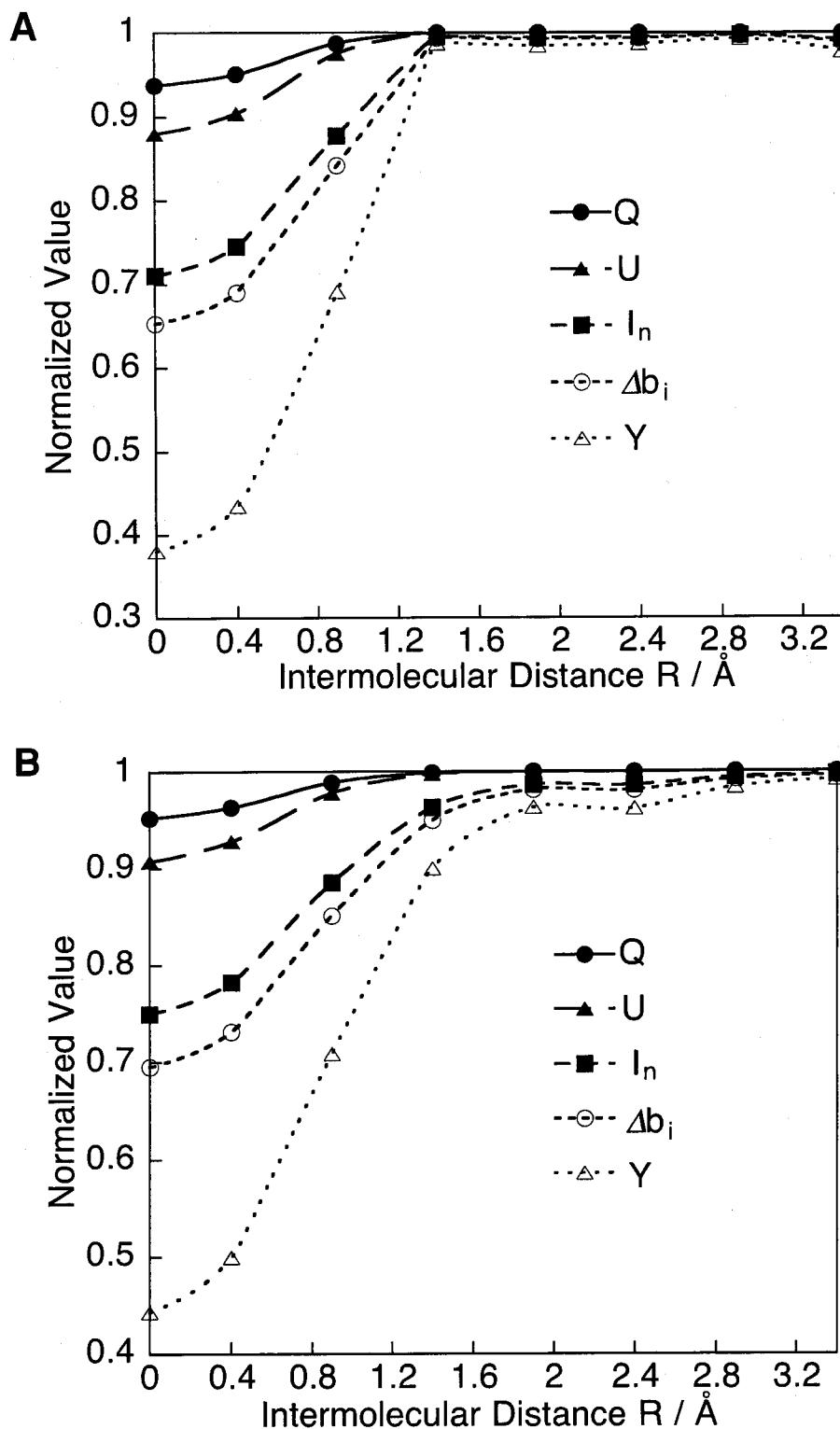
Figure 2.14. The variation of chemical indices at the LS state of **1a_O2** (**A**) and **1b_O2** (**B**) by UB2LYP in the region from R = 0.0 to 3.4 Å.
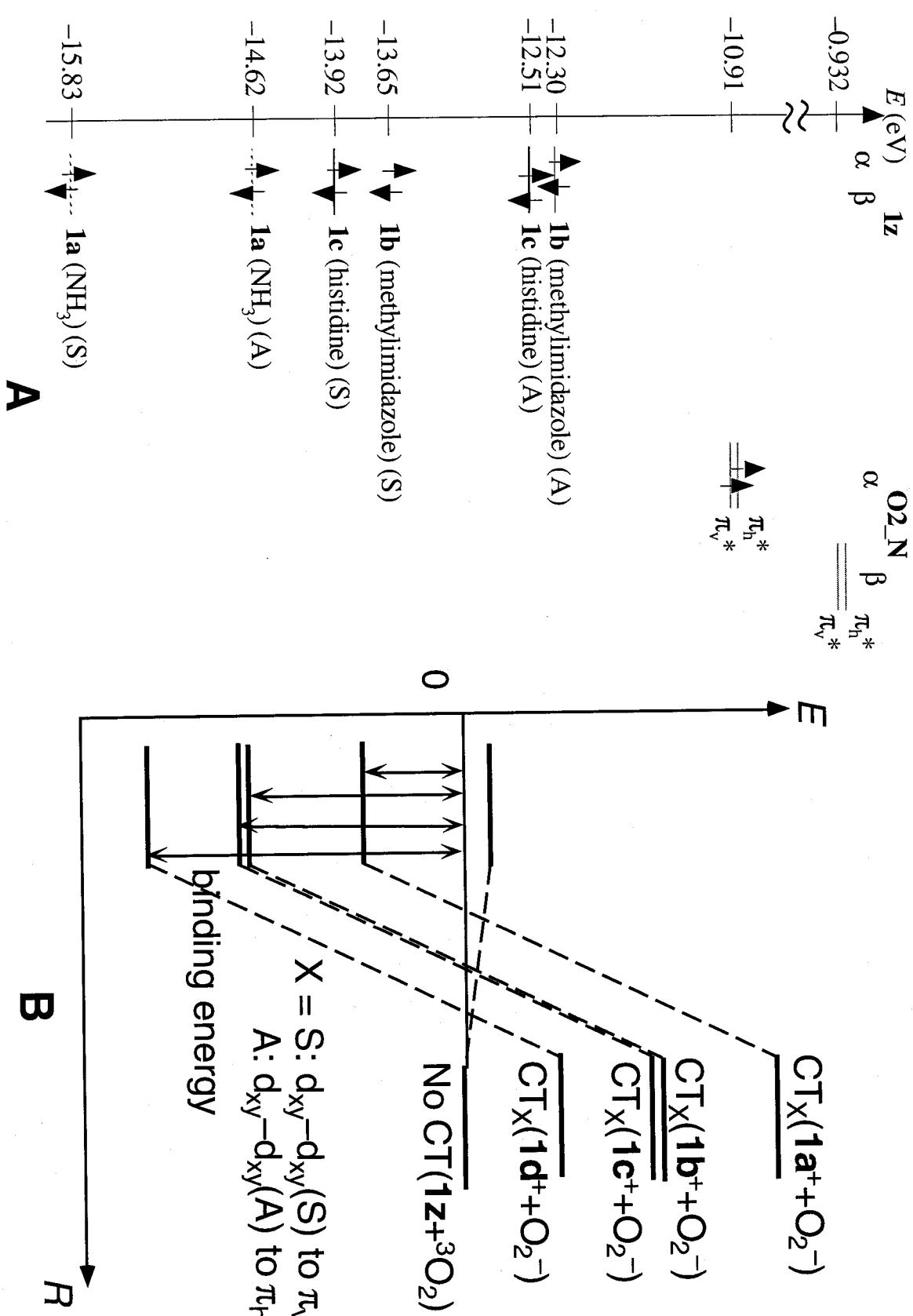
Figure 2.15. Orbital energy diagrams of symmetrical and antisymmetrical $d_{xy} \pm d_{xy}$ orbitals of **1z** ($z = a$–c) and π_h^* and π_v^* orbitals of dioxygen by UB2LYP results (A) and configuration energy diagrams by the Mulliken CT theory (B).

Part III

Chapter 3

Magnetic and Electronic Structures of the Active Sites in Oxygenated and Deoxygenated Hemerythrin: A Hybrid DFT Approach for Biomolecular Magnetism

3.1 Introduction

Hemerythrin (Hr) [3] is one of the major metalloproteins capable of reversibly binding dioxygen and found in animals of several marine invertebrates including *Sipunculida, Priapulida* and *Brachiopoda*. Past decades, it has been extensively studied from experimental aspects [48–51]. The two physiologically relevant forms of Hr are the deoxygenated (deoxyHr) and oxygenated (oxyHr) states. Crystallographic [48] and spectroscopic [49, 50] studies of deoxyHr have shown that the active site consists of two ferrous ions, Fe(II), that are bridged by two carboxylate ions and a μ-OH ligand. The coordination spheres of the two irons are completed by five histidine-N ligands, three binding to the six-coordinate (Fe1) and two to the five-coordinate (Fe2) metal centers. In deoxyHr, the magnetic coupling constant (J_{ab}) was determined -13 cm^{-1} as would be expected for a μ-OH bridge. In the reaction of deoxyHr with dioxygen, two electrons from Fe(II)–Fe(II) center and the proton from the bridging μ-OH group are transferred to O$_2$ binding to Fe2, yielding the μ-oxo-bridged diferric site, Fe(III)–Fe(III) of oxyHr possessing a terminal hydroperoxide. The presence of a μ-oxo bridge at the active site of oxyHr gives rise to a strong antiferromagnetic coupling between the two ferric centers, $J_{ab} = -77$ cm^{-1}.

Synthetic models [52–55] shed light to the electronic structure of the binuclear iron site in Hr. Lippard and co-workers synthesized Fe$_2$(μ-O)(μ-O$_2$CCH$_3$)$_2$(HBpz$_3$)$_2$ (HBpz$_3$ = hydrotris{3,5-diisopropyl-pyrazolyl}borate) [52] (**Figure 3.1 A**), which is a model of the azidomet Hr. The structural and spectroscopic data of the complex were in agreement with those of binuclear iron active site of oxyHr. The coupling constant of this complex between the two ferric centers was determined $J_{ab} = -121$ cm^{-1}, showing an antiferromagnetic interaction. For deoxyHr, Fe(μ-OH)(μ-O$_2$CCH$_3$)$_2$(Me$_3$-TACN)$_2$ (Me$_3$TACN = N',N'',N'''-trimethyltriazacyclononane) [53] (**Figure 3.1 B**) was synthesized, and its electronic structure was investigated experimentally. The magnetic coupling constant was found to be -13 cm^{-1}.

Recently, Brunold and Solomon investigated the electronic structure of deoxyHr and oxyHr by SQUID susceptibility experiment and evaluated the effective exchange interaction (J_{ab}) for Hr model, (NH$_3$)$_3$Fe(μ-OH)(η^2-HCOO)$_2$Fe(NH$_3$)$_2$ and (NH$_3$)$_3$Fe(μ-O)(η^2-

HCOO)$_2$Fe(OOH) (NH$_3$)$_2$ by density functional (DFT) calculations employing the local density approximation of Vosko, Wilk and Nusair and the nonlocal gradient corrections of Becke and Perdew [51].   However, the estimated $|J_{ab}|$ values for these simple models failed to reproduce the experimental results for both oxy and deoxyHr [50, 51].   Since the magnetic interaction concerns the electronic structure such as chemical bonds, it is important to employ the appropriate methods which estimate the magnetic coupling exactly in order to elucidate the dioxygen binding process.   Moreover, several enzymes involve transition metal clusters in their active sites, whose magnetic behaviors have been investigated by many experimental techniques.   Probably, reliable ab initio calculations of the J_{ab} values would contribute to the significant development of theoretical understanding of these active sites.   Such efforts may open an interdisciplinary field between molecular magnetism and biochemistry: biomolecular magnetism.

In this chapter, the author has performed the UHF and UDFT calculations (UB2LYP, UB3LYP and UBLYP) for the diferric complexes (**1**) as models of oxyHr and the diferrous complexes (**2**) as models of deoxyHr.   The calculated results have been discussed in order to elucidate the origin of the antiferromagnetic interaction and determine the appropriate methods to investigate the chemical bond nature of Hr.   As illustrated in **Figure 3.2**, the active site structures of the models of deoxyHr and oxyHr were approximated by the simplest (**a**) and the realistic (**b**) models.   In **a**, formates (HCOO) and NH$_3$ are utilized as glutamic (Glu) and aspartic (Asp) acids and histidines.   In **b**, acetates (CH$_3$COO) replace Glu and Asp, and Me-Im ligands replace histidines.   The author has examined the magnetic interaction and the chemical bonding nature of **1z** with oxygen (**1z_O2**) and **2z** (**z = a** and **b**) from the viewpoint of the effective exchange integrals (J_{ab}), the shape and symmetry of natural orbitals, and the charge and spin density distributions.   The SE interaction via μ-hydroxo bridge leads to the weak antiferromagnetic interaction between the two ferric ions in deoxyHr.   On the other hand, the σ- and π-type SE interactions via μ-O bridging atom result in the antiferromagnetic couplings between the two ferrous ions in oxyHr.   The author has also found that UB2LYP exchange-correlation functionals can be regarded as a reliable method to investigate the magnetic coupling for oxy and deoxyHr.   Chemical indices estimated by

UHF and UDFT calculations enable us to obtain the information into the nature of the chemical bond of the active site in Hr.   Judging from chemical indices, the difference of chemical bond nature was line with the fact that the magnetic coupling for the models of oxyHr is stronger than that for deoxy one.   OxyHr shows a weak chemical bond in the active core, leading to the reversible dioxygen trapping.   This means that magnetism is one of the useful criterion for understanding the nature of the active sites.   The author has investigated the dioxygen association in deoxyHr, utilizing Mulliken charge transfer (CT) theory.   The UB2LYP results were also consistent with the stepwise mechanism for oxygen trapping of deoxyHr.

3.2 Ab initio calculation

3.2.1 Orbital interaction

Molecular orbital (MO) pictures seem to be suitable for qualitative understanding of the magnetic interaction and the electronic structure for model **1z_O2** and **2z**.   To make an MO-theoretical explanation, let us consider the orbital interaction for **1z_O2** and **2z** on the basis of orbital symmetry rule.   Two d_i ($i = z^2$, zx, yz, x^2-y^2 and xy) atomic orbitals (AOs) interact each other symmetrically (S) and antisymmetrically (A), and form bonding and antibonding MOs.   These bonding and antibonding MOs of Fe ions interact with p AOs of bridging ligands.   The symmetry allowed orbital interactions are to be considered as shown in **Figures 3.3** and **3.4**.   The σ-type singly occupied MOs (SOMOs) are bonding MO of 3dσ (S) MO ($d_{z^2}+d_{z^2}$) of Fe ions and vacant 3s (S) orbital of μ-oxo or μ-OH group and antibonding one of 3dσ (A) MO ($d_{z^2}-d_{z^2}$) and filled 2p (A) orbital (**Figure 3.3 A**).   The π-type SOMOs are given by antibonding MO of 3dπ (A) MO ($d_{xz}-d_{xz}$) and filled 2p (A) orbital and that of 3dπ (S) MO ($d_{xz}+d_{xz}$) and filled 2p (S) orbital (**Figure 3.3 B**), where S-type orbitals interact each other stronger than A-type ones do.   The $\pi_\perp$-type SOMOs are presented by only 3d$\pi_\perp$ (A) MO ($d_{yz}-d_{yz}$) and antibonding MO of 3d$\pi_\perp$ (S) MO ($d_{yz}+d_{yz}$) and filled 2p (S) orbital (**Figure 3.4 C**).   The δ-type SOMOs are expressed by antibonding MO of 3dδ (S)

MO $(d_{x^2-y^2}+d_{x^2-y^2})$ and filled S-type orbitals of bridging acetate groups and only $3d\delta$ (A) MO $(d_{x^2-y^2}-d_{x^2-y^2})$ (**Figure 3.4 D**). The $\delta_\perp$-type SOMOs are provided by $3d\delta_\perp$ (S) MO $(d_{xy}+d_{xy})$ and $3d\delta_\perp$ (A) MO $(d_{xy}-d_{xy})$ because of no $\delta_\perp$-type orbital interaction between Fe ions and bridging ligands (**Figure 3.4 E**).

In **1z_O2**, two high-spin Fe(III) ions show all types of orbital interactions via orbitals of bridging ligands. On the other hand, two high-spin Fe(II) ions of **2z** indicate σ-, π-, $\pi_\perp$- and δ-type orbital interactions. The strength of these interactions is in order; $\sigma > \pi \cong \pi_\perp > \delta \cong \delta_\perp$. Judging from this trend, the σ- and π-type superexchange (SE) interactions cause the antiferromagnetic couplings for **1z_O2** and **2z**. The δ-type SE interaction also contributes the antiferromagnetic interaction slightly.

3.2.2 Calculation procedure

The UHF and hybrid DFT (UB2LYP, UB3LYP) and pure DFT (UBLYP) calculations were performed with the Tatewaki–Huzinaga MIDI (533(21)/53(21)/(41)) [39] plus Hay's d diffuse function ($\alpha = 0.1215$) [40] for Fe atoms, Pople's 6-31G* [41] for C, O and N atoms and 6-31G [42] for H atoms.

The location of H4 atom was determined by partial optimization in **1z_O2**. Since these models were too large to fully optimize the geometries in our computer systems, other parameters were fixed. However, the calculated results for these models should represent a significant advancement with respect to the magnetic interaction for both oxy and deoxyHr. Other geometrical parameters for **1z_O2** and **2z** were taken from X-ray crystallographic studies [48, 49]. The author chose the simplest model, $(NH_3)_3Fe(\mu\text{-}HOOC)_2Fe(NH_3)_2$ (**a**), and the realistic model, $(Me\text{-}Im)_3Fe(\mu\text{-}H_3COOC)_2Fe(Me\text{-}Im)_2$ (**b**), with the Fe–Fe core in oxy Hr (**1**) and deoxyHr (**2**) in order to elucidate the ligand coordination effects as shown in **Figure 3.2**. The author calculated the J_{ab} values of **1z_O2** and **2z** using several computational schemes, eqs. (12a)–(12c), to estimate the magnitude of magnetic interactions and determined the NOs, their occupation numbers using eq. (15) and normalized chemical indices with eqs. (24a)–(24d).

3.3 Magnetic Interaction for 1_O2 and 2

3.3.1 Effective exchange integrals

To estimate the magnitude of the magnetic interaction for **1z_O2** and **2z**, the author has calculated the J_{ab} values. **Table 3.1** summarizes the J_{ab} values for **1z_O2** and **2z** by eqs. (12a)–(12c). All the calculated J_{ab} values were negative, showing antiferromagnetic interactions between the Fe ions. These results were qualitatively consistent with the experiment [48–51]. The UHF underestimated the absolute values of the J_{ab} for **1z_O2** and **2z**, while the UBLYP overestimated them as compared with the experimental values (–77 cm^{-1} for **1_O2** and –13 cm^{-1} for **2**). Solomon's calculation [51] estimated too large $|J_{ab}|$ values ($J_{ab} = -214$ cm^{-1}) as well as our UBLYP results, indicating that pure DFT tends to estimate the absolute values of J_{ab} much larger than experimental one. On the other hand, for **1z_O2** and **2z**, UB2LYP and UB3LYP calculations reproduce the experimental value quantitatively. The hybrid methods, especially UB2LYP exchange-correlation functionals, are desirable for more reliable $J_{ab}^{(3)}$ values between models **a** and **b** was 20–100 cm^{-1} for **1z_O2**, indicating that the difference of ligand substitution is sensitive to the magnetic interaction.

As for UHF, UB2LYP, UB3LYP and UBLYP calculations, the $J_{ab}^{(3)}$ values by our approximate spin projection (AP) procedure were close to $J_{ab}^{(1)}$ for **1z_O2** and almost same for **2z**. The absolute values of calculated J_{ab} were in order; $|J_{ab}^{(2)}| < |J_{ab}^{(3)}| \leq |J_{ab}^{(1)}|$. This result indicates that **1z_O2** and **2z** belong to the weak-overlap and the no-overlap regions, respectively. This apparently indicates that comparisons of $J_{ab}^{(i)}$ ($i = 1$–3) are promising for elucidating the orbital overlap effect in the SE interaction.

3.3.2 Natural orbitals and occupation numbers

The bonding and antibonding singly occupied natural orbitals (SONOs) and their occupation numbers by UHF and hybrid DFT are expected to clarify the mechanism of the magnetic interaction for **1b_O2** and **2b**. **Table 3.2** summarizes the occupation numbers of

HOMO, SONOs and LUMO for these species. The UHF underestimates the strength of the $\sigma(\pi)$-bonding, while UBLYP overestimates it. This is reason why UHF and UBLYP underestimate and overestimate $|J_{ab}|$ values, respectively. Judging from the fact that the calculated J_{ab} values are close to the experiments, UB2LYP is found to be a reliable method for investigation of the nature of chemical bonds in these species. **Figure 3.5** illustrates the SONOs of **1b_O2** in LS state by UB2LYP calculation. It is found that SONO±5 shows the σ-type (dσ–pσ) interaction, that SONO±4 and SONO±3 illustrate the π-type (dπ–pπ) ones, and that SONO±2 and SONO±1 show the δ-type ones as illustrated in **Figures 3.3** and **3.4**. We can observe that the NOs are delocalized on the Fe(μ-O)Fe site at the UB2LYP level. The delocalized orbitals can be explained by the σ- and π-type antiferromagnetic SE interactions between the Fe ions. These results make it clear that the SE interaction via dioxygen is responsible for the strong antiferromagnetic interaction between the two ferric ions of **1b_O2**.

On the other hand, for **2z** it is found in **Figure 4.6** that SONO±4 shows the σ-type coupling, SONO±3 and SONO±2 illustrate the π-type ones, and SONO±1 shows the δ-type one as illustrated in **Figure 4.6**. The SONOs are found to be delocalized on the Fe(μ-OH)Fe site at the UB2LYP level, leading to the antiferromagnetic SE interaction between the Fe ions. These results show that the SE interaction via dioxygen is responsible for the antiferromagnetic interaction between the two Fe ions of **2b**.

3.3.3 Charge and spin density populations

The author has investigated the charge and spin density distributions for **1z_O2** and **2z** to elucidate the characteristics of the charge transfers among Fe(III) (or Fe(II)), O^{2-} (or OH⁻) and ligands. As listed in **Table 3.3**, the charge density on O3 site of **1z_O2** varies from formal charge (−2.0) to approximately −1.0, and that on hydroxide group (O3H4) of **2z** changes from formal charge (−1.0) to about −0.5, indicating the charge density transfers to Fe ions for both models. The back charge transfer implies that SE interaction is responsible for the antiferromagnetic coupling of Hr. The ligands regulate the back charge transfer from oxo or hydroxide group to the Fe–Fe core, namely delocalization of charge transfer on the

135

active site.   The magnitudes of charge transfer from the ligands to the active cores of **1z_O2**

or **2z** increase in order: UHF (1.042) < UB2LYP (1.718) < UB3LYP (2.082) < UBLYP

(2.400), showing the same tendency as the decrease of charge density on O3 site from formal

charge (–2.0).   It follows that the charge densities are more delocalized over the whole

molecule, as the ratio of the HF exchange functional decreases in order: UHF (100%) >

UB2LYP (50%) > UB3LYP (20%) > UBLYP (0%).   On the other hand, the charge densities

of OOH part (O5 + O6 + H4) of **1z_O2** are approximately –1.0, showing that charge densities

of the active site are transferred to the O5 and O6 sites when dioxygen is bound to the active

core of **1** and proton in the active core move to dioxygen.

The spin densities are delocalized over the Fe(μ-O)Fe and Fe(μ-OH)Fe sites, while the

populations by the UHF calculation are localized at the Fe sites.   The localized spin densities

by UHF tend to underestimate the magnitude of J_{ab} value for **1_O2** and **2**.   The spin densities

on O3 site of **1_O2** and O3H4 site of **2** are so small that spin polarization (SP) effects do not

influence the magnetic interaction of Hr.   On the other hand, the spin densities of O5 and O6

of **1** become about 0.0.   Judging from charge and spin densities, it is found that the dioxygen

takes two electrons and one proton and changes hydroperoxide ion, OOH⁻.

3.4 Chemical Bond Nature

3.4.1 Effective bond order

Effective bond order b estimated from the occupation numbers of SONOs in **Table 3.2**

with eq. (19) was about 0.23 (σ), 0.17 (π), 0.14 ($\pi_\perp$), 0.02 (δ) and 0.01 ($\delta_\perp$) for **1b_O2** and

0.06 (σ), 0.03 (π), 0.02 ($\pi_\perp$) and 0.01 (δ) for **2b** by UB2LYP, respectively.   The d-p

interaction of the active site became larger as $\sigma > \pi \gg \delta$, indicating that the σ and π-type SE

interactions mainly contribute to the magnetic coupling of **1b_O2** and **2b**.   The b values of

1b_O2 were much larger than those of **2b**, showing the same tendency of J_{ab} values.   This

implies that σ and π-type SE interactions of **2b** are much smaller than those of **1b_O2**,

resulting in the small magnitude of J_{ab} value of **2b**.   On the other hand, the occupation

numbers of HOMO and LUMO were 1.997 and 0.003 for **1b_O2** and 1.998 and 0.002 for **2b** by UB2LYP, respectively. This shows the very weak SP effect under the UB2LYP approximation. On the other hand, the occupation numbers of HOMO and LUMO in models **a** and **b** are close each other, indicating that SP effect is much smaller than SE interaction. The NO analysis and effective bond order clearly demonstrate that the origin of the antiferromagnetic exchange interaction of oxy and deoxyHr is the σ and π-type SE interactions via weak Fe–O or Fe–OH conjugation.

3.4.2 Other chemical indices

Since magnetic couplings are substantially related to the chemical bonding nature, the author has discussed the characteristics of the chemical bond in both oxy and deoxyHr. Spin density index (Q), unpaired electron density (U), decrease of bond order ($\Delta b = 1 - b$), information entropy (I) and diradical character (Y) should be useful indices for the investigation of bond character. Using the occupation numbers of SONOs, these indices can be estimated with eqs. (24a)–(24d). General tendencies of these chemical indices for the active site of **1z_O2** and **2z** were in the following order:

$$Y < \Delta b \cong I < U < Q. \tag{27}$$

In **Tables 3.4** and **3.5**, the large Q values, namely spin density indices, show that the electron pair remains to be splitting because of the electron correlation (EC) effect. We can find the similar behavior for the U values, which are equivalent to the deviation for exact singlet value $^{LS}\langle S^2 \rangle = 0$ for the BS solution, indicating that the electron localization via the EC effect is significant for **1z_O2** and **2z**. On the other hand, the Y values, which characterize the double excitation of electrons occupying bonding NOs, imply that the electrons occupying SONO partially can delocalize between spin sites. The I and Δb values express the character of chemical bonds and exhibit intermediate behaviors between Q and Y values. Therefore, they could be regarded as useful indices to diagnose the bond nature and the measures of the strength of orbital interaction. Judging from these chemical indices,

1z_O2 belongs to the rather weak orbital interaction region. However, this weak bond character is sufficient for the cooperative intramolecular (through-bond) charge transport for the proton migration step of oxygen trapping (see below), namely the reversible dioxygen binding in Hr. On the other hand, **2z** belongs to the very weak orbital interaction region, showing a small antiferromagnetic coupling.

In **Table 3.4**, the chemical indices for **1z_O2** show a following relation in term with the orbital type; $\sigma < \pi < \delta$. All the δ-type chemical indices were almost 1.0, showing that δ-type orbital interactions between Fe(III) ions via bridging acetate ligands are very small. These results indicate that δ-type SE interaction hardly contributes to the magnetic coupling. On the other hand, the σ-type chemical indices reduced from 1.0, implying that σ-type orbitals of ferric ions interact each other via bridging μ-O ligands much stronger than δ-type orbitals. The π-type chemical indices show the intermediate bonding character between σ- and δ-type ones. Judging from these results, σ- and π-type SE interactions are mainly attributable to the antiferromagnetic couplings. On the other hand, the σ-, π- and δ-type chemical indices for **2z** were almost 1.0. It shows that orbital interactions between Fe(II) ions via bridging μ-OH and acetate ligands are very small, resulting in a weak antiferromagnetic SE interaction for **2z**.

The chemical indices also provide information with respect to computational methods. These values estimated by UHF were almost 1.0, indicating that up and down spins are localized on each Fe ion. In other words, two Fe ions dissociate each other even via bridging ligands. In UBLYP calculation, these values show that σ- and π-type unpaired electrons are delocalized on whole active site, implying strong covalent σ- and π-type bonds. The UBLYP apparently overestimates these bonds. The indices evaluated by both UB2LYP and UB3LYP calculations give intermediate bond character between those by UHF and UBLYP. Although, the σ-bond character by UB2LYP is close to that by UHF, while that character by UB3LYP is similar to that by UBLYP. The difference of the σ-bond character would contributes that of the magnetic interaction. The electron delocalization and correlation are competitive in the iron–oxygen cluster in oxy and deoxyHr. This is the reason why we need to use UB2LYP instead of UB3LYP and UBLYP; it is noteworthy that UB2LYP works well in strongly correlated electron systems.

138

3.5 Charge Transfer Mechanism for Dioxygen Trapping

3.5.1 One-electron transfer step

As shown in previous chapter, charge-transfer (CT) interactions between metal cluster and triplet molecular oxygen ($^3O_2$) play important roles in $^3O_2$-trapping in oxyHc. The orbital energy levels obtained by the hybrid DFT calculations were successfully utilized to depict CT excitation energy diagrams and possible potential curves. Here, using the orbital energy of Fe in **2z** and dioxygen, the author discusses the mechanism of dioxygen binding of Hr qualitatively. When dioxygen becomes close to the active core of Hr, it is bound to the Fe2 site of Hr. The orbital energy of MOs corresponding to d_i ($i = z^2$, zx, yz, x^2-y^2 and xy) orbital in Fe2 and π and $\pi_\perp$ orbitals in O_2 are shown in **Figure 3.7 A**. From **Figure 3.7 A**, these large energy gaps between α- and β-MOs corresponding to dxy orbitals are ascribed to the different coordination number and the strong electron correlation (EC) effects on Fe ions. This indicates that stepwise dioxygen binding to **2z** occurs as illustrated in **Figure 3.8 A** and that the use of reliable methods involving EC effects is crucial even for qualitative studies of the electron-transfer process. In fact, UB2LYP indicates that only α orbital energies corresponding to d_{xy} orbital in both models **a** (–9.82 eV) and **b** (–8.27 eV) are the closest to that of the $\pi_\perp^*$ orbitals in O_2 (–0.93 eV), indicating that d_{xy} orbital of Fe2 interacts with $\pi_\perp^*$ orbitals of O_2 when dioxygen approaches to the active site of Hr. The CT should occur from dxy orbital of Fe2 to $\pi_\perp^*$ orbital of O_2 when dioxygen is bound to Fe2 site in Hr, resulting in mixed valence (MV) Fe1(II)–Fe2(III) core and O_2^- anion (Step 1 as shown in **Figure 3.8 A**).

From above results, in Step 1 of dioxygen binding process in Hr, ligand coordination effects are influential to the orbital energies as well as that of Hc. The orbital energies corresponding to d_i orbitals of model **a** were smaller than those of model **b**. As described above, the highest α orbital energies corresponding to d_{xy} orbital in model **a** (–9.82 eV) were smaller than that of $\pi_\perp^*$ orbital of dioxygen (–0.932 eV), as shown in **Figure 3.7 A**, indicating that dxy orbital of Fe2 interacts with $\pi_\perp^*$ orbitals of dioxygen weakly. In other words, the

139

CT excitation energy from d_{xy} type MOs of **2a** to $\pi_\perp^*$ orbital of O_2 to afford the CT (**2a$^+$**O_2^-) state is large and the stabilization energy by the configuration mixing between CT (**2a$^+$**O_2^-) and no CT (**2a**+O_2) is small. While, the highest α orbital energy corresponding to d_{xy} orbital in model **b** (-8.27 eV) was closer to that of $\pi_\perp^*$ orbital of dioxygen than that for **2a**, showing that the interaction between d_{xy} and $\pi_\perp^*$ orbital in the model **b** is stronger than that in the model **a**. The CT excitation energies become smaller in these complexes as illustrated in **Figure 3.7 B**, indicating the strong configuration mixing. Such strong CT interaction between **2b** and dioxygen is ascribed to the origin of the smaller activation barrier of **2b**+O_2 than that of **2a**+O_2 as shown in **Figure 3.7 B**.

3.5.2 Spin inversion and oxygen activation

As shown in **Figure 3.7 B**, the spin state of the initial complex between **2z** and $^3O_2$ should be triplet because the ground state of **2z** is singlet, indicating that the spin inversion from the triplet to the singlet state occurs to afford a singlet **2z**–O_2 complex. From **Figure 3.7 B**, the initially formed CT complex between the MV [Fe(II)–Fe(III)] core and $O_2^{-\bullet}$ is triplet, but the energy gap between the triplet and singlet CT complexes would become smaller than that between no CT complexes (**2z**+$^1O_2$ and **2z**+$^3O_2$) because the complexes are consisted of magnetically coupled species. This implies the facile spin inversion from the triplet to the singlet state within the CT complex: $\{^2[\text{Fe(II)}-\text{Fe(III)}]\bullet^2[O_2^-]\}$. Probably, the protein dynamics play an important role in the process especially Step 2 with respect to the cooperative proton and electron transfer (PET) reaction as illustrated in **Figure 3.8 A**.

However, judging from the CT excitation energies, these ligand coordination effects will influence the protein function . For example, the geometric structures of the active cores in methane monooxygenase (MMO) and ribonucleotide reductase (RNR) are similar to that of Hr, although these function, in which MMO catalyzes the conversion of methane to methanol and RNR catalyzes the reduction of ribonucleotides to their corresponding deoxyribonucleotide, are different from that of Hr. The oxygenase and reductase function of MMO and RNR may be attributable to the non-bridging carboxylate ligands utilized instead of imidazole ones. Electron donating character of carboxylate is stronger than that of

imidazole, leading to the rise of the orbital energy corresponding to Fe site nearby the π^* or σ^* orbitals of O_2.   This strong electron donation would result in the breaking O–O bond and oxygen activation.   If we can change the coordination ligands from $HBpz_3$ to the more electron-donating ligands as shown in **Figure 3.1 C**, the complex may show oxygenase function.   Further studies on this point are in progress.

3.6 Discussion and Concluding Remarks

3.6.1 Chemical indices

Chemical indices have been utilized to understand the nature of chemical bonds in the active sites of oxy and deoxyHr.   In order to investigate the bond nature, we need to perform the symmetry-adapted (SA) CASCI and CASSCF for them.   However, these systems are too large to carry out such calculations.   The author estimates the chemical indices, which can also be defined by CASCI and CASSCF calculations, using the occupation numbers of UNO and DNO obtained by the broken-symmetry (BS) calculations.   The evaluated results provide a lot of information into the chemical bond of the Fe–Fe active core, e.g. the magnitude of electron localization at Fe sites and the double excitation of electrons occupying bonding NOs.   Moreover, these indices help us to understand the origin of the magnetic couplings in oxy and deoxyHr and the difference of the magnitude of the coupling constants. These results imply that the chemical indices are useful for the elucidation of the magnetic interaction and the bonding nature in metal clusters in biology.   Since chemical bond nature is strongly related to active control of the reaction in enzymes and proteins, the investigation of the chemical indices and the magnetic interaction can be utilized as the probe to shed light on the elucidation of their functions.   In this sense, an intersection area between molecular magnetism and biochemistry, i.e., biomolecular magnetism, is promising.

3.6.2 One- or two-step mechanism for oxygen trapping

Both one- and two-step mechanisms were proposed to explain the dioxygen trapping

141

process in Hr on the basis of the experimental grounds as illustrated in **Figure 3.8**. A mechanism presented by Howard and Rees [56] consists of two-step one-electron transfers bracketing proton transfer from the metal center to the dioxygen as illustrated in **Figure 3.8 A** (two-step mechanism). Que and True [57] proposed a mechanism with proton transfer following a concerted two-electron transfer as shown in **Figure 3.8 B** (one-step mechanism). In this chapter, the α orbital energies of d_{xy} orbital in Fe1 and Fe2 of **2b** were -12.02 and -8.27 eV, respectively, because of the difference of the coordination number to Fe ions, showing that simultaneous two-electron transfer was difficult in **2b** and dioxygen. This result supports the two-step mechanism proposed by Howard and Rees as shown in **Figure 3.8**. The two-step CT mechanism indicates that the spin inversion from the triplet to the singlet state occurs at the Step 1, namely one-electron transfer step, and the next cooperative PET step (Step 2) takes place without spin inversion. However, to confirm this proposal, it is necessary to analyze the potential energy surface and the variation of charge and spin densities in the dioxygen binding process of deoxyHr in detail.

The author has found that hybrid DFT with our approximately spin projected (AP) scheme is a reliable procedure to investigate the electronic structure of oxy and deoxy Hr. The AP scheme is also applicable to BS solutions, for which the orbital overlaps (T_i) between magnetic orbitals are not negligible. The total energy of the LS state is given by the AP scheme as eq. (14). This equation removes the major part of the spin contamination errors, being applicable to depict potential curves smoothly, In fact, eq. (14) works well in the whole region of dissociation processes of covalent bonds since the AP-LS energy reduces to LS energy of the closed-shell state at the instability threshold $T_i = 1$. The AP scheme would be applicable to investigation of the PET step.

3.6.3 Concluding remarks

The author has performed UHF and UDFT calculations for models **1** and **2** to investigate the magnetic interaction and chemical bonding nature of oxy and deoxyHr. The conclusions are as follows: (i) the σ- and π-type superexchange (SE) interactions via μ-hydroxo bridge account for the weak antiferromagnetic interaction between the two ferrous

ions of deoxyhemerythrin, (ii) the σ- and π-type SE interaction via μ-oxo bridging atom is responsible for the antiferromagnetic coupling between the two ferric ions of oxyhemerythrin, (iii) the difference of the magnitude of the magnetic couplings between oxy and deoxyHr is ascribed to the strength of dσ-pσ and dπ-pπ interaction of the active core; (iv) hybrid DFT, especially UB2LYP, can reproduce the experimental value quantitatively and UB2LYP can be regarded as a reliable method for the investigation of the magnetic coupling constant of both oxy and deoxyHr, and (v) hybrid DFT calculations followed by chemical bonding analyses are applicable to other binuclear transition metal complexes involving in enzymes [46, 47].

Table 3.1. Effective exchange interactions $(J_{ab})^a$ calculated for the models of oxy and deoxyHr

Model	Method	$J_{ab}^{(1)}$	$J_{ab}^{(2)}$	$J_{ab}^{(3)}$
1a_O2[b]	UHF	−15.04	−12.53	−15.02
	UB2LYP	−53.47	−44.56	−53.19
	UB3LYP	−95.07	−79.22	−92.38
	UBLYP	−383.4	−319.5	−367.1
1b_O2[b]	UHF	−30.51	−25.43	−30.46
	UB2LYP	−51.14	−42.62	−50.91
	UB3LYP	−108.9	−90.77	−105.7
	UBLYP	−242.9	−202.4	−230.8
2a[c]	UHF	−3.329	−2.663	−3.329
	UB2LYP	−11.04	−8.834	−11.04
	UB3LYP	−24.26	−19.41	−24.23
	UBLYP	−8.334	−6.669	−8.277
2b[c]	UHF	−3.544	−2.835	−3.544
	UB2LYP	−10.27	−8.214	−10.26
	UB3LYP	−22.88	−18.30	−22.85
	UBLYP	−26.09	−20.87	−25.89

$^a J_{ab}$ are shown in cm^{-1}. $^b J_{ab}$(exp.) = −77 cm^{-1} for oxyhemerythrin.

$^c J_{ab}$(exp.) = −13 cm^{-1} for deoxyhemerythrin.

Table 3.2.   Occupation numbers[a] of HOMO, SONOs of **1z_O2** and **2z** (**z** = **a** and **b**) by the UHF and UDFT calculations in the LS state

method	model	HOMO	SONO–5	SONO–4	SONO–3	SONO–2	SONO–1
UHF	**1a_O2**	1.998	1.102	1.070	1.061	1.006	1.004
	1b_O2	1.997	1.113	1.073	1.064	1.006	1.003
	2a	1.997		1.031	1.019	1.011	1.003
	2b	1.997		1.030	1.018	1.011	1.002
UB2LYP	**1a_O2**	1.997	1.238	1.183	1.156	1.018	1.003
	1b_O2	1.997	1.226	1.165	1.143	1.016	1.01
	2a	1.998		1.063	1.038	1.023	1.007
	2b	1.998		1.063	1.037	1.022	1.005
UB3LYP	**1a_O2**	1.996	1.783	1.257	1.19	1.035	1.021
	1b_O2	1.997	1.746	1.389	1.201	1.081	1.032
	2a	1.998		1.121	1.076	1.043	1.015
	2b	1.997		1.120	1.073	1.043	1.012
UBLYP	**1a_O2**	1.998	1.860	1.464	1.367	1.093	1.048
	1b_O2	1.997	1.797	1.641	1.414	1.274	1.114
	2a	1.998		1.252	1.194	1.098	1.035
	2b	1.996		1.264	1.183	1.093	1.026

[a]n(SONO–p)+ n(SONO+p) = 2.0 and n(HOMO) + n(LUMO) = 2.0.

Table 3.3. Charge densities and spin densities of for the models of oxy and deoxyHr in the LS state

model	Methods		Fe1[a]	Fe2[a]	O3[a]	H4[a]	O5[a]	O6[a]
1a_O2	UHF	Charge	1.778	1.927	−1.275	0.489	−0.587	−0.600
		Spin	4.663	−4.599	−0.033	0.001	−0.077	−0.008
	UB2LYP	Charge	1.248	1.406	−0.964	0.457	−0.454	−0.523
		Spin	4.242	−4.214	0.090	0.000	−0.204	−0.016
	UB3LYP	Charge	0.876	1.023	−0.788	0.462	−0.400	−0.462
		Spin	3.854	−3.392	−0.020	0.001	−0.427	−0.106
	UBLYP	Charge	0.640	0.811	−0.693	0.442	−0.224	−0.360
		Spin	3.590	−3.013	−0.120	0.001	−0.418	−0.150
1b_O2	UHF	Charge	1.964	2.013	−1.302	0.508	−0.593	−0.632
		Spin	4.639	−4.559	−0.027	0.001	−0.111	−0.000
	UB2LYP	Charge	1.394	1.455	−1.007	0.471	−0.475	−0.556
		Spin	4.310	−4.226	0.026	0.000	−0.207	−0.001
	UB3LYP	Charge	0.931	1.119	−0.799	0.462	−0.345	−0.458
		Spin	3.764	−3.595	−0.288	0.086	0.059	−0.003
	UBLYP	Charge	0.649	0.856	−0.708	0.453	−0.265	−0.384
		Spin	3.251	−3.200	−0.273	0.131	−0.005	0.170
2a	UHF	Charge	1.517	1.494	−1.207	0.459		
		Spin	3.941	−3.906	−0.034	−0.004		
	UB2LYP	Charge	1.100	1.126	−1.043	0.436		
		Spin	3.850	−3.794	−0.060	−0.005		
	UB3LYP	Charge	0.827	0.874	−0.920	0.420		
		Spin	3.765	−3.684	−0.090	−0.006		
	UBLYP	Charge	0.591	0.664	−0.810	0.408		
		Spin	3.612	−3.509	−0.114	−0.008		
2b	UHF	Charge	1.387	1.450	−1.201	0.465		
		Spin	3.936	−3.905	−0.031	−0.004		
	UB2LYP	Charge	1.013	1.111	−1.038	0.446		
		Spin	3.844	−3.792	−0.053	−0.005		
	UB3LYP	Charge	0.765	0.874	−0.918	0.431		
		Spin	3.759	−3.682	−0.076	−0.006		
	UBLYP	Charge	0.540	0.671	−0.799	0.417		
		Spin	3.594	−3.501	−0.106	−0.009		

[a]The site numbers are shown in **Figure 3.1**.

Table 3.4. Chemical indices for σ, π, δ-type orbitals of **1z_O2** (**z** = **a** and **b**) by the UHF and UDFT calculations in the LS state

model	κ	method	$^{\kappa}Q_n$	$^{\kappa}U_n$	$^{\kappa}I_n$	$^{\kappa}\Delta b$	$^{\kappa}Y_n$
1a_O2	σ-type	UHF	0.995	0.990	0.923	0.898	0.798
		UB2LYP	0.971	0.943	0.809	0.762	0.549
		UB3LYP	0.621	0.386	0.256	0.217	0.029
		UBLYP	0.511	0.261	0.168	0.140	0.011
	π-type	UHF	0.998	0.996	0.951	0.934	0.869
		UB2LYP	0.985	0.971	0.868	0.831	0.671
		UB3LYP	0.974	0.949	0.822	0.777	0.576
		UBLYP	0.908	0.825	0.644	0.584	0.295
	δ-type	UHF	1.000	1.000	0.996	0.995	0.990
		UB2LYP	1.000	1.000	0.992	0.989	0.979
		UB3LYP	1.000	0.999	0.980	0.972	0.944
		UBLYP	0.997	0.995	0.947	0.929	0.860
1b_O2	σ-type	UHF	0.994	0.987	0.914	0.887	0.776
		UB2LYP	0.974	0.949	0.819	0.774	0.569
		UB3LYP	0.666	0.444	0.298	0.254	0.042
		UBLYP	0.604	0.364	0.240	0.203	0.025
	π-type	UHF	0.998	0.995	0.949	0.931	0.863
		UB2LYP	0.988	0.976	0.881	0.846	0.699
		UB3LYP	0.950	0.904	0.756	0.705	0.469
		UBLYP	0.839	0.709	0.531	0.473	0.193
	δ-type	UHF	1.000	1.000	0.997	0.995	0.991
		UB2LYP	1.000	1.000	0.991	0.987	0.974
		UB3LYP	0.998	0.996	0.958	0.943	0.887
		UBLYP	0.978	0.956	0.845	0.806	0.632

Table 3.5. Orbital overlap and chemical indices for σ, π, δ-type orbitals of **2z** (**z** = **a** and **b**) by the UHF and UDFT calculations in the LS state

| model	κ	method	$^\kappa Q_n$	$^\kappa U_n$	$^\kappa I_n$	$^\kappa \Delta b\, {}^\kappa Y_n$	
2a	σ-type	UHF	1.000	0.999	0.977	0.969	0.938
		UB2LYP	0.998	0.996	0.953	0.937	0.875
		UB3LYP	0.993	0.985	0.908	0.879	0.762
		UBLYP	0.968	0.937	0.797	0.748	0.526
	π-type	UHF	1.000	1.000	0.989	0.985	0.97
		UB2LYP	1.000	0.999	0.978	0.97	0.94
		UB3LYP	0.998	0.996	0.956	0.94	0.881
		UBLYP	0.988	0.976	0.886	0.854	0.716
	δ-type	UHF	1.000	1.000	0.998	0.997	0.995
		UB2LYP	1.000	1.000	0.995	0.993	0.986
		UB3LYP	1.000	1.000	0.989	0.985	0.97
		UBLYP	0.999	0.999	0.974	0.965	0.929
2b	σ-type	UHF	1.000	0.999	0.978	0.97	0.939
		UB2LYP	0.998	0.996	0.954	0.937	0.875
		UB3LYP	0.993	0.986	0.909	0.88	0.764
		UBLYP	0.964	0.93	0.786	0.736	0.506
	π-type	UHF	1.000	1.000	0.99	0.986	0.971
		UB2LYP	1.000	0.999	0.979	0.971	0.941
		UB3LYP	0.998	0.996	0.957	0.942	0.885
		UBLYP	0.989	0.979	0.893	0.862	0.73
	δ-type	UHF	1.000	1.000	0.999	0.998	0.996
		UB2LYP	1.000	1.000	0.996	0.995	0.99
		UB3LYP	1.000	1.000	0.992	0.988	0.977
		UBLYP	1.000	0.999	0.981	0.974	0.948

A

HB(pz)₃⁻

B

R=Me

MTACN

C
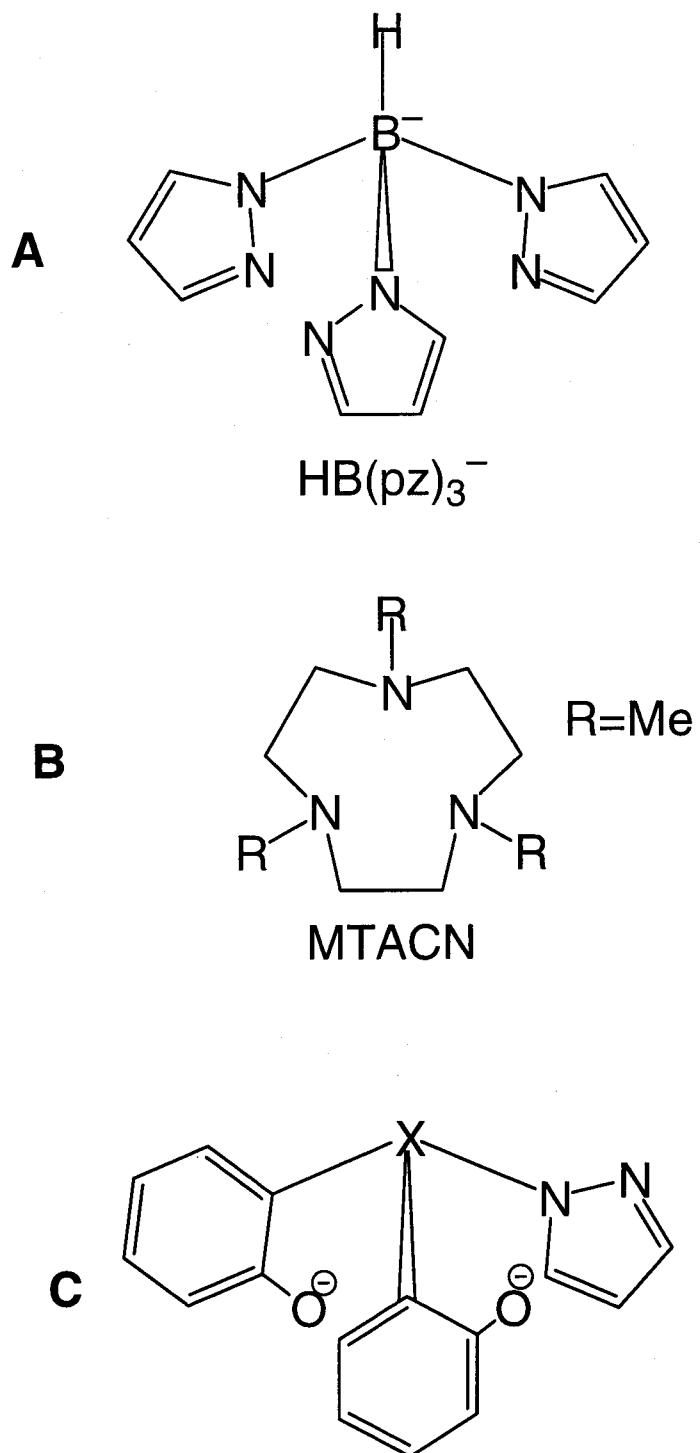
Figure 3.1 Coordination ligands utilized for the models of Hr; HBpz₃ (= hydrotris{3,5-diisopropyl-pyrazolyl}borate) (**A**) and Me₃TACN (= *N',N'',N'''*-trimethyltriazacyclononane) (**B**), and a proposed ligand for oxygen activation (**C**).

149
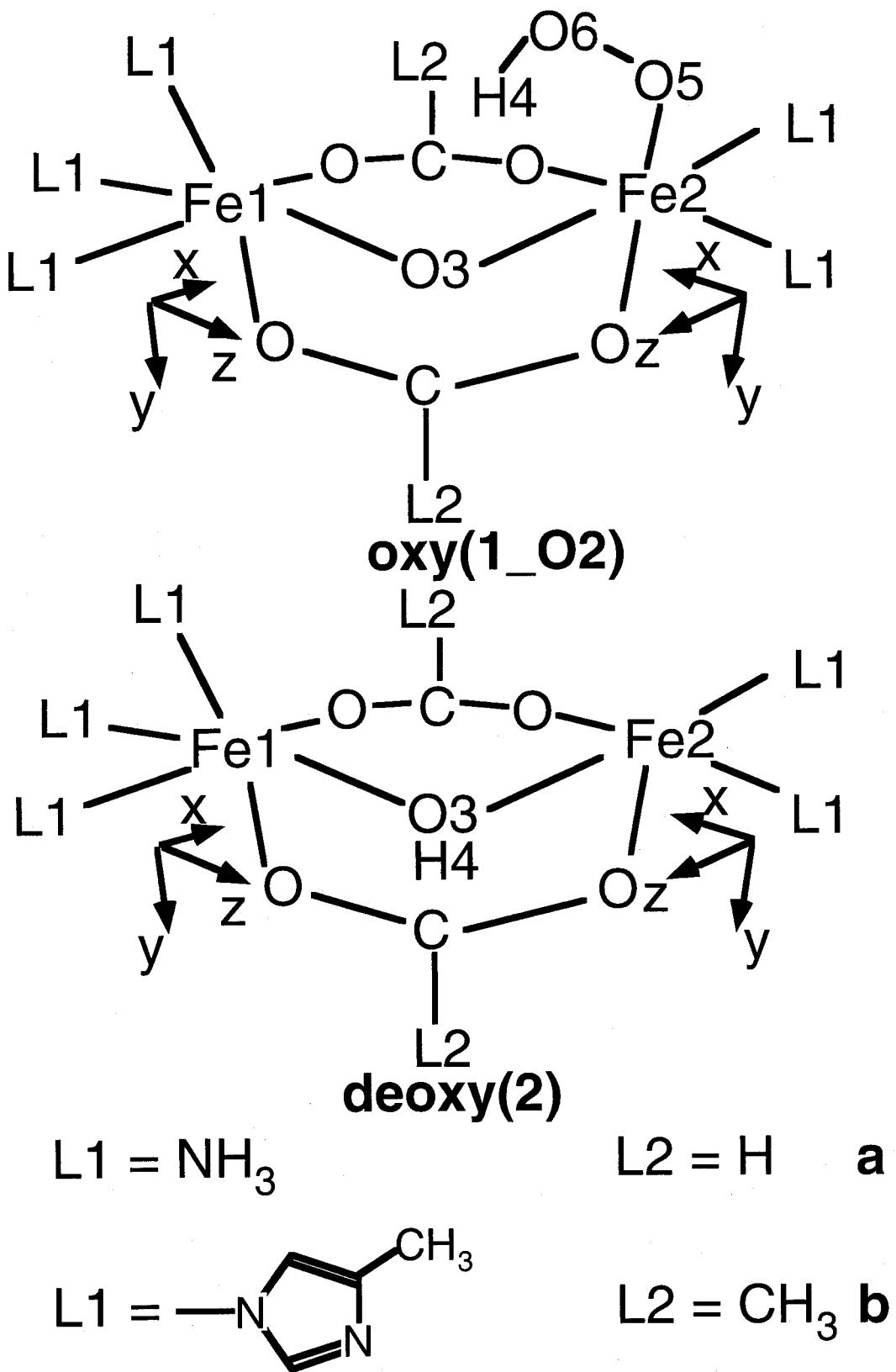
Figure 3.2   Molecular structures of a model of oxyhemerythrin (**1**) with oxygen
(**1_O2**), and a model of deoxyhemerythrin (**2**), respectively. Site
umbers are illustrated in **1_O2** and **2** .
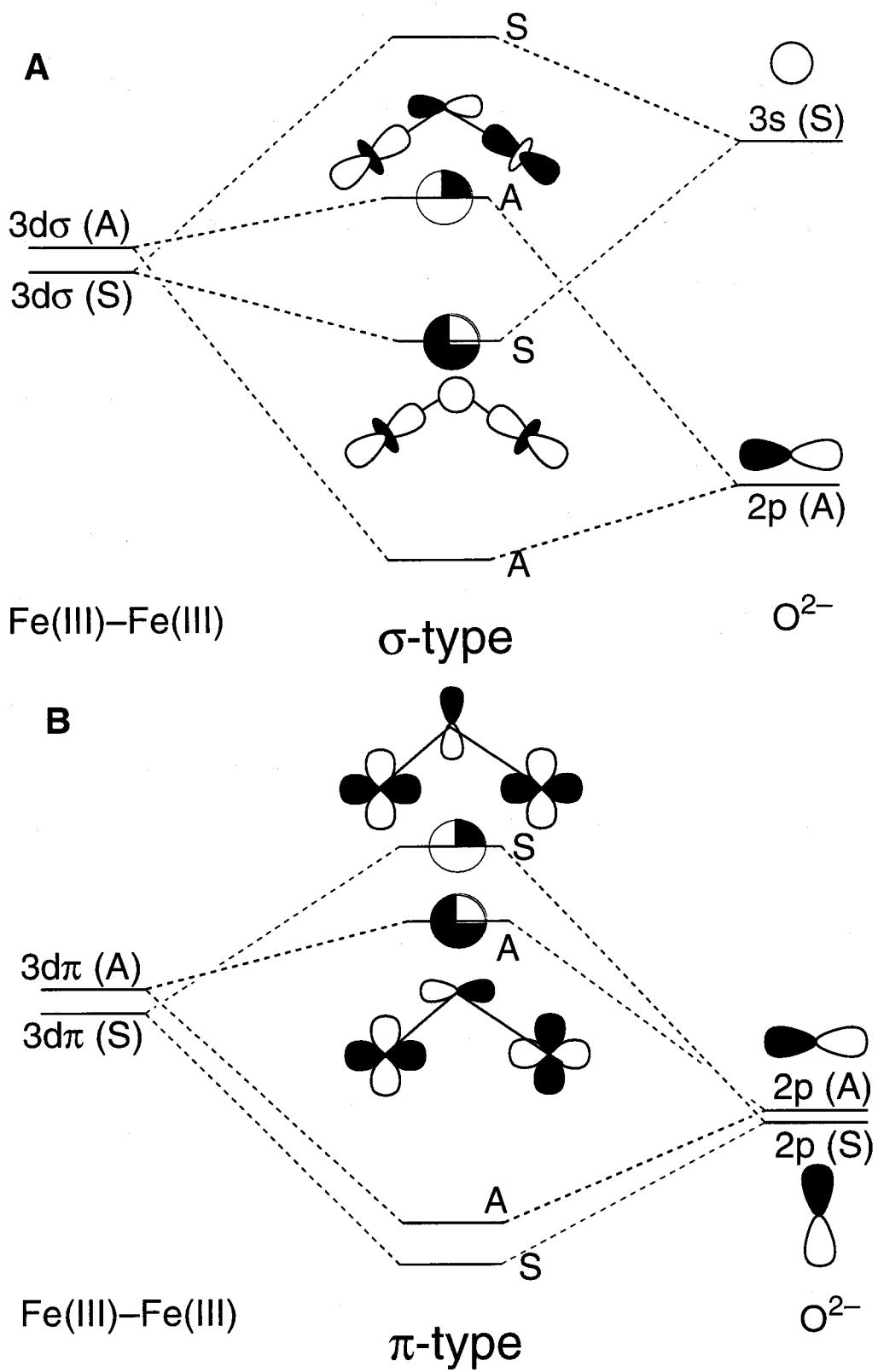
Figure 3.3   Symmetry allowed σ- (**A**) and π- (**B**) type orbital interaction diagrams and schematic illustrations of SOMOs formed by bonding and antibonding MOs of Fe ions and p AOs of bridging ligands.

C

$3d\pi_\perp$ (A)

$3d\pi_\perp$ (S)

$2p$ (S)

Fe(III)–Fe(III)

$\pi_\perp$-type

O^{2-}

D

$3d\delta$ (A)

$3d\delta$ (S)

Fe(III)–Fe(III)

δ-type

acetate

E

$3d\delta_\perp$ (A)

$3d\delta_\perp$ (S)

Fe(III)–Fe(III)
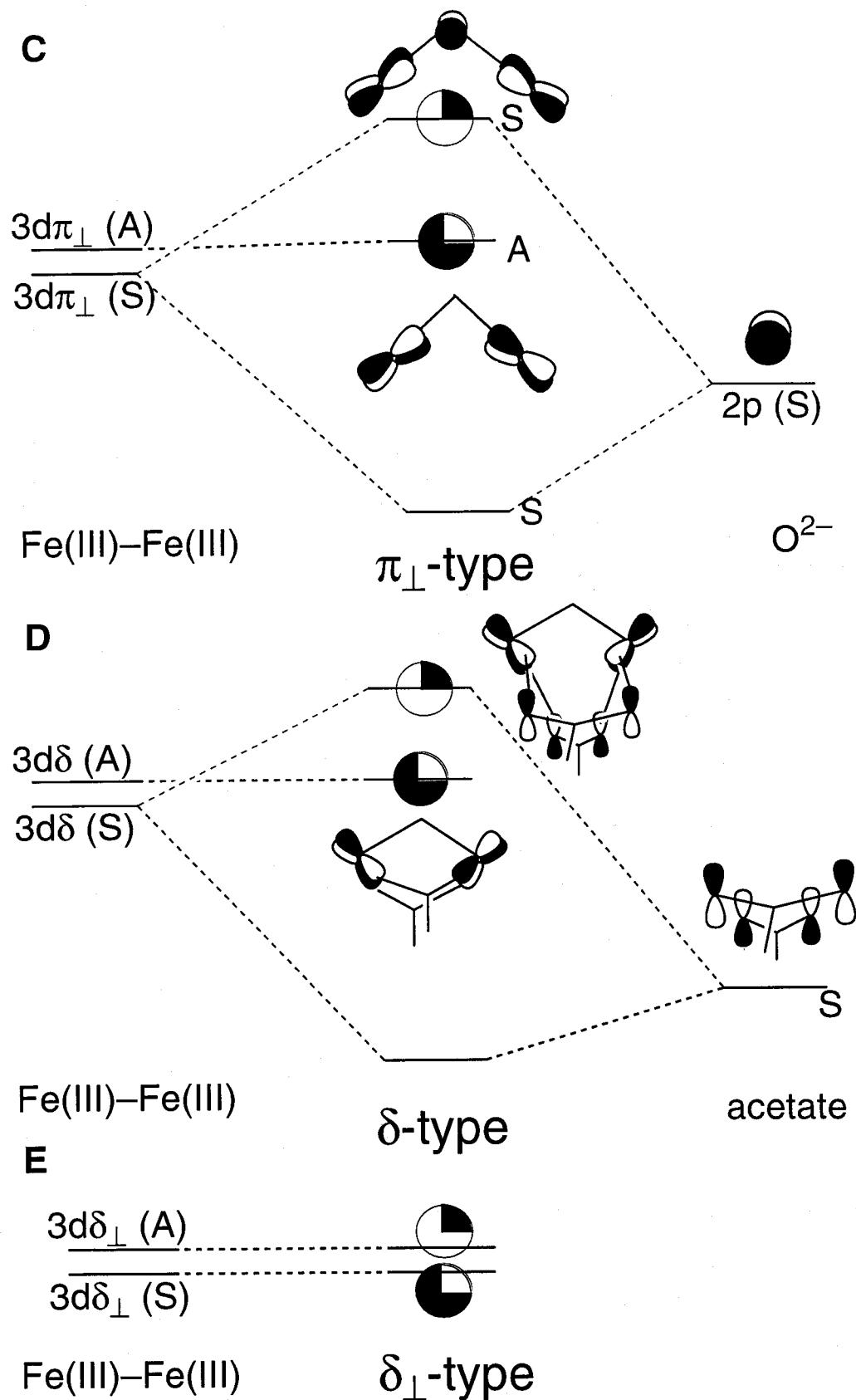
$\delta_\perp$-type

Figure 3.4 Symmetry allowed $\pi_\perp$-(**C**), δ- (**D**) and $\delta_\perp$- (**E**) type orbital interaction diagrams and schematic illustrations of SOMOs formed by bonding and antibonding MOs of Fe ions and p AOs of bridging ligands.

152

σ

SONO–5

σ

SONO+5

π

SONO–4

π

SONO+4

π⊥

SONO–3

π⊥

SONO+3

δ

SONO–2

δ

SONO+2

δ⊥

SONO–1

δ⊥
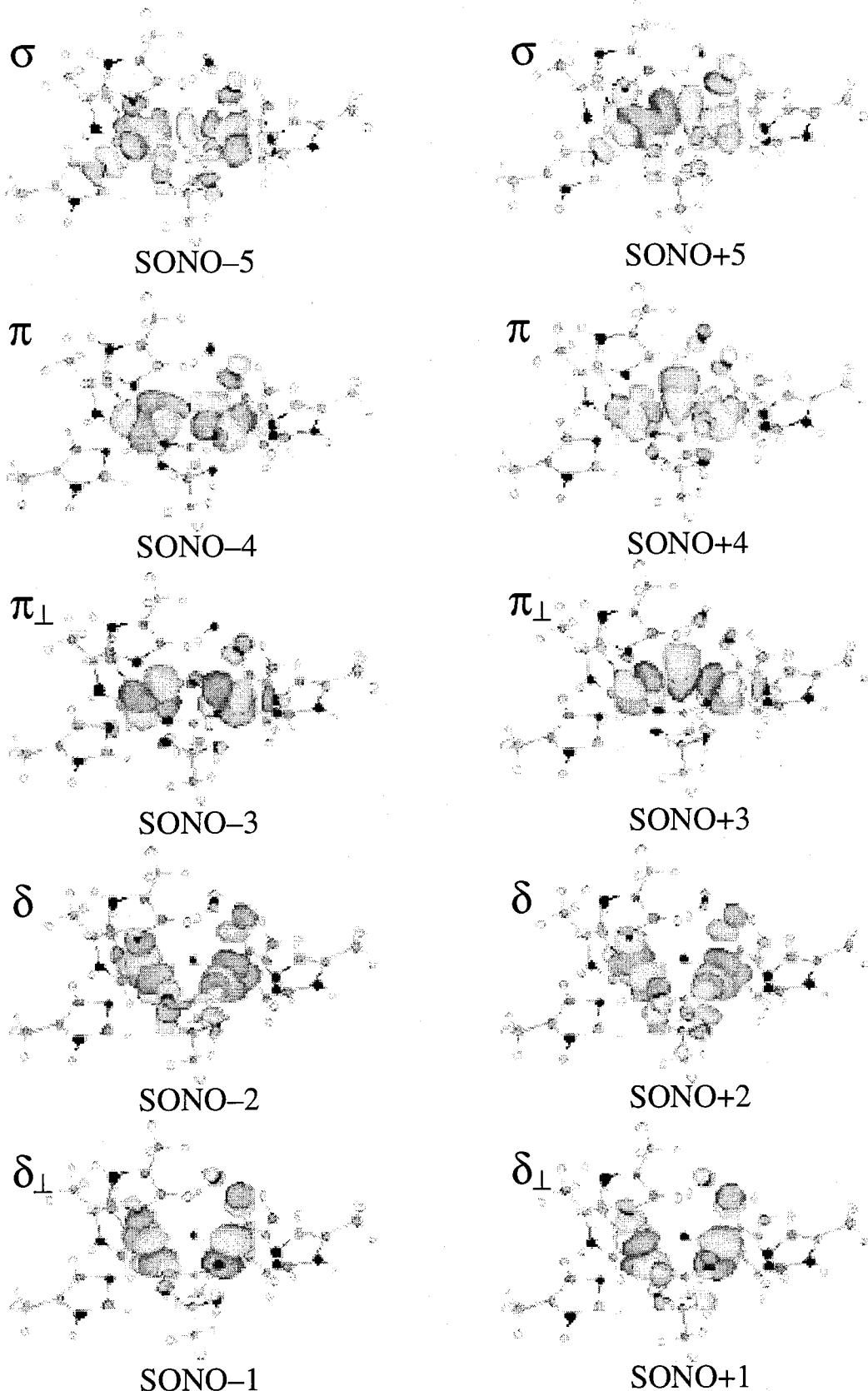
SONO+1

Figure 3.5   Singly occupied bonding (SONO–5 to SONO–1) and antibonding
(SONO+1 to SONO+5) natural orbitals (SONOs) for the LS state of
1b_O2 by UB2LYP.

σ

SONO–4

σ

SONO+4

π

SONO–3

π

SONO+3

$\pi_\perp$

SONO–2

$\pi_\perp$

SONO+2

δ

SONO–1

δ
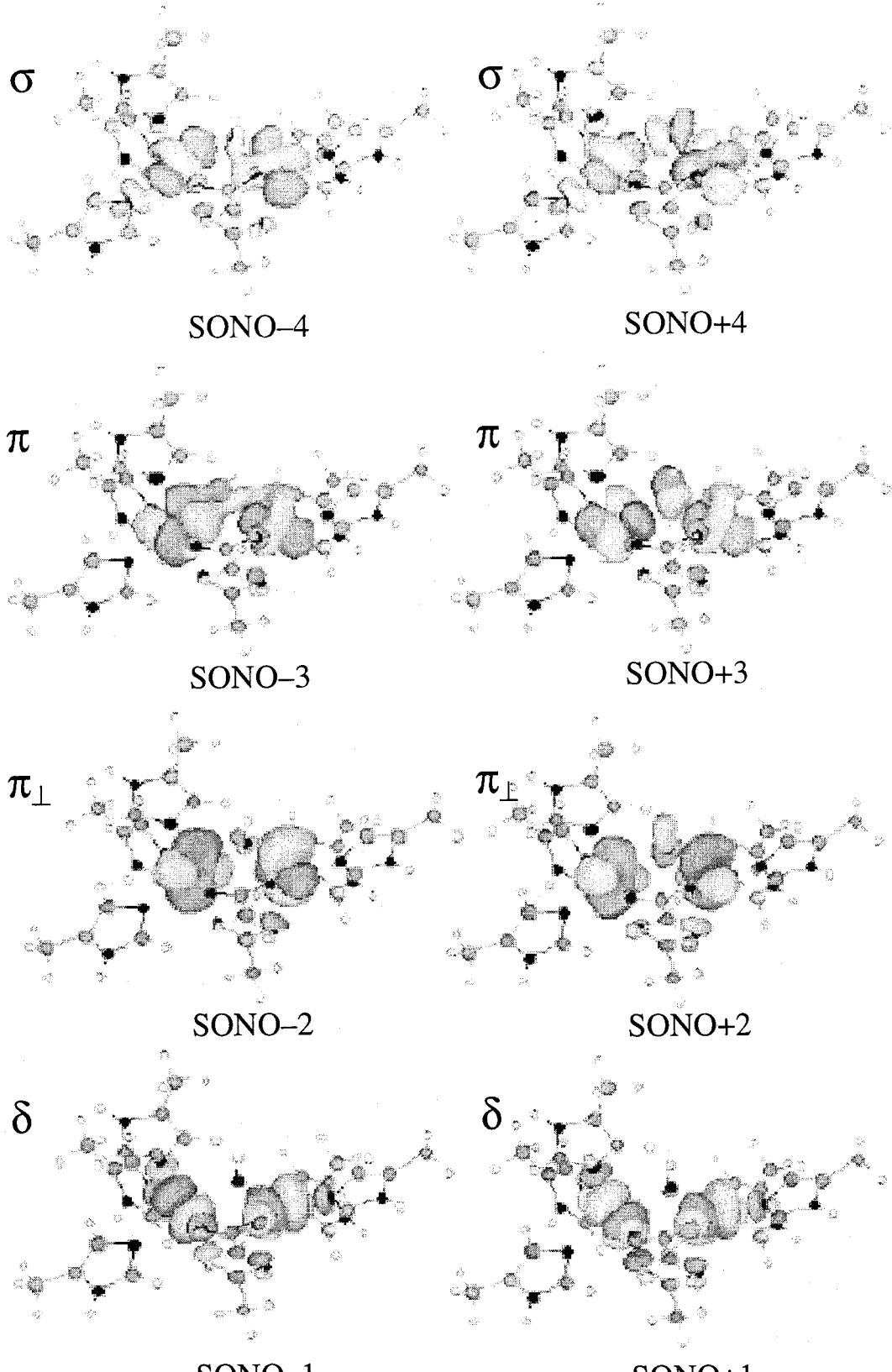
SONO+1

Figure 3.6   Singly occupied bonding (SONO–5 to SONO–1) and antibonding (SONO+1 to SONO+5) natural orbitals (SONOs) for the LS state of **2b_O2** by UB2LYP.
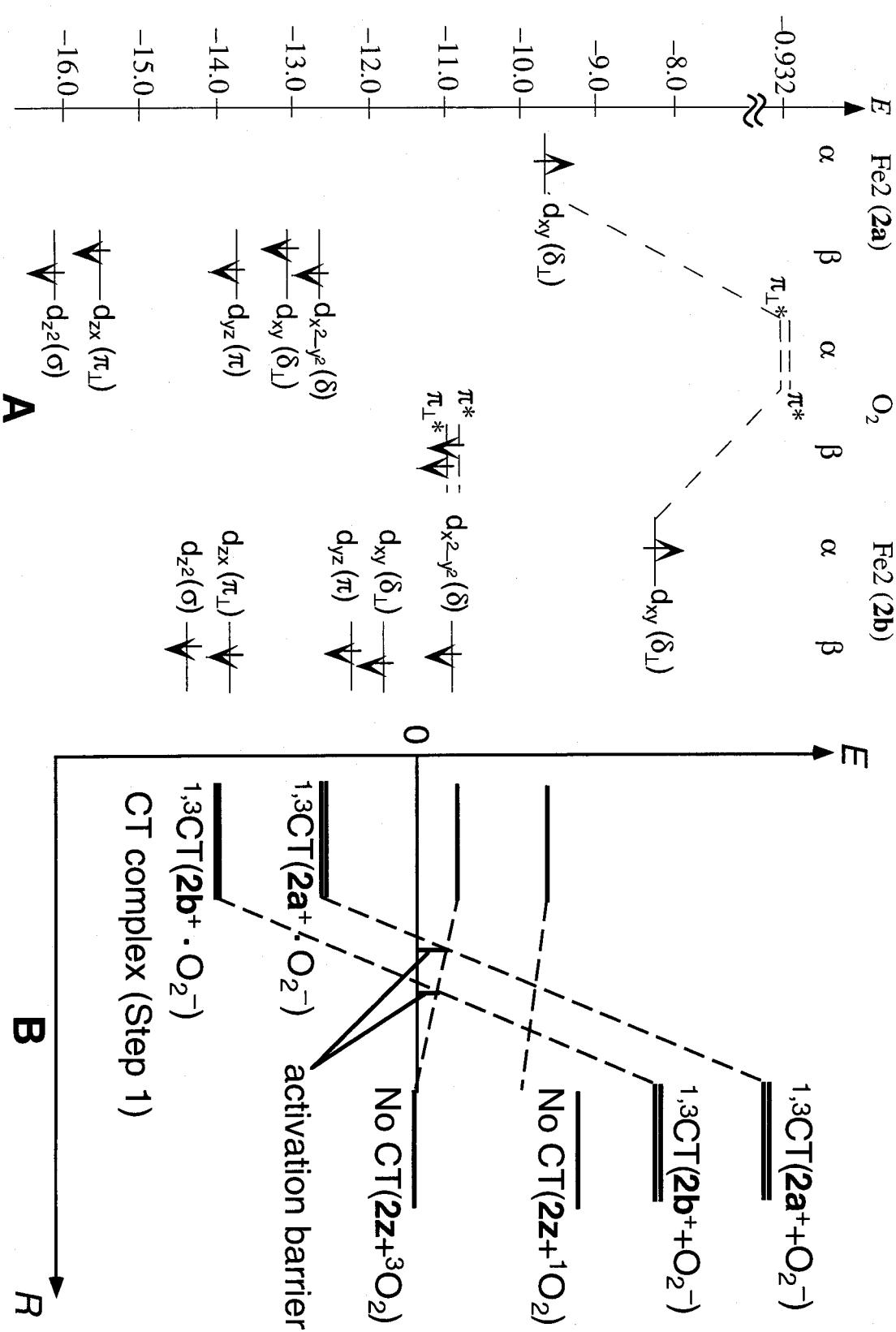
Figure 3.7 Orbital energy diagrams of d orbitals at the Fe2 ion of **1z** (**z** = **a** and **b**) and π* and $\pi_\perp$* orbitals of dioxygen by UB2LYP results (**A**) and configuration energy diagrams by the Mulliken CT theory (**B**).

155
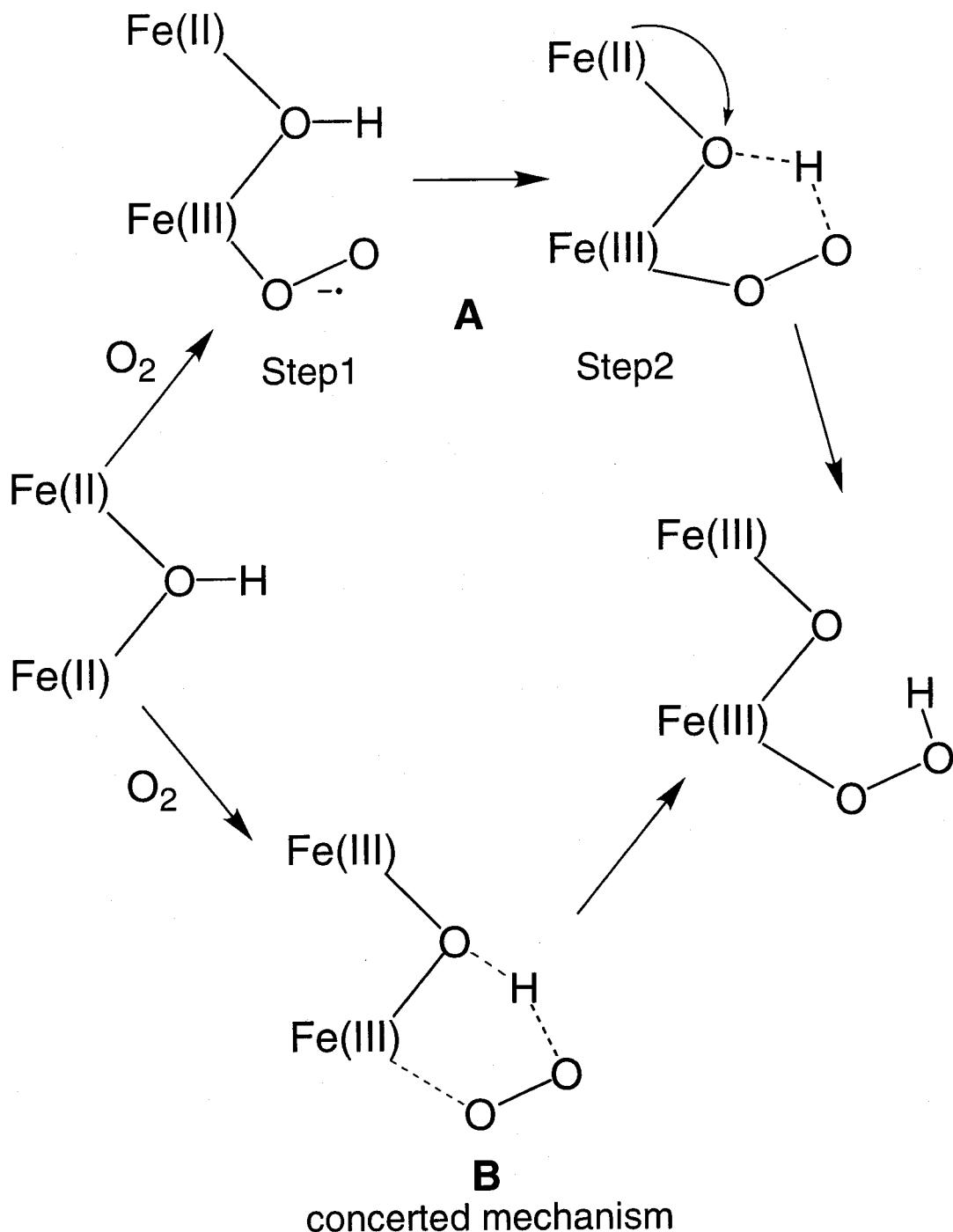
Figure 3.8 Proposed two-step (**A**) and one-step (**B**) mechanisms of dioxygen binding to Hr based on experimental grounds. The hybrid DFT computational results are consistent with the former.

Part III

Chapter 4

Concluding Remarks of Part III

4.1 Reversible Dioxygen Binding Process in Hemocyanin and Hemerythrin

In this part, the author has investigated the ligand coordination effects for the magnetic interaction and the reversible dioxygen binding process, namely how dioxygen is bound to the activation, in hemocyanin (Hc) and hemerythrin (Hr).

In chapter 2, the magnetic interaction for the realistic models of active site in hemocyanin has been investigated by performing hybrid density functional (HDFT) calculations such as UB2LYP. For the purpose, NH_3 (**a**), methylimidazole (**b**) and histidine (**c**) have been utilized as the ligands coordinated to $Cu(II)(\mu-\eta^2:\eta^2O_2^{2-})Cu(II)$ (**1z_O2**) (**z = a-c**) and $Cu(I)-Cu(I)$ (**2z**) cores. Judging from the calculated effective exchange integrals for **1z_O2D**, copper–oxygen bonds are strongly antiferromagnetic, in accord with the experiment. Additionally, in order to elucidate reversible dioxygen binding process and its ligand coordination effects, the author has also performed UB2LYP calculations for **1a_O2**, **1b_O2**, **2a_O2** and **2b_O2** changing two parameters of O–O length, 1.2 Å (**O2N**) for molecular oxygen (O_2) and 1.4 Å (**O2D**) for peroxide (O_2^{2-}). Reversible dioxygen binding of hemocyanin has been investigated in detail from the viewpoint of the shape of potential energy surface, charge and spin density distribution responsible for electron-transfer interaction between **1z** (**2z**) and O_2. With the respect to the dioxygen binding process, the structural change from deoxy to oxyHc is expected to play a crucial role in controlling the stepwise two-electron transfer from dioxygen to Cu–Cu active core of hemocyanin, resulting in association and dissociation of dioxygen. The electron-donating ability of ligands influences the binding energy and the shape of potential energy surfaces of **1z_O2** due to the balance of repulsive interaction between **1z** and dioxygen and symmetry-allowed orbital interactions between bonding and antibonding $d_{xy} \pm d_{xy}$ orbitals of **1z** and π_h^* and π_v^* orbitals of dioxygen. The effective bond-order, localized electron density and information entropy for **1z_O2** were calculated in terms of occupation numbers of the natural orbitals by UB2LYP in order to elucidate the nature of the Cu_2O_2 bonding. These chemical indices indicate that the copper–oxygen bonds in Hc exhibit an intermediate covalent-bonding character (half bonding), which is the origin of an active control of oxygen transport: addition and dissociation of O_2 in Hc by the conformational changes.

In chapter 3, the author has investigated the magnetic interaction and the chemical bond nature of realistic models of the active site in Hr by UHF and DFT calculations. The results have

been discussed in relation to the effective exchange integrals (J_{ab}) and the charge and spin density distributions as well as the shape and symmetry of natural orbitals. In addition, the author has examined the chemical bonding nature of the models of oxy and deoxyHr from the viewpoint of chemical indices such as effective bond order, information entropy and unpaired electron density. The superexchange (SE) interactions via μ-hydroxo bridge accounts for the weak antiferromagnetic interaction between the two ferrous iron ions of deoxyHr. On the other hand, the SE interaction via μ-oxo bridging atom is responsible for the antiferromagnetic coupling between the two ferric iron ions of oxyHr. The author also found that spin-polarized Becke half and half LYP exchange-correlation functionals can be regarded as a reliable method to investigate the magnetic coupling for oxy and deoxyHr. Judging from chemical indices, the difference of the strength of chemical bond is consistent with the fact that the magnetic coupling for the models of oxy Hr is larger than that for deoxy one. They are applicable to elucidate electronic structure of magnetic metal clusters in biological systems, i.e., biomolecular magnetism. At last, the author has discussed the dioxygen trapping in deoxyHr on the basis of Mulliken CT theory, proposing a two-step electron transfer mechanism

4.2 Future Prospects

In this thesis, the author has focused attention on the static electronic structure of the active site in metalloproteins. The molecular orbital (MO) calculations such as HF, hybrid DFT and DFT have provided a lot of insights into the biological process of the methalloproteins. However, in order to deeply understand biological function of metalloproteins, it is necessary to perform theoretical calculations including proteins which surround the active sites and to employ the molecular simulation involving time and temperature. In other words, the dynamical molecular simulation for whole metalloprotein would elucidate the biological function in detail.   Therefore, molecular dynamics (MD) and molecular mechanics (MC) containing MO calculations, ab initio MD calculations, should be performed for the metalloprotein.   Nowadays, ab initio MD methods are developed and applied for a lot of proteins and enzymes in order to understand the protein functions. However, since metalloproteins are huge and strong electron correlated systems, ab

initio MD calculations have not performed for such systems.   Judging from the existence of a lot of proteins which requite metal ions to perform complicated biological function, theoretical investigations for the metalloproteins, theoretical bioinorganic chemistry, are very exciting interdisciplinary field among physics, chemistry and biology.

References of Part III

(1) Tolman, W. B. *Acc. Chem. Res.* **1997**, *30*, 227.

(2) Niederhoffer, E. C.; Timmons, J. H.; Martell, A. E. *Chem. Rev.* **1984**, *89*, 137.

(3) Stenkamp, R. E. *Chem. Rev.* **1994**, *94*, 715.

(4) Solomon, E. I.; Baldwin, M. J.; Lowery, M. D. *Chem. Rev.* **1992**, *92*, 521.

(5) Holm, R. H.; Kennephol, P.; Solomon, E. I. *Chem. Rev.* **1996**, *96*, 2239

(6) Solomon, E. I.; Lowery, M. D. *Science* **1993**, *259*, 1575.

(7) Blomberg, M. R. A.; Siegbahn, P. E. M. *J. Phys. Chem. B* **2001**, *105*, 9375.

(8) Siegbahn, P. E. M.; Blomberg, M. R. A. *Chem. Rev.* **2000**, *100*, 421.

(9) Magnus, K. A.; Hazes, B.; Ton-That, H.; Bonaventura, C.; Bonaventura, J.; Hol, W. G. J. *Proteins* **1994**, *19*, 302.

(10) Hazes, B.; Magnus, K. A.; Bonaventura, C.; Bonaventura, J.; Dauter, Z.; Kalk, K. H.; Hol, W. G. J. *Protein Sci.* **1993**, *2*, 597.

(11) Larrabee, J. A; Spiro, T. G. *J. Am. Chem. Soc.* **1980**, *102*, 4217.

(12) Eickman, N. C.; Himmelwright, R. S.; Solomon, E. I. *Proc. Natl. Acad. Sci. U.S.A.* **1979**, *76*, 2094.

(13) Woolery, G. L.; Powers, L.; Winkler, M.; Solomon, E. I.; Spiro, T. G. *J. Am. Chem. Soc.* **1984**, *106*, 86.

(14) Brown, J. M.; Powers, L.; Winkler, M.; Solomon, E. I.; Spiro, T. G. *J. Am. Chem. Soc.* **1980**, *102*, 4210.

(15) Co, M. S.; Hodgson, K. O.; *J. Am. Chem. Soc.* **1981**, *103*, 3200.

(16) Dooley, D. M.; Scott, R. A.; Ellinghaus, J.; Solomon, E. I.; Gray, H. B. *Proc. Natl. Acad. Sci. U.S. A.* **1978**, *75*, 3019.

(17) Solomon, E. I.; Dooley, D. M.; Wang, R. H.; Gra, H. B.; Cerdonio, M.; Mogno, F.; Romani, G. L. *J. Am. Chem. Soc.* **1976**, *98*, 1029.

(18) Kitajima, N.; Fujisawa, K.; Fujimoto, C.; Moro-oka, Y.; Hashimoto, S.; Kitagawa, T.; Toriumi, K.; Tatsumi, K.; Nakamura, A. *J. Am. Chem. Soc.* **1992**, *114*, 1277.

(19) Kitajima, N.; Fujisawa, K.; Moro-oka, Y.; Toriumi, K. *J. Am. Chem. Soc.* **1989**, *111*, 8975.

(20) Karlin, K. D.; Kaderli, S.; Zuberbühler, A. D. *Acc. Chem. Res.* **1997**, *30*, 139.

(21) Kodera, M.; Katayama, K.; Tachi, Y.; Kano, K.; Hirota, S.; Fujinami, S.; Suzuki, M. *J. Am. Chem. Soc.* **1999**, *121*, 11006.

(22) Gebbink, R. J. M. K.; Martens, C. F.; Kenis, P. J. A.; Jansen, R. J.; Nolting, H-F.; Solé, V. A.; Feiters, M. C.; Karlin, K. D.; Nolte, R. J. M. *Inorg. Chem.* **1999**, *38*, 5755.

(23) Baldwin, M. J.; Root, D. E.; Pate, J. E.; Fujisawa, K.; Kitajima, N.; Solomon, E. I. *J. Am. Chem. Soc.* **1992**, *114*, 10421.

(24) Baldwin, M. J.; Ross, P. K.; Pate, J. E.; Tyeklár, Z.; Karlin, K. D.; Solomon, E. I. *J. Am. Chem. Soc.* **1991**, *113*, 8671.

(25) Liang, H-C.; Karlin, K. D.; Dyson, R.; Kaderli, S.; Jung, B.; Zuberbühler, A. D. *Inorg. Chem.* **2000**, *39*, 5884–5894.

(26) Tuczek, F.; Solomon, E. I.; *J. Am. Chem. Soc.* **1994**, *116*, 6916.

(27) Ross, P. K.; Solomon, E. I. *J. Am. Chem. Soc.* **1990**, *112*, 5871.

(28) Ross, P. K.; Solomon, E. I. *J. Am. Chem. Soc.* **1991**, *113*, 3246.

(29) Maddaluno, J.; Giessner-Prettre, C. *Inorg. Chem.* **1991**, *30*, 3439.

(30) Getlicherman, H.; Giessner-Prettre, C.; Maddaluno, J. *J. Phys. Chem.* **1996**, *100*, 6819.

(31) Eisenstein, O.; Giessner-Prettre, C.; Maddaluno, J.; Stussi, D.; Weber, J. *Arch. Biochem. Biophys.* **1992**, *296*, 247.

(32) Bernardi, F.; Bottoni, A.; Casadio, R.; Fariselli, P.; Rigo, A. *Inorg. Chem.* **1996**, *35*, 5207.

(33) Bernardi, F.; Bottoni, A.; Casadio, R.; Fariselli, P.; Rigo, A. *Int. J. Quant. Chem.* **1996**, *58*, 109.

(34) Erasmus, C.; Haase, W. *Inorg. Chim. Acta* **1994**, *221*, 141.

(35) Flock, M.; Pierloot, K. *J. Phys. Chem. A* **1999**, *103*, 95.

(36) Bérces, A. *Inorg. Chem.* **1997**, *36*, 4831.

(37) Estiu, G. L.; Zerner, M. C. *J. Chem. Am. Soc.* **1999**, *121*, 1893.

(38) Here, we have examined the least-motion dissociation (or association) paths only to elucidate differences of ligand coordination effects. During our study, detailed dioxygen binding path of the hemocyanin has been investigated and reported employing ammonia ligands as the histidine. Metz, M.; Solomon, E. I.; *J. Am. Chem. Soc.* **2001**, *123*, 4938.

(39) Tatewaki, H.; Huzinaga, S. *J. Chem. Phys.* **1980**, *72*, 339.

(40) Hay, P. J. *J. Chem. Phys.* **1977**, *66*, 4377.

(41) Hariharan, P. C.; Pople, J. A. *Theoret. Chim. Acta* **1973**, 28, 213.

(42) Hehre, W. J.; Ditchfild, R.; Pople, J. A. *J. Chem. Phys.,* **1972**, *56*, 2257.

(43) Kearns, D. R. *Chem. Rev.* **1971**, *71*, 395.

(44) *Singlet Oxygen*; Wasserman, H. H.; Murray, R. W., Eds.; Academic Press: New York, 1979.

(45) Takano, Y.; Tsunesada, T.; Isobe, H.; Yoshioka, Y.; Yamaguchi, K.; Saito, I. *Bull. Chem. Soc. Jpn.* **1999**, *72*, 213.

(46) Siegbahn P. E. M.; Blomberg, M. R. A. *Annu. Rev. Phys. Chem.* **1999**, *50*, 221.

(47) Yoshioka, Y.; Kubo, S.; Yamaguchi K.; Saito, I. *Chem. Phys. Lett.* **1998**, *294*, 459.

(48) Holmes, M. A.; Le Trong, I.; Turley, S.; Sieker, L. C.; Stenkamp, R. E. *J. Mol. Biol.* **1991**, *218*, 583.

(49) Dawson, J. W.; Gray, H. B.; Hoenig, H. E.; Rossman, G. R.; Schredder, J. M.; Wang, R. H. *Biochemistry* **1972**, *11*, 461.

(50) Reem, R. C.; Solomon, E. I. *J. Am. Chem. Soc.* **1989**, *111*, 4688.

(51) Brunold, T. C.; Solomon, E. I. *J. Am. Chem. Soc.* **1999**, *121*, 8277.

(52) Armstrong, W. H.; Lippard, S. J. *J. Am. Chem. Soc.* **1983**, *105*, 4837.

(53) Armstrong W. H.; Spool, A.; Papaefhymiou, G. C.; Frankel, R. B.; Lippard, S. J. *J. Am. Chem. Soc.* **1984**, *106*, 3633.

(54) Chaudhuri, P.; Wieghardt, K.; Nuber, B.; Weiss, J. *Angew. Chem. Int. Ed. Engl.* **1985**, *24*, 778.

(55) Hartman, J. R.; Rardin, R. L.; Chaudhuri, P.; Pohl, K.; Wieghardt, K.; Nuber, B.; Weiss, J.; Papaefthymiou, G. C.; Frankel, R. B.; Lippard, S. J. *J. Am. Chem. Soc.* **1987**, *109*, 7387.

(56) Que, L., Jr.; True, A. E.; *Progress in Inorganic Chemistry: Bioinorganic Chemistray*; Lippard, S. J., Ed.; John Wiley & Sons, Inc.; New York, Vol. 38 1990; p 97.

(57) Howard, J. B.; Rees, D. C. *Adv. Protein Chem.* **1991**, *42*, 199.

Part IV

General Conclusion

Part IV

Chapter 1

General Conclusion of This Thesis

In this doctoral thesis, the author has performed theoretical investigation for d-p conjugated systems found in the field of molecule-based magnetism and biology. There are four conclusions of this thesis as follows.

(I) Propose of the spin-alignment rules for d-π-p and d-π-d conjugated magnetic systems

The author has investigated the magnetic interaction for the d-π-p and d-π-d conjugated magnetic systems. The subtle balance of spin polarization and spin delocalization (superexchange) effects determines the spin-alignment of d-π-p and d-π-d conjugated magnetic systems in contrast to that of p-π-p conjugated systems which is mainly controlled by spin polarization effects.

(II) Theoretical description of the mechanism of the dioxygen binding process in non-heme oxygen transport proteins

The author has investigated the reversible dioxygen binding process and to make it clear how dioxygen is bound to the active sites in hemocyanin and hemerythrin. Analyses on the basis of the orbital symmetry and Mulliken CT theory lead to the stepwise dioxygen binding process in these non-heme oxygen transport proteins.

(III) Theoretical examination of the ligand coordination effects for the d-p conjugated systems

The ligands ligated to the active core or d-spin site attribute to these interesting characteristics of d-p conjugated systems. Theoretical calculation has shown that the electronic structure of naked active core systems is totally different from that of ligand coordinated systems. The coordination ligands regulate the orbital interaction and charge transfer of the active core, and provide electronic and magnetic structure for these systems leading to interesting functions such as photo-induced magnetism and oxygen transport.

(IV) Confirmation of the effectiveness to hybrid DFT computation for the d-p conjugated systems

Density functional theory (DFT) developed in solid state physics has been accepted as an alternative approach to overcome the electron correlation problem. Nowadays, DFT calculations are widely used in computational chemistry because of their simple procedures in practical applications to large molecules and polymers, and has been accepted as an alternative approach for the post HF methods. However, pure DFT tends to overestimate the electron delocalization and to overstabilize the electronic energy in LS state for the d-p conjugated systems which include the

strong electron correlation.   In this thesis, the author has applied the HF plus DFT hybrid methods

(hybrid DFT) for the d-p conjugated systems and succeeded to reproduce the magnetic interaction

quantitatively.

List of Publications

[A] Main Papers

(1) "Theoretical Studies of Decomposition Reactions of Dioxetane, Dioxetanone, and Related Species. CT Induced Luminescence Mechanism Revisited."
Yu Takano, Tsunaki Tsunesada, Hiroshi Isobe, Yasunori Yoshioka, Kizashi Yamaguchi, Isao Saito,
Bull. Chem. Soc. Jpn., **72**, 213–225 (1999).

(2) "Theoretical studies of the effective exchange interactions and photoinduced magneism in manganese and copper Di(4-pyridyl)Carbene Complexes."
Yu Takano, Tomohisa Soda, Yasutaka Kitagawa, Yasunori Yoshioka, Kizashi Yamaguchi,
Chem. Phys. Lett., **301**, 309–316 (1999).

(3) "Theoretical Studies on Magnetic Interaction of Mn-π Conjugated Systems."
Yu Takano, Tomohisa Soda, Yasutaka Kitagawa, Taku Onishi, Yasunori Yoshioka, Kizashi Yamaguchi,
Mol. Cryst. Liq. Cryst., **342**, 291–296 (2000).

(4) "Density functional and post Hartree-Fock studies on the effective exchange interaction of d-π-p and d-π-d conjugated systems involving m-phenylene bridge."
Yu Takano, Taku Onishi, Yasutaka Kitagawa, Tomohisa Soda, Yasunori Yoshioka, Kizashi Yamaguchi,
Int. J. Quant. Chem., **80**, 681–691 (2000).

(5) "Theoretical studies on the magnetic and reversible dioxygen binding of the active site in hemocyanin."
Yu Takano, Shigehiro Kubo, Taku Onishi, Hiroshi Isobe, Yasunori Yoshioka, Kizashi Yamaguchi,
Chem. Phys. Lett., **335**, 395–403 (2001).

(6) "Extended Hartree-Fock (EHF) theory of chemical reactions VI. Hybrid DFT and post-Hartree-Fock approaches for concerted and nonconcerted transition structures of the Diels-Alder reaction."
Hiroshi Isobe, Yu Takano, Yasutaka Kitagawa, Takashi Kawakami, Shusuke Yamanaka,

Kizashi Yamaguchi, Kendall N. Houk,

Mol. Phys., in press.

(7) "Density functional study on the photo-induced magnetism in Cu(II) and Mn(II) bis(hexafluoroacetylacetonato) with di(4-pyridylcarbene):UBLYP, UB3LYP, UB2LYP and UHF calculations."

Yu Takano, Yasutaka Kitagawa, Taku Onishi, Yasunori Yoshioka, Kizashi Yamaguchi, Noboru Koga, Hiizu Iwamura,

J. Am. Soc. Chem., **124**, 450–461 (2002).

(8) "Theoretical Studies on Magnetic Interaction of M-π Conjugated Systems via Pyrimidine Coupler."

Yu Takano, Hiroshi Isobe, Takashi Kawakami, Kizashi Yamaguchi,

Mol. Cryst. Liq. Cryst., in press.

(9) "The nature of the copper–oxygen bonds in hemocyanin by hybrid DFT calculation of effective exchange integrals and dioxygen binding energy via ligand coordination effects."

Yu Takano, Shigehiro Kubo, Hiroshi Isobe and Kizashi Yamaguchi,

J. Am. Chem. Soc., submitted.

(10) "Theoretical studies on magnetic and electronic structures of the active site in oxygenated and deoxygenated hemerythrin: A hybrid DFT approach for biomolecular magnetism."

Yu Takano, Hiroshi Isobe, Kizashi Yamaguchi,

J. Am. Chem. Soc., submitted.

(11) "Hybrid DFT studies on the magnetic interaction and weak covalent-bonding for phenalenyl radical dimeric pair."

Yu Takano, Takeshi Taniguchi, Takashi Kubo, Kagetoshi Yamamoto, Takeji Takui, Kazuhiro Nakasuji and Kizashi Yamaguchi

J. Am. Chem. Soc., submitted.

(12) "Effective exchange integrals, effective bond order, unpaired electron density and information entropy for a phenalenyl radical dimeric pair."

Yu Takano, Takeshi Taniguchi, Takashi Kubo, Kagetoshi Yamamoto, Takeji Takui, Kazuhiro Nakasuji and Kizashi Yamaguchi

Chem. Phys. Lett., submitted.

[B] Others

(1) "Hubbard and Heisenberg Models for Four-Site Four-Electron Systems.Group-Theoretical Interrelationships and Applications to Multinuclear Transition-Metal Clusters."
Yasunori Yoshioka, Shigehiro Kubo, Shinji Kiribayashi, Yu Takano, Kizashi Yamaguchi,
Bull. Chem. Soc. Jpn., **71**, 573–588 (1998).

(2) "Ab Initio Size-Consistent Calculations of Effective Exchange Interactions in Mesoscopic Magnetic Clusters Composed of Triplet Methylenes and Quartet Nitrogen Atoms."
Takashi Kawakami, Syusuke Yamanaka, Yu Takano, Yasunori Yoshioka, Kizashi Yamaguchi,
Bull. Chem. Soc. Jpn., **71**, 2097–2108 (1998).

(3) "Theoretical Study of Electronic Structures of One-Dimensional Magnetic Clusters Composed of Doublet Lithium and Copper Atoms."
Takashi Kawakami, Syusuke Yamanaka, Yu Takano, Yasunori Yoshioka, Kizashi Yamaguchi,
J. Mol. Struct. (Theochem), **451**, 89–107 (1998).

(4) "Electronic structures of organometallic conjugated systems. Possibilities of molecular magnets, magnetic conductors and spin-mediated superconductors composed of metallocene units."
Taka-aki Okamura, Yu Takano, Yasunori Yoshioka, Norikazu Ueyama, Akira Nakamura, Kizashi Yamaguchi
J. Organomet. Chem., **569**, 177–187 (1998).

(5) "Symmetry and Broken Symmetries in MO Descriptions of Unstable Molecules II. Alignment, Flustration and Tunneling of Spins in Mesoscopic Molecular Magnets."
Kizashi Yamaguchi, Syusuke Yamanaka, Masamichi Nishino, Yu Takano, Yasutaka Kitagawa, Hidemi Nagao, Yasunori Yoshioka,
Theor. Chem. Acc., **102**, 328–345 (1999).

(6) "Density functional study of intramolecular ferromagnetic interaction through m-phenylene coupling unit (III): Possibility of high-spin polymer."
Masaki Mitani, Yu Takano, Yasunori Yoshioka, Kizashi Yamaguchi,
J. Chem. Phys., **111**, 2283–2294 (1999).

(7) "Experimental and theoretical studies on the selectivity of GGG triplets toward one-electron

oxidation in B-form DNA."

Yasunori Yoshioka, Yasutaka Kitagawa, Yu Takano, Kizashi Yamaguchi, Takashi Nakamura, Isao Saito,

J. Am. Chem. Soc., **121**, 8712–8719 (1999).

(8) "Ab Initio Crystal Orbital Study of Ferromagneic Interaction of Spins in Polymer Comprising Phenylenevinylene."

Masaki Mitani, Yu Takano, Daisuke Yamaki, Yasunori Yoshioka, Kizashi Yamaguchi,

Mol. Cryst. and Liq. Cryst., **335**, 613–622 (1999).

(9) "Thoretical studies on magnetic interactions of dichroium tetraacetate by using hybrid density functional theory."

Yasutaka Kitagawa, Tomohisa Soda, Taku Onishi, Yu Takano, Yasunori Yoshioka, Kizashi Yamaguchi,

Mol. Cryst. Liq. Cryst., **343**, 145–150 (2000).

(10) "Theoretical Studies on Magnetic Interaction of Di-μ-Oxo Bridged Manganese Dimers."

Tomohisa Soda, Yasutaka Kitagawa, Taku Onishi, Yu Takano, Yasunori Yoshioka, Kizashi Yamaguchi,

Mol. Cryst. Liq. Cryst., **343**, 157–162 (2000).

(11) "Theoretical Studies of the Antiferromagnetic Model Clusters for K_2MX_4 Type Solids."

Taku Onishi, Tomohisa Soda, Yasutaka Kitagawa, Yu Takano, Daisuke Yamaki, Satoshi Takamizawa, Yasunori Yoshioka, Kizashi Yamaguchi,

Mol. Cryst. Liq. Cryst., **343**, 133–138 (2000).

(12) "Theoretical Study on Necessary Conditions for Reversible Photoinduced Magnetization: Cobalt-Iron Cyanide System."

Masamichi Nishino, Yasutaka Kitagawa, Taku Onishi, Tomohisa Soda, Yu Takano, Hidemi Nagao, Yasunori Yoshioka, Kizashi Yamaguchi,

Mol. Cryst. Liq. Cryst., **343**, 151–156 (2000).

(13) "Ab initio computation of effective exchange integrals for H–H, H–He–H and Mn_2O_2 complex. Comparison of broken-symmetry approaches."

Tomohisa Soda, Yasutaka Kitagawa, Taku Onishi, Yu Takano, Yasuteru Shigeta, Hidemi Nagao, Yasunori Yoshioka, Kizashi Yamaguchi,

Chem. Phys. Lett., **319**, 223–230 (2000).

(14) "Density functional study of intramolecular ferromagnetic interaction through m-phenylene coupling unit (I): UBLYP, UB3LYP and UHF calculation."
Masaki Mitani, Hiroki Mori, Yu Takano, Daisuke Yamaki, Yasunori Yoshioka, Kizashi Yamaguchi,
J. Chem. Phys., **113**, 4035–4051 (2000).

(15) "Density functional study of intramolecular ferromagnetic interaction through m-phenylene coupling unit (II): Examination of functional dependency."
Masaki Mitani, Daisuke Yamaki, Yu Takano, Yasutaka Kitagawa, Yasunori Yoshioka, Kizashi Yamaguchi,
J. Chem. Phys., **113**, 10486–10504 (2000).

(16) "Theoretical Study of the Magnetic Interaction for M-O-M type Metal Oxides. Comparison of Broken-Symmetry Approaches."
Taku Onishi, Yu Takano, Yasutaka Kitagawa, Takashi Kawakami, Yasunori Yoshioka, Kizashi Yamaguchi,
Polyhedron, **20**, 1177–1184 (2001).

(17) "EHF Theory of Chemical Reactions V. The Nature of Manganese-Oxygen Bonds in Photosystem II by Hybrid Density Functional (DFT) and Coupled-Cluster (CC) Methods."
Hiroshi Isobe, Tomohisa Soda, Yasutaka Kitagawa, Yu Takano, Takashi Kawakami, Yasunori Yoshioka and Kizashi Yamaguchi,
Int. J. Quant. Chem., **85**, 34–43 (2001).

(18) "Theoretical Study on the Magnetic Interaction for Manganese Oxides."
Taku Onishi, Yu Takano, Yasutaka Kitagawa, Takashi Kawakami, Yasunori Yoshioka, Kizashi Yamaguchi,
Mol. Cryst. Liq. Cryst., in press.

(19) "Theoretical investigation of magnetic parameters in two dimentional sheets of pure organic BEDT-TTF and BETS molecules by using ab initio MO and DFT methods."
T. Kawakami, T. Taniguchi, Y. Kitagawa, Y. Takano, H. Nagao and K. Yamaguchi,
Mol. Phys., submitted.

(20) "Generalized spin density functional study of multicenter polyradical systems."

   S. Yamanaka, Y. Takano and K. Yamaguchi,

   Mol. Phys., submitted.

(21) "Analytical and Ab initio Studies of Effective Exchange Interactions, Polyradical Charcter,

   Unpaited Electron Density and Information Entropy in Radical Clusters $(R)_N$: Allyl Radical

   Cluster (N = 2–10) and Hydrogen Radical Cluster."

   Kizashi Yamaguchi, Takashi Kawakami, Yu Takano, Yasutaka Kitagawa, Yoshifumi

   Yamashita and Harunori Fujita,

   Int. J. Quant. Chem., submitted

(22) "Theoretical Studies on Contributions of SOMO–SOMO and Other Couplings to the Magnetic

   Interaction in Radical Clusters."

   Ryo Takeda, Yu Takano, Yasutaka Kitagawa, Takashi Kawakami, Yoshifumi Yamashita,

   Fumitake Matsuoka, Kizashi Yamaguchi,

   Mol. Cryst. Liq. Cryst., submitted.

(23) "Theoretical Studies of Electoron-Phonon and Multi-Band Effects of MgB_2."

   Kizashi Yamaguchi, Yasutaka Kitagawa, Masahiro Takahata, Taku Onishi, Hiroshi Isobe, Yu

   Takano, Takashi Kawakami, Hidemi Nagao,

   Mol. Cryst. Liq. Cryst., submitted.

(24) "Theoretical Studies on Electronic States of Hole-doped Copper Oxides."

   Taku Onishi, Yu Takano, Daisuke Yamaki, Kizashi Yamaguchi,

   Mol. Cryst. Liq. Cryst., submitted.